

Assessment of the Radiological Risks for a Beta-Beam Facility at CERN

THÈSE N° 5757 (2013)

PRÉSENTÉE LE 30 MAI 2013
À LA FACULTÉ DES SCIENCES DE BASE
LABORATOIRE DE PHYSIQUE DES ACCÉLÉRATEURS DE PARTICULES
PROGRAMME DOCTORAL EN PHYSIQUE

ÉCOLE POLYTECHNIQUE FÉDÉRALE DE LAUSANNE

POUR L'OBTENTION DU GRADE DE DOCTEUR ÈS SCIENCES

PAR

Stefania TROVATI

acceptée sur proposition du jury:

Prof. R. Schaller, président du jury
Prof. L. Rivkin, directeur de thèse
Prof. A. Bay, rapporteur
Dr M. Benedikt, rapporteur
Dr M. Magistris, rapporteur



ÉCOLE POLYTECHNIQUE
FÉDÉRALE DE LAUSANNE

Suisse
2013

To my family

Acknowledgements

Someone said "It's not the destination, but the journey that matters most". Well, right now I am very happy of having reached the destination!

I would like to express my greatest gratitude to my supervisor Prof. L. Rivkin for fostering the conclusion of this work. I am particularly grateful to M. Magistris for his precious help all along the thesis work, from the conceptual inception, through ongoing advice and encouragement, to this day. I would like to thank M. Silari and the whole CERN Radiation Protection group for giving me the opportunity to take part into the Marie Curie RADENV project, to M. Benedikt and the other members of the beta-beam collaboration task for their contributions to this work, especially P. Delahaye and E. Boucquerel. I would also like to thank F. Cerutti and A. Mairani for the help with theoretical understanding, S. Fortsch and J.P. Mira for the irreplaceable support in the experimental part of the work and G. White for the extraordinary editorial job.

Many people have accompanied me in the journey exchanging interesting ideas and thoughts, sharing bad and good moments. I would like to thank them all, also those that I am going to forget... In no particular order: Sophie Mallows, Zuzana Zajacova, Egidio Mauro, Alessio Mereghetti, Luca Timeo, Stefano Rosati, Nuno Jacinto, Giacomo Sacchetti, Chris Theis, Paola Solevi, Leonardo Sala, Silva Bortolussi, Marta Filibian and the unbeatable team of *The Dudes*. A special thanks goes to my family and Greg for their undivided support.

S.T.

Abstract

This thesis assesses the radiological risks and environmental impact of a future beta-beam facility at CERN.

Beta beams will produce neutrino and anti-neutrino beams through the β^\pm decay of radioactive ions, accelerated from 8 keV per nucleon to 92 GeV per nucleon, along a chain of accelerators that includes existing machines (the CERN proton synchrotron and the super proton synchrotron) and new machines (a rapid cycling synchrotron and a decay ring for the storage of the ions that will then decay into neutrinos and anti-neutrinos). The primary ion beams considered in this study are ${}^6\text{He}$ and ${}^{18}\text{Ne}$. In comparison to other neutrino facilities, for instance CNGS, beta beams presents different types of radiological risk, due to the decay products of the radioactive primary beams. These products have, in fact, a different charge-to-mass ratio with respect to the primary ions and are lost in the machine components. In addition, other losses contribute to the overall radiation field of the accelerator complex: injection, acceleration, RF-capture and collimation.

This thesis predicts the prompt and induced radiation in the facility and estimates the necessary countermeasures to protect the public and personnel, according to the CERN Safety Code. The thesis reviews the analytical models commonly used for the calculation of neutrons streaming through shielding walls and for the diffusion of radionuclides in air. The present work provides information on beam loss assumptions, accelerator design and material chemical compositions, and provides results of sufficiently general interest for ion accelerators in a rather wide energy range.

This work also summarizes some capabilities of the Monte Carlo code FLUKA, used to simulate the transport and interaction of ions. For comparison a study with data available in the literature for the production of secondary neutron spectra is included. In addition, this work shows a comparison study between the secondary neutron spectra produced by ions and those produced by protons of the same energy, normalized to the mass number of the ions. A benchmark framework and measurements performed to test the capability of the code in predicting the production of secondary ions in low-energy nuclear reactions are presented. The conclusion strongly indicates the feasibility of the future beta-beam facility at CERN from the point of view of radiation protection.

Keywords: radioactive ions, accelerators, prompt radiation, induced radioactivity, nuclear reactions, shielding design, airborne radioactivity, residual dose rates.

Résumé

Cette thèse évalue les risques radiologiques d'une future installation pour faisceaux bêta au CERN et son impact sur l'environnement. Beta beams va produire des faisceaux de neutrinos et anti-neutrinos par décroissance β^\pm des ions, qui sont accélérées à partir de 8 keV par nucléon jusqu'à 92 GeV par nucléon, le long d'une chaîne d'accélérateurs qui comprend machines déjà existantes au CERN (le synchrotron à proton et le super synchrotron à proton) et aussi des nouvelles machines (le synchrotron rapidement pulsé et l'anneau de décroissance pour le stockage des ions qui se désintègrent en neutrinos et anti-neutrinos). Les ions primaires considérés dans cette étude sont le ^6He et le ^{18}Ne . En comparaison à d'autres installations pour produire les neutrinos, comme, par exemple, CNGS, les beta beams présentent des risques radiologiques différents, en raison des produits de décroissance des ions primaires. Ces produits ont en effet une autre rapport charge-masse par rapport aux ions primaires et sont perdus dans la machine. En outre, d'autres pertes contribuent au champ de radiation autour du complexe d'accélérateurs : injection, accélération, capture RF et pertes de collimation.

Cette thèse prédit la radiation instantanée et induite dans les accélérateurs et estime les contre-mesures nécessaires pour protéger le public et le personnel, selon le Code de la sécurité du CERN. La thèse examine les modèles analytiques les plus communément utilisées pour le calcul de neutrons qui passent à travers le blindage et pour la diffusion des radionucléides dans l'air. Cette thèse fournit des informations sur les hypothèses de pertes de faisceau, le design des accélérateurs et les compositions chimiques des matériaux, fournissant des résultats d'intérêt générale pour les accélérateurs d'ions dans une gamme d'énergie assez large.

Cette thèse résume également des capacités du code Monte Carlo FLUKA, qui est utilisé pour la simulation du transport et des interactions des ions. De plus, une étude comparative entre les spectres secondaires produites par des ions et ceux produits par des protons de même énergie, normalisés au nombre de nucléons des ions, sont présentés. Il présente aussi un'étude comparatif entre les spectres des neutrons secondaires provenant de données disponibles en littérature et ceux prédits par le code et les résultats des mesures effectuées pour tester la capacité du code de prédire la production d'ions secondaires, pour les réactions nucléaires de énergie faible.

La conclusion du travail de thèse indique clairement la faisabilité de la future installation beta beams au CERN, du point de vue de la radioprotection.

Mots-clés : ions radioactives, accélérateurs, radiation instantanée, réactions nucléaires, blindage, radioactivité dans l'air, débit de dose résiduelle.

Contents

Acknowledgements	v
Abstract (English/Français)	vii
List of figures	xiii
List of tables	xx
1 Introduction	1
2 The beta beams	5
2.1 Neutrino oscillations	5
2.2 Experimental set-ups	6
2.3 New concepts in neutrino beams	6
2.3.1 Choice of ions	8
2.3.2 Physics potential and impact on possible measurements	9
2.4 Beta beams at CERN: feasibility study	10
2.4.1 Accelerator chain	10
2.4.2 Losses along the accelerator chain	12
2.5 Conclusion of the feasibility study	14
3 Theoretical framework	17
3.1 Radiation protection at ion accelerators: nuclear reactions and theoretical models	17
3.2 General features of the Monte Carlo code FLUKA	18
3.3 The Boltzmann Master Equation theory	20
3.4 Comparison with experimental data	21
3.4.1 $^{20}\text{Ne}+^{63}\text{Cu}$ at 100 MeV/u	22
3.4.1.1 Experimental set-up	22
3.4.1.2 Simulations and results	23
3.4.2 $^{16}\text{O}+^{12}\text{C}$ at 14.7 MeV/u	24
3.4.2.1 Experimental set-up	25
3.4.2.2 Simulations and results	27
3.4.3 Conclusions	29
3.5 Comparison between protons and ions	32

4	Radiation protection parameters and methods	35
4.1	Radiation protection aspects	35
4.1.1	Quantities and units in radiation protection	36
4.1.2	Radiation protection at CERN	40
4.2	Monte Carlo calculations and analytical methods	42
4.2.1	Prompt radiation and shielding: models and biasing techniques	42
4.2.1.1	Point source and line of sight model	42
4.2.1.2	Biasing	43
4.2.2	Induced activity: residual doses, radionuclide inventory, airborne activity	45
4.2.2.1	Residual doses and radionuclide inventory	46
4.2.2.2	Air activation	46
4.3	Conclusions	49
5	The Rapid Cycling Synchrotron (RCS)	51
5.1	Beam losses	52
5.2	Shielding calculations	53
5.3	Induced activity	57
5.3.1	Air activation	60
5.3.1.1	Dose to the reference population	60
5.3.1.2	Inhalation dose and external exposure to activated air for workers	61
5.3.2	Residual Doses	62
5.3.3	Possible countermeasures to high residual doses	66
5.4	Summary and conclusions	66
6	The Proton Synchrotron (PS)	69
6.1	Beam losses	70
6.2	Shielding calculations	70
6.3	Induced activity	73
6.3.1	Air activation	74
6.3.1.1	Dose to the reference population	74
6.3.1.2	Inhalation dose and external exposure to activated air for workers	77
6.3.2	Residual Doses	78
6.4	Summary and conclusions	84
7	The Decay Ring (DR)	87
7.1	Beam losses	88
7.2	Shielding calculations	90
7.2.1	Point-loss approximation	92
7.2.2	MC simulation with real loss maps	94
7.3	Induced Activity	96
7.3.1	Air activation	98
7.3.1.1	Dose to the reference population	98
7.3.1.2	Inhalation dose and external exposure to activated air for workers	101

7.3.2 Residual Doses	102
7.4 Summary and conclusions	107
8 Conclusions	109
A Residual dose rate maps in the RCS	113
B Residual dose rate maps in the DR	119
Bibliography	127
Curriculum Vitae	133

List of Figures

2.1	Beta-beam layout at CERN.	11
2.2	Cumulative ${}^6\text{He}$ and ${}^{18}\text{Ne}$ decays during acceleration.	13
3.1	Possible heavy-ion interaction processes, depending on the impact parameter b [68].	18
3.2	The FLUKA program flow for heavy ions [44].	20
3.3	The experimental set-up at HIMAC [49].	22
3.4	Double differential neutron spectra at 15° (top) and 30° (bottom).	24
3.5	Double differential neutron spectra at 60° (top) and 90° (bottom).	25
3.6	Left: scattering chamber with the two rotatable arms. Right: target frame.	26
3.7	Typical 2D PID spectra for heavy IMFs with $Z \geq 5$, between T1A and T1B detectors [48].	27
3.8	Typical 2D PID spectra for IMF with $3 \leq Z \leq 4$ between T2A and T2B [48].	27
3.9	Mass function spectra extracted between T1A and T1B with the gates around the loci of O. These gates were used to calculate the double differential spectra of the respective isotope [48].	28
3.10	Mass function spectra extracted between T1A and T1B with the gates around the loci of F. These gates were used to calculate the double differential spectra of the respective isotope [48].	28
3.11	Double differential spectra of ${}^{17}\text{F}$ at 10° . Comparison between experimental data and theoretical prediction. The three components of the theoretical curve are fragments produced in complete fusion, inelastic scattering and in 3-body mechanism with incomplete fusion.	29
3.12	Double differential spectra of ${}^{17}\text{F}$ at 12° . Comparison between experimental data and theoretical prediction. The three components of the theoretical curve are fragments produced in complete fusion, inelastic scattering and in 3-body mechanism with incomplete fusion.	30
3.13	Double differential spectra of ${}^{17}\text{F}$ at 15° . Comparison between experimental data and theoretical prediction. The three components of the theoretical curve are fragments produced in complete fusion, inelastic scattering and in 3-body mechanism with incomplete fusion.	30

List of Figures

3.14	Double differential spectra of ^{17}O at 10° . Comparison between experimental data and theoretical prediction. The three components of the theoretical curve are fragments produced in complete fusion, inelastic scattering and in 3-body mechanism with incomplete fusion.	31
3.15	Double differential spectra of ^{17}O at 12° . Comparison between experimental data and theoretical prediction. The three components of the theoretical curve are fragments produced in complete fusion, inelastic scattering and in 3-body mechanism with incomplete fusion.	31
3.16	Double differential spectra of ^{17}O at 15° . Comparison between experimental data and theoretical prediction. The three components of the theoretical curve are fragments produced in complete fusion, inelastic scattering and in 3-body mechanism with incomplete fusion.	32
3.17	Representation of a beam line element, i.e. a magnet yoke around a beam pipe.	33
3.18	Neutron fluence at 100 MeV per nucleon at the boundary between the beam pipe and the magnet yoke. Comparison between ^6He ions and protons (intensity normalized to the ^6He intensity).	33
3.19	Neutron fluence at 100 MeV per nucleon at the boundary between the beam pipe and the magnet yoke. Comparison between ^{18}Ne ions and protons (intensity normalized to the ^{18}Ne intensity).	34
4.1	Recommended radiation weighting factors for neutrons as a function of neutron energy.	38
4.2	The ICRU sphere.	39
4.3	Point-source/Line of sight sketch.	43
4.4	Sketch for the approximation of a uniform loss with a point loss.	44
4.5	Pictorial representation of the <i>surface splitting</i> biasing technique.	45
5.1	Layout of the RCS.	51
5.2	Optical functions for one super-period [74].	52
5.3	Layout of the RCS with the different kinds of losses and their locations in the ring.	53
5.4	Intensities for decay (red) and RFC-acceleration (black) losses for ^6He (top) and for ^{18}Ne (bottom); the x-axis represents the position along the RCS circumference (m) and the y-axis the loss in arbitrary units on the left, in percentages of the injected beam intensity on the right.	54
5.5	Simplified geometry used for the calculation of the source terms and of the attenuation lengths in concrete. 3D visualisation with SIMPLGEO [76].	55
5.6	Attenuation curves in concrete at 90° for several ^6He -beam energies. The data are fitted by eq. (7.1) in Chapter 4.	55
5.7	Attenuation curves in concrete at 90° for several ^{18}Ne -beam energies. The data are fitted by eq. (7.1) in Chapter 4.	56
5.8	3D visualisation of the geometry of the injection area.	59
5.9	3D visualisation of the geometry of the electrostatic septum.	59
5.10	3D visualisation of the geometry of an arc section (top-view).	60

5.11 Annual effective dose to the reference population: contributions from the main radionuclides.	61
5.12 Residual dose rate profile near the septum as a function of the distance from the beam line, for the 3 waiting times, for ^{18}Ne	62
5.13 Specific activities (Bq/g) for some radionuclides produced in the beam pipe at the septum, given for the three waiting times (^{18}Ne operation).	63
5.14 Specific activities in Bq/g for some radionuclides produced in the coils in the quadrupole, given for the three waiting times (^{18}Ne operation).	64
5.15 Specific activities in Bq/g for some radionuclides produced in the beam-pipe inside the quadrupole, given for the three waiting times (^{18}Ne operation).	64
5.16 Specific activities in Bq/g for some radionuclides produced in the yoke in the quadrupole, given for the three waiting times (^{18}Ne operation).	65
5.17 Top: Residual dose rate after one week with both RFc-acceleration and decay losses. Bottom: Residual dose rate after one week with decay losses only.	67
6.1 The PS complex (from CERN PS webpage).	69
6.2 Decay losses in the PS, calculated via the Strahlsim code [81], for ^6He (top) and ^{18}Ne (bottom), at injection energy. The magnets are indicated in blue/magenta [24].	71
6.3 Attenuation curves in concrete for neon at the extraction energy of the PS.	71
6.4 Attenuation curves in concrete for helium at the extraction energy of the PS.	72
6.5 The PS tunnel section (original drawing).	73
6.6 Cross section of a combined-function magnet in the PS tunnel, as it is represented in the FLUKA simulations.	74
6.7 Characteristic lethargic spectra for secondary protons, pions and neutrons produced in the air by ^6He	75
6.8 Characteristic lethargic spectra for secondary protons, pions and neutrons produced in the air by ^{18}Ne	75
6.9 Contribution of airborne radionuclides to the total annual effective dose given to the reference population: comparison between the radionuclides produced by ^{18}Ne (purple) and by ^6He (blue).	77
6.10 Residual dose rate map for ^6He , one hour after the end of the yearly operation of the PS.	78
6.11 Residual dose rate map for ^6He , one day after the end of the yearly operation of the PS.	78
6.12 Residual dose rate map for ^6He , one week after the end of the yearly operation of the PS.	79
6.13 Residual dose rate profiles for ^6He , for three waiting times after the yearly operation of the PS. The profiles are taken at the worst loss point in the magnets.	79
6.14 Residual dose rate for ^{18}Ne , one hour after the end of the yearly operation of the PS.	80
6.15 Residual dose rate for ^{18}Ne , one day after the end of the yearly operation of the PS.	80

List of Figures

6.16 Residual dose rate for ^{18}Ne , one week after the end of the yearly operation of the PS.	81
6.17 Residual dose rate profiles for ^{18}Ne , for three waiting times after the yearly operation of the PS. The profiles are taken at the worst loss point in the magnets.	81
6.18 Specific activities of radionuclides produced in the beam pipe by ^6He	82
6.19 Specific activities of radionuclides produced in the yoke by ^6He : comparison between the C-shaped part and the poles.	83
6.20 Naming convention for the sections of the coils in the induced-activity calculations: “straight” (left and right) and “bent” (front and back).	83
7.1 Layout of the DR.	87
7.2 Optical functions in the arcs: in red horizontal betatron function, in blue vertical betatron function, in green dispersion function [24].	88
7.3 Loss amount as a function of injection cycles for ^6He (top) and ^{18}Ne (bottom)[24].	89
7.4 Overview of the energy deposition distribution (mW cm^{-3}) in the superconducting coils of the dipole in the lattice cell. The projection is averaged over the length of the magnet [24].	90
7.5 A representation of the FLUKA geometry of a cell in the arcs of the DR.	90
7.6 ^{18}Ne losses (blue) at the entrance (left) of the arc and in one cell (right), expressed in arbitrary units.	91
7.7 ^6He (left) and ^{18}Ne (right) losses in the first bump section, expressed in arbitrary units.	91
7.8 Power deposited in the collimation and in the bump sections by collimation losses: in blue for helium and in green for neon.	91
7.9 Attenuation curve in concrete at 90° for $92 \text{ GeV/u } ^{18}\text{Ne}$ ions on copper.	92
7.10 Attenuation curve in concrete at 90° for $92 \text{ GeV/u } ^6\text{He}$ ions on copper.	93
7.11 ^{18}Ne ambient dose equivalent rate map in one cell in the arcs (top view), expressed in μSvh^{-1} per unit primary particle.	94
7.12 ^{18}Ne ambient dose equivalent rate as a function of the distance Z in one cell in the arcs (top view), expressed in μSvh^{-1} per unit primary particle.	95
7.13 Detailed drawing of the cross sections of the coils of the dipoles in the DR, in the open mid-plane layout. The specifications for the material compositions can be found in Table 7.5.	96
7.14 Lattice of a bump section in the DR.	97
7.15 Warm quadrupole and dipole in the bumps as they are represented in the geometry of the simulations.	98
7.16 Track length spectra for protons, neutrons and pions produced in the air for ^{18}Ne operation.	99
7.17 Conversion coefficients from activity to dose for several stacks (ISOLDE, TT20, TT60, BA3): comparison between short-lived nuclides (top) and for long-lived nuclides (bottom).	100
7.18 Possible layout of the ventilation outlets in the DR.	100

7.19 Residual dose rates for the waiting times of 1 hour, 1 day and 1 week in one arc cell, for ^{18}Ne : layout with absorbers on left, layout with open mid-plane magnets on the right.	104
7.20 Residual dose rates for the waiting times of 1 hour, 1 day and 1 week in one arc cell, for ^6He : layout with absorbers on left, layout with open mid-plane magnets on the right.	105
7.21 Residual nuclides in the absorber, specific activities for ^{18}Ne operation.	106
7.22 Specific activities after one week in the dipole yoke, in the layouts with and without absorbers, for ^{18}Ne operation.	106
7.23 Residual dose-rate profile for ^{18}Ne operation at the dipole for several waiting times (open mid-plane layout).	107
A.1 Layout of the RCS with the different kinds of losses and their locations in the ring.	113
A.2 Residual dose rate map after one hour for ^6He , in the septum area.	114
A.3 Residual dose rate map after one day for ^6He , in the septum area.	114
A.4 Residual dose rate map after one week for ^6He , in the septum area.	114
A.5 Residual dose rate map after one hour for ^{18}Ne , in the septum area.	115
A.6 Residual dose rate map after one day for ^{18}Ne , in the septum area.	115
A.7 Residual dose rate map after one week for ^{18}Ne , in the septum area.	115
A.8 Residual dose rate map after one hour for ^6He , in the arcs for RFc-acceleration and decay losses.	116
A.9 Residual dose rate map after one day for ^6He , in the arcs for RFc-acceleration and decay losses.	116
A.10 Residual dose rate map after one week for ^6He , in th arcs for RFc-acceleration and decay losses.	116
A.11 Residual dose rate map after one hour for ^{18}Ne , in the arcs for RFc-acceleration and decay losses.	117
A.12 Residual dose rate map after one day for ^{18}Ne , in the arcs for RFc-acceleration and decay losses.	117
A.13 Residual dose rate map after one week for ^{18}Ne , in th arcs for RFc-acceleration and decay losses.	117
B.1 The layout of the DR with the names of the main sections.	119
B.2 Residual dose rate maps for the waiting times of 1 hour, 1 day and 1 week in one arc cell, for ^{18}Ne : layout with absorbers on left, layout with open mid-plane magnets on the right.	120
B.3 Residual dose rate maps for the waiting times of 1 hour, 1 day and 1 week in one arc cell, for ^6He : layout with absorbers on left, layout with open mid-plane magnets on the right.	121
B.4 Residual dose rate maps for the waiting times of 1 hour, 1 day and 1 week in the collimation section, for ^{18}Ne	122
B.5 Residual dose rate maps for the waiting times of 1 hour, 1 day and 1 week in the collimation section, for ^6He	123

List of Figures

B.6	Residual dose rate maps after one hour for ^{18}Ne , in the second bump, in the second quadrupole (worst case).	124
B.7	Residual dose rate maps after one day for ^{18}Ne , in the second bump, in the second quadrupole (worst case).	124
B.8	Residual dose rate maps after one week for ^{18}Ne , in the second bump, in the second quadrupole (worst case).	124
B.9	Residual dose rate maps after one hour for ^6He , in the second bump, in the first bending magnet (worst case).	125
B.10	Residual dose rate maps after one day for ^6He , in the second bump, in the first bending magnet (worst case).	125
B.11	Residual dose rate maps after one week for ^6He , in the second bump, in the first bending magnet (worst case).	125

List of Tables

2.1	β^- candidate emitters for the parent ions.	8
2.2	β^+ candidate emitters for the parent ions.	9
2.3	Top-down approach beam intensities in the beta-beam facility.	13
2.4	Summary of decay losses in all the machines.	13
2.5	Comparison between CNGS total losses and beta-beam decay losses.	14
4.1	Radiation weighting factors according to ICRP 103.	38
4.2	Radiation weighting factors w_T per organ group, according to ICRP 103.	39
4.3	CERN Radiation Safety Code: classification of radiation areas	41
5.1	Main parameters of the ring.	52
5.2	Loss percentages for several energies and for the production mechanism for ^6He (^{18}Ne).	53
5.3	Attenuation lengths in concrete and source terms for several energies in the machine range.	56
5.4	Concrete shield thicknesses for injection losses. The values in parentheses represent the recommended values.	57
5.5	Concrete shield thicknesses for decay losses. The values in parentheses represent the recommended values.	57
5.6	Concrete shield thicknesses for RfC+acceleration losses.	58
5.7	Concrete shield thicknesses for RfC+acceleration and decay losses.	58
5.8	Annual effective dose given to the reference population for several combinations of F and T_{decay}	61
5.9	Inhalation and external-exposure dose to workers for several irradiation and waiting times, coming from induced activity in the air.	62
5.10	Residual dose rates at 1 m from the loss points (mSv h^{-1}) for ^{18}Ne operation.	65
5.11	Residual dose rates at 1 m from the loss points (mSv h^{-1}) for ^6He operation.	66
6.1	Main parameters of the ring within beta beams.	69
6.2	Source terms H_0 (Sv m^2 per primary ion) and attenuation lengths λ_θ in concrete (g cm^{-2}) for ^{18}Ne and ^6He at the extraction energies.	72
6.3	Concrete shield thickness for decay losses of ^{18}Ne and ^6He . The values in parentheses contain a safety margin.	72

List of Tables

6.4	Contribution to the total annual effective dose of the most relevant radionuclides produced by air activation in the PS tunnel during a one-year ^6He operation and released into the environment.	76
6.5	Contribution to the total annual effective dose of the most relevant radionuclides produced by air activation in the PS tunnel during a one-year ^{18}Ne operation and released into the environment.	76
6.6	Inhalation and external-exposure dose to workers for several irradiation and waiting times, coming from induced activity in the air.	77
6.7	Total and specific activities of radionuclides produced in the beam pipe by ^6He , for the waiting times of 1 hour, 1 day and 1 one week. Only the radionuclides with a total activity higher than 10 MBq are listed.	82
6.8	Total and specific activities of radionuclides produced in the coils by ^6He , for the waiting times of 1 hour, 1 day and 1 one week: comparison between the straight and bent sections.	84
7.1	Main parameters of the ring.	87
7.2	Source terms H_0 (Sv m^2 per primary ion) and attenuation lengths λ_θ in concrete (g cm^{-2}).	93
7.3	Maximum shielding thicknesses for the ^{18}Ne operation in the DR, for each machine section. An extra attenuation length is included in the thickness. . . .	93
7.4	Maximum shielding thicknesses for the ^6He operation in the DR, for each machine section. An extra attenuation length is included in the thickness.	94
7.5	Coil composition (volume fraction in %) in the cold magnets in the arcs.	97
7.6	Yoke composition (weight fractions) in the cold magnets in the arcs.	97
7.7	Yoke composition in warm magnets in the bumps in %.	98
7.8	Contribution to the total annual effective dose from losses in the first arc during ^{18}Ne operation. $F = 20000 \text{ m}^3$, $\text{Vol}_{out} = 31252.4 \text{ m}^3$ (outlet located after the first SS).	101
7.9	Contribution to the total annual effective dose from losses in the second arc for ^{18}Ne operation. $F = 20000 \text{ m}^3$, $\text{Vol}_{out} = 31252.4 \text{ m}^3$ (outlet located after the second SS).	102
7.10	Contribution to the total annual effective dose released in the environment, due to losses in the bumps and the collimation section. $F = 20000 \text{ m}^3$, $\text{Vol}_{out}^{bump1} = 86620.4 \text{ m}^3$, $\text{Vol}_{out}^{coll} = 78012.4 \text{ m}^3$, $\text{Vol}_{out}^{bump2} = 73287.4 \text{ m}^3$ (outlet located after the SS).	103
7.11	Inhalation and external-exposure dose to workers for several irradiation and waiting times, coming from induced activity in the air.	103

1 Introduction

Beta beams will produce neutrino and anti-neutrino beams through beta-decaying ions, which are accumulated in a high-energy storage ring. Until now, the use of radioactive ions as primary beams has been regarded as a safety issue. This thesis is to objectively establish the actual radiological risks of beta beams with respect to safety.

Beta beams will be a chain of accelerators that cover the range from 8 keV per nucleon up to 92 GeV per nucleon. This work focuses on the intermediate- and high-energy ranges, starting from 100 MeV per nucleon, because of their relevance for safety aspects. There is a wide range of type and origin of beam losses: injection and extraction, merging, radio-frequency capture and acceleration, beam-gas interaction, collimation and above all decay. Despite the facility being optimized to have most of the decay losses in the storage ring, decays in the upstream machines are unavoidable. The interaction of lost particles with the machine components generates prompt radiation and induced activity. In order to guarantee the feasibility of the beta-beams at CERN, technical solutions to reduce these two radiological aspects are necessary.

The second chapter, after an overview of neutrino experiment history and the status of the existing experiments, justifies the need for a new facility like beta beams and examines its impact on possible physics measurements. It then describes the layout of an ideal facility to be installed at CERN, assessing the possibility to use existing machines. Finally, it shows the expected loss distribution along the accelerator chain and the total power deposited in a year on the machine components. These values are compared with those of the CERN Neutrino Gran Sasso (CNGS) facility. CNGS, unlike beta beams, produces neutrinos from the decay of pions and kaons. It can be nevertheless regarded as a comparable facility in terms of purpose, intensity and level of technology.

Experimental data on secondary particles generated by the interaction of ions with matter are still scarce and only Monte Carlo (MC) calculations, that use models based on the interpolation of the existing data, are possible. In the third chapter, the MC code FLUKA, used for the calculations, is presented in its general features and in particular in its capability of describing

Chapter 1. Introduction

nucleus-nucleus interaction physics. The models for high-energy interactions implemented in the code for these reactions have been already benchmarked. However, the low-energy model, which is based on the Boltzmann Master Equation theory, is still under development. It applies to reactions occurring below 100 MeV per nucleon, which corresponds to the injection energy into the circular accelerators in beta beams. In order to validate the model for present calculations, two benchmark studies are described. The first one is a comparison between simulations and available data coming from measurements performed at HIMAC, in Japan, on neutron spectra produced by ^{20}Ne ions hitting a thick copper target. The second one concerns an experiment performed at the IThemba Labs, in South Africa, where the intermediate-mass fragments produced in the $^{16}\text{O}+^{12}\text{C}$ reaction at 14.7 MeV per nucleon were measured. The theoretical predictions are compared with the collected experimental results.

The fourth chapter is an overview of all the methods used for the risk assessment calculations. After an introduction to the quantities and units used in radiation protection studies, the specific radiation protection framework used at CERN is briefly presented. This framework is based on the CERN Safety Code, on the Swiss and French legislation, and it has precise dose-rate guidelines and limits for the emissions into the environment. The calculation methods for estimates of induced-activity are then described in detail. For high-density materials, the yields of the residual nuclides produced in the activation process and the residual doses can be assessed with a set of MC simulations. For gaseous media like air, because of their low inelastic-interaction probability, the activity must be calculated analytically. In particular, the predicted track-length spectra of protons, neutrons and pions in the air are convoluted with isotope-production cross sections. The analytical model for the air diffusion from the accelerator tunnels to the environment is fully described. Several methods for shielding calculations can be found in the literature. They are based on assumptions that aim at simplifying the calculations when complex geometries are involved. In the case of thick shielding walls, biasing techniques are also recommended to compensate for the absorption of particles in matter and to reduce the statistical error. An overview of the most common biasing methods and the ones used for the calculations in this thesis are shown.

In the following chapters all the results of the calculations performed for the Rapid Cycling Synchrotron (RCS, Chapter 5), the Proton Synchrotron (PS, Chapter 6) and the Decay Ring (DR, Chapter 7) are described. The RCS is the first of the circular machines in the beta-beam chain and it bunches and accelerates the beams up to an energy of 2.5 GeV proton-equivalent. Decay losses are uniformly distributed in the ring and represent a small fraction of the total losses. A high percentage of the beam is lost at injection and during acceleration, giving rise to high doses close to the injection septum and to the quadrupole families in the arcs. Ad-hoc solutions to reduce the acceleration losses have been considered. After the RCS, the beam is injected into the PS, one of the oldest accelerators in use at CERN. As its operation for the beta beams does not entail a re-design of the machine, attention is paid to key maintenance and safety parameters, like the coil lifetimes, the residual doses during interventions and the airborne activity impact on the environment. The beam undergoes its last acceleration in the SPS, up to the final energy of 92 GeV per nucleon. Data on expected beam losses in the

SPS were not available at the time this thesis was written. Therefore this study does not cover the radiological risks associated with SPS. In the DR, (i.e. the high-energy storage ring), the beam is not further accelerated but accumulated before decaying. The quasi-totality of the losses is due to collimation and decay. The sections which are mainly affected by these losses are the arcs, collimator and bump areas. All the radiation protection aspects are considered, including the shielding thickness in the tunnel. A comparison between the thickness obtained with the simplified model described in the Chapter 3 and that calculated with MC simulations is presented. Chapter 8 summarizes the most important results achieved in this work with an overview of the more general achievements of the beta-beam design study and its future prospects.

2 The beta beams

Beta beams are a new concept for a neutrino factory, aimed at producing pure electron neutrino-antineutrino ($\nu_e - \bar{\nu}_e$) beams through the β^\pm decay of radioactive ions circulating in a high-energy storage ring [1]. The demand for better neutrino beams is correlated with the considerable improvement in neutrino detectors, and to the recent exciting claims of evidence for neutrino oscillations by various experiments. The current theoretical understanding is not able yet to accommodate in a unique picture the oscillations of neutrinos with different origins, namely solar, atmospheric and accelerator neutrinos and decisive experiments are needed. A high-intensity neutrino source of a single flavor, improved backgrounds and known energy spectrum and intensity would enable both oscillation searches and precision measurement of the lepton mixing parameters. The beta beams would therefore represent such a source of single flavor neutrinos.

2.1 Neutrino oscillations

The observation of neutrino oscillations, besides proving that neutrinos have mass and mix, also represents the basis for requiring physics beyond the Standard Model. The oscillation is a quantum-mechanical phenomenon, predicted by Bruno Pontecorvo [2], according to which neutrinos can undergo a change in their flavors (electron, muon and tau) from production to measurement. In the early 1970s the chlorine solar experiment [3] demonstrated that electron neutrinos detected on earth were indeed fewer than expected. A further confirmation came in the 1980s from the water Čerenkov KamiokaNDE experiment [4], which was able to demonstrate that the collected signals were coming from the sun. Even if relevant, these two experiments were not considered evidence for neutrino oscillation because based on theoretical predictions: only in 2002 SNO [5] and KamLAND [6] were able to assess in a model-independent way that the total neutrino flux on earth was as expected while the electron neutrino flux was depleted.

2.2 Experimental set-ups

All along the history of neutrino experiments, four main categories of experimental set-ups can be defined: conventional, first and second generation long-baseline, next generation experiments.

Conventional neutrino beams are produced through high-energy proton beams hitting small Z , very thin and segmented targets: the produced π and K mesons are focused (or defocused) by large magnetic lenses into a long tunnel where they decay into ν_μ - $\bar{\nu}_\mu$'s. The length of the tunnel is optimized in order to maximize pion decays. The charged mesons are dumped downstream the tunnel whilst high energy muons are stopped by the earth. The neutrino beam is of course contaminated by $\bar{\nu}_\mu$, ν_e and $\bar{\nu}_e$ but this can be evaluated through the knowledge of the π and K production in the primary beam target. Closed detectors are used to measure neutrino beams and background. Among conventional beams it is possible to distinguish between a first and a second generation.

Long-baseline experiments (LBL) are devoted to confirm the atmospheric evidence of oscillations and measuring mixing angles ($\sin^2 2\theta_{23}$) and mass differences (Δm_{23}^2). The first experiment was K2K at KEK [7] and it confirmed the atmospheric oscillation at the SuperKamiokande detector (at 4.3σ): it had a baseline of 250 km and produced 1.2 GeV (on average) neutrinos. The main results supported maximal mixing. Another noticeable LBL experiment, supporting maximal mixing, is MINOS (Main Injector Neutrino Oscillation Search) [8], producing a neutrino beam from Fermilab to the Soudan mine in Minnesota. Both these two experiments aim at improving the knowledge of oscillation parameters and probing the third mixing angle. ICARUS [9] and OPERA [10], at the CNGS beam [11] from CERN, intend to prove the $\nu_\mu \rightarrow \nu_\tau$ oscillations.

Second generation long-baseline experiments, namely T2K [12] and NOvA [13], will measure θ_{13} by detecting sub-leading $\nu_\mu \rightarrow \nu_e$ oscillations. Another approach for this measurement is being explored at nuclear reactors by observing the disappearance of $\bar{\nu}_e$. But, as T2K and NOvA, even combined with a reactor experiment, cannot give established results about leptonic CP violation, a next-generation of long-baseline neutrino experiments that can provide more sensitive results are needed. In order to achieve this, neutrino super beams and gigantic detectors must be built: T2K phase II, called T2HK, will increase its beam power (up to 4 MW) and build a 520 kt water Čerenkov detector. A CNGS upgrade has been also computed and new projects are under study, i.e. CERN-SPL super beam [14, 15] and a wide-band beam (WBB) at BNL [16, 17] which would offer a higher flux and a broad energy spectrum.

2.3 New concepts in neutrino beams

Conventional neutrino beams have two main intrinsic limitations: the precision in the measurement of the neutrino hadroproduction at the target and the background given by the "unwanted" flavors. If the neutrino parents are fully selected, collimated and accelerated,

several improvements with respect to conventional neutrino beams can be achieved: the neutrino fluxes can be derived from the number of parents circulating in the accelerator and from their Lorentz boost factor γ . Furthermore the background arising from other flavors is suppressed or reduced to wrong sign muons. But also this new method of producing neutrinos presents some drawbacks, in terms of technological problems: the parents need to be unstable particles that require a fast acceleration scheme. This can be attained in two ways: with muon decay within neutrino factories or with beta decaying ions within beta beams. With this kind of beams there is no need to perform a hadroproduction experiment because neutrino fluxes at the close and far detectors are fully predictable.

In the beta-beam facility study, the candidates for primary ions are ${}^6\text{He}$ and ${}^{18}\text{Ne}$, whose decay reactions are:



and the decay branching ratio is the unity in both cases.

The flux of neutrinos reaching the far detector is an important feature of the facility. For example, in the ${}^6\text{He}$ case, the Q value, or endpoint kinetic energy of the beta particle, is 3.5078 MeV and the average energy of the emitted neutrino is 1.937 MeV. The emission is isotropic since the parent ion is spinless. With an acceleration to $\gamma=150$, which is the maximum achievable by using the Super Proton Synchrotron (SPS) at CERN, in the forward direction, the center-of-mass neutrino energy corresponds to the one at rest multiplied by 2γ [18], therefore at the far detector it will be 581 MeV. The typical decay angle of a neutrino is $\frac{1}{\gamma}$ and as the lateral dimensions of the detector are much smaller than $\frac{L}{\gamma}$, where L is the distance, it is possible to conclude that the neutrino spectrum has no radial dependence. The flux Φ at the detector is proportional to $\frac{\gamma^2}{L^2}$ and for a distance $L=100$ km it would be $7.2\text{E-}7$ m^{-2} per parent ion. The candidate site is the Frejus mountain, which can host a megaton class detector, at a distance of 130 km from CERN. Considering a muon-based neutrino factory, under the same distance and γ conditions, the neutrino flux at the detector would be of $5.7\text{E-}9$ m^{-2} , i.e. 128 times less than in beta beams.

Another important parameter to consider is the number of neutrino interactions when $\langle E \rangle / L \approx \Delta m^2$, where E is the average neutrino energy. This parameter describes the collected statistics in an oscillation disappearance experiment and indicates the appearance signal intensity, since:

$$I \propto \sin^2\left(1.27 \frac{\Delta m^2 L}{E}\right). \quad (2.3)$$

For electron and muon neutrinos in the considered energy range, it is possible to assume neutrino cross-sections proportional to neutrino energy; as the focusing of the neutrino beam

Chapter 2. The beta beams

only depends on γ , the interaction rate in the far detector is:

$$N_{int} \propto (\Delta m^2)^2 (1.27 \frac{\gamma}{E_{cms}}), \quad (2.4)$$

where E_{cms} is the neutrino energy in the frame when the parent is at rest. γ/E_{cms} is the quality factor that characterizes the neutrino beam and its interaction probability. A ${}^6\text{He}$ beam, accelerated to $\gamma=150$, is five times more efficient than a neutrino beam from muons at $\gamma=500$.

2.3.1 Choice of ions

The beta-beam concept for the generation of a ν_e and $\bar{\nu}_e$ beam was proposed in 2002 [19, 20]. The study for the choice of the parent ions, relevant for the design of the entire facility and its performances, was influenced by several aspects: the efficiency in production rate, the need of small Z ions in order to store higher intensities in the decay ring, just to mention some. Also the necessity of a compromise in between a half-life short enough to obtain a high-energy decay and long enough to accumulate the desired number of ions in the decay ring affected the final choice of ions. In the end, a list of candidate ions was established, whose characteristics are summarized in Tables 2.1, for the β^- emitters, and 2.2, for the β^+ emitters.

	A/Z	$\tau_{1/2}$ (s)	Q_β (MeV) (ground state)	Q_β (MeV) (effective)	E_β (MeV) (average)	E_ν (MeV) (average)
${}^6\text{He}^{2+}$	3.0	0.8	3.5	3.5	1.57	1.94
${}^8\text{He}^{2+}$	4.0	0.11	10.7	9.1	4.35	4.80
${}^8\text{Li}^{3+}$	2.7	0.83	16.0	13.0	6.24	6.72
${}^9\text{Li}^{3+}$	3.0	0.17	13.6	11.9	5.73	6.20
${}^{11}\text{Be}^{4+}$	2.8	13.8	11.5	9.8	4.65	5.11
${}^{15}\text{C}^{6+}$	2.5	2.44	9.8	6.4	2.87	3.55
${}^{16}\text{C}^{6+}$	2.7	0.74	8.0	4.5	2.05	2.46
${}^{16}\text{N}^{7+}$	2.3	7.13	10.4	5.9	4.59	1.33
${}^{17}\text{N}^{7+}$	2.4	4.17	8.7	3.8	1.71	2.10
${}^{18}\text{N}^{7+}$	2.6	0.64	13.9	8.0	5.33	2.67
${}^{23}\text{Ne}^{10+}$	2.3	37.2	4.4	4.2	1.90	2.31
${}^{25}\text{Ne}^{10+}$	2.5	0.6	7.3	6.9	3.18	3.73
${}^{25}\text{Na}^{11+}$	2.3	59.1	3.8	3.4	1.51	1.90
${}^{26}\text{Na}^{11+}$	2.4	1.07	9.3	7.2	3.34	3.81

Table 2.1: β^- candidate emitters for the parent ions.

Q_β represents the energy difference between the parent and daughter ground states. ${}^6\text{He}$ and ${}^{18}\text{Ne}$ were selected, as both isotopes can be easily produced, they are noble gases chemically inert and easy to handle, and they do not produce dangerous long-lived daughter products that could create concern in the low-energy part of the facility.

	A/Z	$\tau_{1/2}$ (s)	Q_β (MeV) (ground state)	Q_β (MeV) (effective)	E_β (MeV) (average)	E_ν (MeV) (average)
${}^8\text{B}^{5+}$	1.6	0.77	17.0	13.9	6.55	7.37
${}^{10}\text{C}^{6+}$	1.7	19.3	2.6	1.9	0.81	1.08
${}^{14}\text{O}^{8+}$	1.8	70.6	4.1	1.8	0.78	1.05
${}^{15}\text{O}^{8+}$	1.9	122.0	1.7	1.7	0.74	1.00
${}^{18}\text{Ne}^{10+}$	1.8	1.67	3.3	3.0	1.50	1.52
${}^{19}\text{Ne}^{10+}$	1.9	17.3	2.2	2.2	0.96	01.25
${}^{21}\text{Na}^{11+}$	1.9	22.4	2.5	2.5	1.10	1.41
${}^{33}\text{Ar}^{18+}$	1.8	0.17	10.6	8.2	3.97	4.19
${}^{34}\text{Ar}^{18+}$	1.9	0.84	5.0	5.0	2.29	2.67
${}^{35}\text{Ar}^{18+}$	1.9	1.77	4.9	4.9	2.27	2.65
${}^{37}\text{K}^{19+}$	1.9	1.22	5.1	5.1	2.35	2.72
${}^{80}\text{Rb}^{37+}$	2.2	34.0	4.7	4.5	2.04	2.48

 Table 2.2: β^+ candidate emitters for the parent ions.

2.3.2 Physics potential and impact on possible measurements

With respect to other experiments, beta beams offer perfectly known intensity and spectrum of the source. Such characteristics are important in disappearance measurements which have the advantage of being sensitive to oscillation. In particular, when Δm^2 is comparable with $\langle E \rangle / L$, the experiment is apt to measure the $\bar{\nu}_e$ disappearance with high precision and sensitivity only limited by statistics. The sensitivity is still good even when Δm^2 is much larger than $\langle E \rangle / L$, but becomes compromised when Δm^2 is smaller than $\langle E \rangle / L$, which corresponds to a detector too close to the source. For a disappearance experiment with beta beams a simple very large electromagnetic calorimeter, capable of measuring the energy of one electron, would be enough. Synchronization with the pulsed structure of the decay ring would minimize the backgrounds. A large water Čerenkov detector could be used.

Appearance experiments, instead, would be limited to muon neutrino observation, as for tau production a high energy is needed and therefore a larger decay ring and an increased storage time because of the lifetime dilatation. Muon neutrino appearance experiments with beta beams have a big possibility, connected with the absence of other flavors in the beams: the far detector can be similar to the ones designed for proton decay experiments, i.e. again a large water Čerenkov. The aim is to distinguish between a minimum-ionization track from an electron shower, without the need of charge identification of the final-state lepton. On the contrary, this is necessary in a muon neutrino factory, where a magnetic field allows separating the background induced by neutrinos of the same flavor but opposite lepton number.

Considering precision measurements, beta beams are of interest for nuclear studies with neutrinos, given the high intensity and the purity of the beams, but only in the low-energy domain. Deep inelastic neutrino interactions are therefore excluded, but cross sections on

different targets of ν_e and $\bar{\nu}_e$ from astrophysical sources can be measured.

Finally, in CP-violation measurements, the beta beams have lower energy and better focusing with respect to a muon neutrino factory, which permits to explore a larger domain of $\langle E \rangle / L$ values.

2.4 Beta beams at CERN: feasibility study

The study performed in 2002 also explored the possible use of existing CERN machines for the acceleration of radioactive ions to a relativistic Lorentz γ of roughly 100 for storage in a new decay ring of approximately the size of SPS. The results from this first short study were very encouraging, and in 2004 it was decided to incorporate a design study for the beta beams within the EURISOL DS proposal [21]. The study aimed at producing feasibility studies and performing technical preparatory work of the most critical parts of the future EURISOL facility. Three possible sites were identified for the construction of the facility: an existing national laboratory, an intergovernmental one like CERN to enable sharing of expensive infrastructure such as the driver and a green-field site in a less favored region within the European Union with support for the construction from EU structural funds. The design study officially started 1 February 2005 and ran for four years. The study proposed to use a thick ISOL (isotope separation on-line) target for the production of ${}^6\text{He}$ and ${}^{18}\text{Ne}$. A high frequency (60 GHz) ECR source was identified as a possible highly efficient tool to create sufficiently short bunches after the target for multi-turn injection into a synchrotron. For the first stage of acceleration, it was proposed to use a 100 MeV-per-nucleon LINAC, for the further acceleration a new rapid cycling synchrotron (RCS), the Proton Synchrotron (PS) and the SPS. For the storage at high-energy a Decay Ring (DR) was proposed, with a new injection and stacking method. In the framework of the feasibility study, beside the efficiency in production, acceleration and storage of the ions, also the analysis of the impact of such facility at CERN in terms of radiological risk was started. The main concern was related to the use of radioactive ions as primary beam and to their decay products distributed all along the accelerator chain.

2.4.1 Accelerator chain

The layout of a possible beta-beam accelerator chain at CERN is shown in Figure 2.1. In order to attain an optimal sensitivity to the θ_{13} angle and CP violating phase, $1.1\text{E}19$ neutrinos and $2.9\text{E}19$ antineutrinos represent the desired throughput over a 10-year operation. This translates into a production of $2\text{E}13$ ${}^6\text{He}$ ions per second and $1\text{E}13$ ${}^{18}\text{Ne}$ ions per second. The methods envisaged for the ion production are: a ${}^9\text{Be}(n,\alpha){}^6\text{He}$ reaction, through a 2 GeV proton beam onto a neutron converter surrounding a BeO target, for ${}^6\text{He}$, and a ${}^{16}\text{O}({}^3\text{He},n){}^{18}\text{Ne}$ reaction, through a 14.8 MeV ${}^3\text{He}$ beam onto a MgO target, for ${}^{18}\text{Ne}$. After the production section, a normal-conducting LINAC with 100 MeV per-nucleon is foreseen. It is based on NC-RF structures and it can tolerate the thermal load created by the high-pulse beam current required by beta beams (up to 13 mA). It delivers fully stripped helium ions at a magnetic

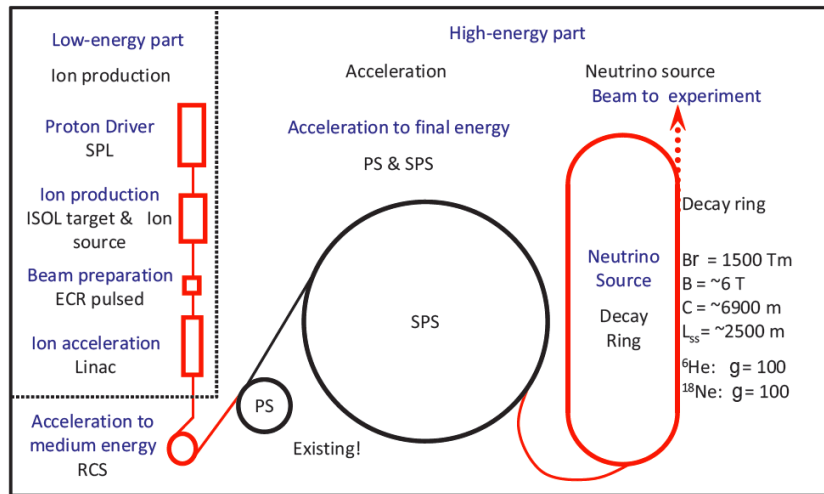


Figure 2.1: Beta-beam layout at CERN.

rigidity of 4.44 Tm and fully stripped neon ions at 2.66 Tm to an accumulation ring based on electron cooling. The aim of this machine is to accumulate the ions while the PS is ramping. This will improve the efficiency of the multi-turn injection in the next machine, by reducing the beam emittance. There are technological challenges related to the realization of the cooling ring, such as a cooling time of the same order as the repetition time of the injected pulses, and limits given by the ${}^{18}\text{Ne}$ half-life, instabilities and space-charge constraints. After the cooling ring, the relatively conventional RCS operates at 10 Hz and is designed to have reasonable radio frequency requirements ($\sim 100 \text{ kV}$). Eddy current effects require the vacuum chamber to be thin, of the order of tenths of millimeters. The RCS has a three-fold symmetry lattice, with a physical radius of 40 m, and accelerates the ions up to a magnetic rigidity of 14.7 Tm. The beams ejected by RCS enter the existing CERN PS. PS operates on its highest harmonic ($h = 21$, 10 MHz) and accumulates twenty bunches one by one from the RCS. The PS delivers both species of beam at a magnetic rigidity of 86.7 Tm in a cycle time of 3.6 s. There is no accumulation in the CERN SPS, which is less than 10% filled, but the machine was designed for fixed-target physics and its radio frequency is not ideally suited. The space charge bottleneck at SPS injection was addressed by adding an extra RF system to the existing one that allows much longer bunches to be transferred from the PS. The SPS delivers beams at $\gamma = 100$, which corresponds to a magnetic rigidity of 935 Tm for helium ions and to 559 Tm for neon. The advantageous charge-to-mass ratio of neon and fixed γ at ejection result in a cycle time of only 3.6 s compared with 6.0 s for helium. After the SPS, the beam is injected into the decay ring. The DR is a superconducting machine which has two long straight sections designed to minimize the length of the arcs, where any ion decays would be wasted. It has the same size as the SPS. The time structure of the bunches established in the PS persists to the decay ring so that the final bunch train comprises twenty bunches that occupy just one eleventh of the machine. It was proposed to stack the ions using asymmetric bunch pair merging [22], based

on a dual-harmonic RF system to combine adjacent bunches in longitudinal phase space. In this way each fresh, dense bunch is embedded in a much larger stored one with minimal emittance dilution. Longitudinal stacking means that each new bunch must be injected inside the rf bucket containing (or neighboring) an existing bunch before merging can begin. However, the requirement for very short bunches implies a bucket duration of only a few tens of nanoseconds and a single-turn injection is excluded because of the impossibly short rise time required. A multi-turn injection scheme is therefore employed. The new bunches are off-momentum and are injected in a high dispersion region on a matched dispersion trajectory. Once stacking is complete, the dual RF system can be used to shorten the bunches to improve the duty factor seen at the experimental detector.

2.4.2 Losses along the accelerator chain

Losses are present in all machines in the chain and have different origins: rf-capture, acceleration, space charge, intra-beam scattering, beam transfer and decay. Decay losses are uniformly distributed in the accelerators and they are due to the changes in the charge-to-mass ratio after the beta decay: the magnetic rigidity changes and particles are lost in the accelerator components. The demand for a high intensity beam to be stored in the decay ring results in relevant losses during accumulation and acceleration. In order to evaluate the lost power in machines the parent particle population $N(t)$ decrease can be assessed as follows:

$$\frac{d}{dt}N(t) = -\frac{\ln(2)}{t_{1/2}\gamma(t)}N(t), \quad (2.5)$$

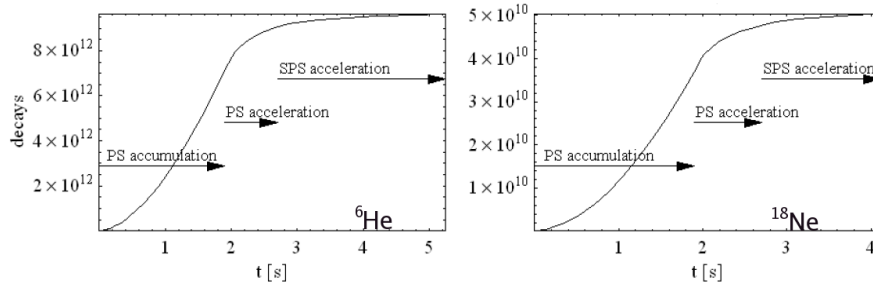
where $\gamma(t)$ is the relativistic parameter and $t_{1/2}$ is the isotope half-life at rest ($t_{1/2} = 0.81$ s for ${}^6\text{He}$ and $t_{1/2} = 1.67$ s for ${}^{18}\text{Ne}$). After the decay, the charge-to-mass ratio changes by a factor 1.5 for ${}^6\text{He}$ and 0.9 for ${}^{18}\text{Ne}$. For simplicity, it is here assumed that the kinetic energy is the only contribution to the energy lost in the machine components, as at a high γ the difference between the total and the kinetic energies is negligible. The energy lost per beam cycle is:

$$E_{\text{loss/cycle}} = \int^{t_{\text{cycle}}} \frac{dN(t)}{dt} T(t) dt. \quad (2.6)$$

T is the kinetic energy and t_{cycle} is the cycle time of the beta-beam complex. The time-average power loss per unit circumference (l) of the machine is then:

$$P_{\text{loss}l} = \frac{E_{\text{loss/cycle}}}{t_{\text{cycle}} \cdot \text{Circumference}} \quad (2.7)$$

Figures 2.2 shows ${}^6\text{He}$ and ${}^{18}\text{Ne}$ cumulative decays, based on a top-down evaluation of particle intensities, as a function of time. The top-down approach is based on the assumption of


 Figure 2.2: Cumulative ${}^6\text{He}$ and ${}^{18}\text{Ne}$ decays during acceleration.

	${}^6\text{He}$	${}^{18}\text{Ne}$	Unit
RCS injection	8.5E11	2.6E11	ions/cycle
RCS ejection	8.3E11	2.6E11	ions/cycle
PS accumulated	1.1E13	4.5E12	ions/cycle
SPS injection	9.5E12	4.3E12	ions/cycle
SPS ejection	9.0E12	4.3E12	ions/cycle
Decay Ring injection	1.8E14	8.5E13	ions/cycle
Decay Ring accumulated	9.7E13	7.4E13	ions/cycle

Table 2.3: Top-down approach beam intensities in the beta-beam facility.

nominal rates of $2.9\text{E}18$ anti-neutrinos per year from ${}^6\text{He}$ decay and $1.1\text{E}18$ neutrinos from ${}^{18}\text{Ne}$ decay per straight section. The top-down intensities are listed in Table 2.3.

Most of the decay losses, before the injection into the DR, occur in the PS, due to the long accumulation time of nearly 2 seconds. Table 2.4 summarizes the losses in all the beta-beam chain, starting from the RCS. To some extent, losses in beta beams can be compared to the

losses (ions per second)	RCS	PS	SPS	Total
${}^6\text{He}$	0.1E12	1.4E12	0.9E11	1.59E12
${}^{18}\text{Ne}$	0.2E11	3E11	0.2E11	3.3E11

Table 2.4: Summary of decay losses in all the machines.

CNGS ones. CNGS produce muon neutrinos through the decay of pions and kaons, generated by a proton beam impinging onto a graphite target. Whilst decay losses are uniformly distributed all around the several machines in beta beams, CNGS losses occur at injection and extraction locations. If we consider the PS machine, the CNGS operation leads to beam losses of $7.8\text{E}18$ protons per year. For comparison, the beta-beam operation with ${}^6\text{He}$ ions would lead to losses of $8.5\text{E}18$, i.e. 1.1 times the CNGS loss. A summary of the inter-comparison between CNGS and beta beams is given in [23] where it is concluded that the E_{lost} in a cycle is equal to 22.7 kJ for CNGS and 25 kJ maximum (${}^6\text{He}$) for beta beams, when considering only decay losses (see Table 2.5). This comparison is only partial and cannot be used as a conclusive analysis of the

		CNGS	Beta beams	
		protons	^6He	^{18}Ne
RCS	loss/cycle [primaries]	-	0.57E12	0.7E11
	$E_{loss}/\text{cycle}[\text{kJ}]$	-	0.2	0.1
	$P_{loss,average}[\text{W/m}]$	-	0.17	0.14
PS	loss/cycle [primaries]	7.6E12	8.43E12	10.7E11
	$E_{loss}/\text{cycle}[\text{kJ}]$	12.4	8	6
	$P_{loss,average}[\text{W/m}]$	3.3	2.2	2.8
SPS	loss/cycle [primaries]	3.8E12	0.53E12	0.6E11
	$E_{loss}/\text{cycle}[\text{kJ}]$	10.3	16.8	6.1
	$P_{loss,average}[\text{W/m}]$	0.25	0.4	0.25
Total	loss/cycle [primaries]	11.4E12	9.53E12	1.2E12
	$E_{loss}/\text{cycle}[\text{kJ}]$	22.7	25	12.2

Table 2.5: Comparison between CNGS total losses and beta-beam decay losses.

impact of beta beams at CERN in terms of losses: first of all, other sources of losses in beta beams are not included in the comparison, like collimation and acceleration; furthermore, from a radiation protection point view, the intensity of the losses is only one of the factors to consider in the radiological-risk assessment. Some other important parameters are the energy of the beam, the points in the machine where the losses occur, the material composition of the machine components and the location of the facility.

2.5 Conclusion of the feasibility study

The feasibility study is now concluded and all the results are published [24]. The study focuses on the accelerator chain, which incorporates some of the existing CERN machines, but more attention is paid to the non-existing machines, the RCS and the DR. Some novel techniques are proposed, like the off-momentum injection in the DR and the RF gymnastics to accumulate ions in longitudinal phase space with minimal emittance dilution. Studies of momentum collimation in the DR, of beam loss, of dynamic vacuum and of radiation protection issues throughout the accelerator chain have been performed. The main conclusions for each working group are here summarized.

Concerning production, ^6He is believed to be an appropriate primary ion as the required production rate could be achieved by impinging 1 GeV protons on a BeO target. Tests performed at the CERN ISOLDE facility have confirmed the efficiency of this production method. The production of ^{18}Ne is still problematic, as the achieved production rate is of two orders of magnitude lower than the required one. Several production methods have been investigated and also alternative ions have been considered, like ^8B and ^8Li . The EUROnu Design study [25] is evaluating the latter option. The ECR prototype source for the ionization and bunching of the ions, designed within the EURISOL Design Study, has been built and commissioned

2.5. Conclusion of the feasibility study

at LCNMI Grenoble within the EUROnu Design Study framework. During the design study it has been understood that the EURISOL SPL would not be suited to the acceleration of the beta-beam ions and a normal-conducting LINAC has been designed by IAP Frankfurt. Indeed the low duty cycle and the high-pulse beam current makes normal-conducting cavities preferable to super-conducting ones. The accumulation ring, which is a non-baseline option, aimed at performing electron cooling between the LINAC and the RCS, seems to be feasible for ^{18}Ne , but it would be problematic for ^6He , due to the longer time needed for the transverse emittance cooling. The study of the RCS design is completed and the main characteristics of this machine are presented in Chapter 4. Beam dynamics studies have proven that in a fast ramping machine like the RCS, eddy currents in the metallic vacuum pipe can introduce field components that modify the natural chromaticity of the ring. The associated effects have been evaluated together with the possible countermeasures. The main conclusion is that the RCS can be built with the known technology. The study has also demonstrated the possibility of exploiting the existing PS and SPS machines, by evaluating their RF and vacuum systems performances within beta beams, and concluding that the two accelerators can be used. The DR design is also completed. With the stacking mechanism the throughput of the facility is optimized. The stacking eventually induces a blow-up of longitudinal phase space which can be limited by the momentum collimation. The main ion losses within the ring are therefore due to collimation, and secondarily to radioactive decays. The energy depositions resulting from both loss mechanisms have driven the design of open mid-plane magnets. Even if some technical issues are still under evaluation, the design study has proven the feasibility of the beta beams within a CERN baseline. At the end of the feasibility study two aspects have been regarded as issues: the ion production efficiency and the radiation protection. The former remains an open problem and methods for the improvement of the ion production rates have been investigated within other tasks of the EURISOL design study. The study of the radiological risks associated with the RCS, PS and DR operations within beta beams is the object of this work.

3 Theoretical framework

3.1 Radiation protection at ion accelerators: nuclear reactions and theoretical models

In general, the interaction of particle beams with accelerators generates both prompt radiation, which is the radiation emitted while the accelerator is operated, and induced radioactivity, which persists also when the accelerator is not operated. Both types of radiation have to be evaluated in a radiation protection study which aims at predicting safety measures for the operation and the maintenance of the accelerator. When particles are lost and interact with matter, several secondary particles can be produced through a number of mechanisms, which depend on the energy and type of the projectiles and on the target material. Charged particles, like electrons and photons, can produce photoelectric effect, pair production and Compton reactions, from which other electrons and photons are generated. The latter can in their turn start new reactions and produce an electromagnetic shower. If the reaction involves particles with an energy above few tens of MeV, nuclear interactions generate hadronic showers. The hadronic shower can in turn trigger electromagnetic showers: above the threshold for the production of pions, 290 MeV, an increasing fraction of energy is transferred from the hadronic to the electromagnetic component due to the production of mesons that decay into electrons, positrons and γ . In order to predict the products of the nuclear reactions, several models have been developed. Among the commonly used ones, one can mention those of interest for the nuclear reactions occurring in the energy range of beta beams: intranuclear cascade model [26], Glauber cascade [27], pre-equilibrium [28], evaporation [29], Fermi break-up [30], fission [31] and nuclear fragmentation [32]. These models describe nuclear reactions stages and are usually applied in different energy ranges. For instance, the intranuclear cascade model applies to reactions occurring above 200 MeV. Below this energy the pre-equilibrium model is used to describe the state at which excited nucleons move inside the nucleus before it achieves an equilibrium state. In the evaporation stage, nucleons and light fragments (only for energies higher than the Coulombian wall) can be ejected. Light nuclei with atomic mass A comprised between 16 and 70 can be well described by the evaporation model, while those with $A < 16$ usually undergo Fermi break-up reactions, and heavy nuclei, with $A > 100$, are

subject to nuclear fragmentation. The intranuclear cascade model can be used also for light nuclei with relatively high energies, but the description of reactions at low energies is limited by the lack of experimental data.

The beta beams will use the radioactive ions ${}^6\text{He}$ and ${}^{18}\text{Ne}$ as primary beam. The energy range of beta beams is quite wide and, besides primary radioactive ions, also their decay products largely contribute to the total amount of losses in machine components. The energy range considered in this study goes from 100 MeV per nucleon to 92 GeV per nucleon. In this scenario, many nuclear reactions occur including elastic and inelastic scattering processes, with γ radiation emission in the latter and knockout reactions, with the ejection of a nucleon. Compound-nucleus mechanisms are also possible. The kind of process occurring in ion reactions depends also on the impact parameter b (see Figure 3.1), which characterizes the distance between the projectile and the target. At large b , Coulomb effects are dominating,

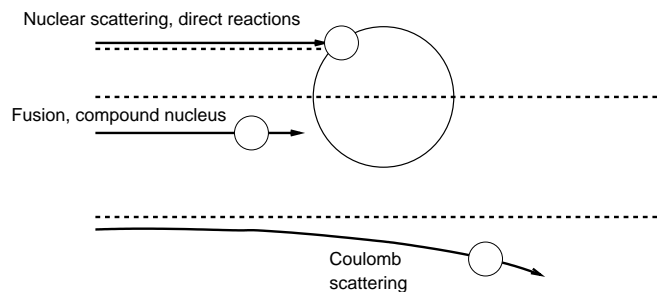


Figure 3.1: Possible heavy-ion interaction processes, depending on the impact parameter b [68].

giving Rutherford scattering and Coulomb excitation. At small b and for small overlapping of the nuclei, usually inelastic scattering and nucleon transfer in direct reactions may occur. For very small impact parameters and if the nuclei completely overlap, a compound nucleus can form, if the excitation energy is high enough to overcome the Coulomb barrier. The compound states and their decay modes towards stability are a challenging subject of study, for many decay channels are possible. Emission of neutrons is usually the preferred decay mode, even if the compound nucleus is extremely proton rich. In general the models employed for the nuclear reactions of ions as projectiles are the Boltzmann Master Equation theory (BME) [33], the Relativistic Quantum Molecular Dynamics model (RQMD) [34] and the Dual Parton Model (DPM) [35]. In the next sections particular relevance is given to the BME theory embedded into the Monte Carlo (MC) code FLUKtuierende KAskade (FLUKA).

3.2 General features of the Monte Carlo code FLUKA

Only few Monte Carlo codes can transport ions and treat the associated reaction mechanisms satisfactorily. FLUKA [36, 37], Mars [38], Phits [39], just to mention some, are often used in radiation protection studies, as their physics model have been validated with experimental data

3.2. General features of the Monte Carlo code FLUKA

collected in campaigns of measurements at several accelerator facilities. A lot of efforts have been made in the last few years in order to collect experimental data also on nucleus-nucleus interactions and to upgrade the databases used by the above-mentioned MC codes. FLUKA is chosen for all MC calculations in this work. An exhaustive description of its capabilities is beyond the scope of this study and can be found in the literature [36, 37]. In this section, only the aspects relevant for the current work are outlined.

FLUKA is a general-purpose Monte Carlo code, describing particle transport and interactions with matter. It was first conceived to simulate hadron cascades at high-energy proton accelerators for shielding design but, year after year, it has evolved into a multipurpose code applied to accelerator shielding (hadrons and leptons), target design, activation, calorimetry, detector design, dosimetry, radiobiology, radiotherapy, space physics, neutrino physics and, recently, radiation damage to electronics. FLUKA can transport around 60 particles and heavy ions, dealing with hadron-hadron and hadron-nucleus interactions from threshold up to 10000 TeV and with electromagnetic interactions from 1 keV up to 10000 TeV. The combinatorial geometry allows the users to describe very complex geometries and to implement electromagnetic fields. Transport of neutrons with energies lower than 20 MeV down to thermal ones is performed in a multigroup approach, with 72 or 260 groups [40]. FLUKA uses its own neutron cross section libraries, containing more than 200 different materials, selected for their interest in physics, dosimetry and accelerator engineering and derived from the most recently evaluated data (ENDF-B VI, JENDL and JEFF [41]). Nucleus-nucleus interactions are reproduced up to 10000 TeV per nucleon with different models corresponding to three energy intervals: BME, RQMD and DPMJET. Figure 3.2 summarizes the program flow for heavy ions, showing the energy thresholds of the three nucleus-nucleus collision models. From 100 MeV per nucleon up to 5 GeV per nucleon the code is interfaced to a modified version of the RQMD-2.4 [42]: the original version successfully describes nucleus-nucleus interactions but is not able to identify nucleon clusters in the final state and therefore their de-excitation mechanisms, limiting the high-energy component of observed spectra at forward angles. In the modified version of RQMD-2.4, projectile- and target-like residues are identified through the other nucleons and the energy balance is possible by taking into account the experimental binding energy of nuclei. The final de-excitation of the fragment is then evaluated by the FLUKA evaporation-fission-fragmentation module. From 5 GeV per nucleon up to 10000 TeV per nucleon the DPMJET-III [43] is used. It is based on the Dual Parton Model and the Glauber formalism. Below 100 MeV per nucleon down to the Coulomb barrier, the BME is used. 100 MeV per nucleon, besides being the threshold energy between the BME and RQMD models, represents the injection energy of the RCS in the beta-beam facility. When the radioactive ion beams interact with the machine components, several reactions occur which involve nucleus-nucleus mechanisms well below 100 MeV per nucleon. This is valid also for higher energies, namely the ones of the other machines in the acceleration chain. As this model is still under development in FLUKA, it has been tested and compared with experimental data (Section 2.4). In the next section, a brief description of the BME model within the FLUKA code is given.

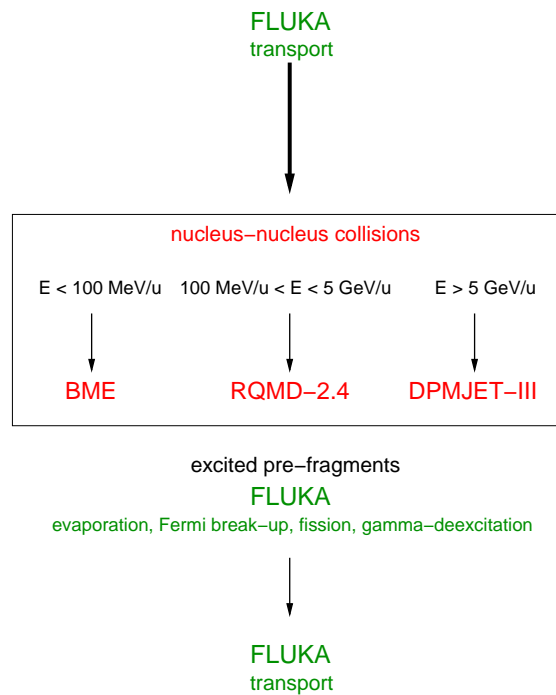


Figure 3.2: The FLUKA program flow for heavy ions [44].

3.3 The Boltzmann Master Equation theory

In the mid sixties, given the experimental evidence of nuclear reactions with a character in between direct and compound-nucleus processes, two phenomenological models, the exciton model by Griffin [45] and the BME theory by Harp, Miller and Berne [33, 46], were proposed to describe the emission of particles by the composite nucleus formed in the interaction of a projectile and a target. Both the models predict the emission of particles during the interaction that brings the unequally distributed initial excitation energy into the statistically distributed thermal energy.

As already mention in Section 1.1, when an ion interacts with a target many different reaction mechanisms can occur. The non-equilibrated nuclei undergo several processes, like the emission of fast particles, in the process that leads to the thermal equilibration (“thermalization”). Once the nuclei are equilibrated they can evaporate particles and γ rays leaving a residue, which, in its turn, may further radiate β , α and γ rays. The BME theory evaluates the variation with time of the distribution of the momenta of the nucleons of an excited nucleus by describing the mutual interactions of the nucleons and their emission into the continuum as separate entities or as a part of a cluster, without assuming the equiprobability of the states for a given configuration. This implies that the BME can be used in the case of asymmetric heavy ion reactions, where other models that assume the equiprobability would fail. In the BME theory, the initial state can be represented with the complete fusion state of the nuclei, after which they can have evaporation with emission of fast particles or pre-equilibrium. If the

latter happens, high-energy particles can trigger peripheral reactions and again evaporation of the residues can occur. The peripheral reactions can also represent an initial state and can be classified target-like, projectile-like or produce intermediate-mass fragments (IMFs). In the last two cases both evaporation and Fermi break up reactions can happen, depending on the mass of the nuclei. All these possible processes lead to the formation of a residual nucleus that can then be described with the evaporation model. Within the theoretical framework of the BME, a large set of experimental data including light particles, IMFs and excitation functions of the evaporation residuals has already been reproduced and can be found in the literature [47, 48]. Reactions which involve heavy targets at the BME energies are still under development. The BME theory is used in the FLUKA code through a database. Several systems of ion pairs (projectile and target) at several energies are treated with the mechanisms within the BME theory and their double differential spectra and ejectile multiplicities are fitted by means of analytical expressions. This is an off-line procedure and the parameters of the fit are stored in the database, which is then used in the on-line calculations to simulate the thermalization process. In this way, the simulations can be reasonably fast. If the full BME formalism was implemented in FLUKA, for reactions occurring in heavy targets, the calculations would become extremely time consuming. As described in [47], in FLUKA, for any pair of ions, the reaction cross section is calculated and subdivided into complete fusion with probability p_{CF} and peripheral collision with probability $p_P = 1 - p_{CF}$. For the peripheral collisions the impact parameter is chosen randomly by the differential cross-section $d\sigma/db$. For small impact parameters the model predicts the complete fusion (CF) of the nuclei, for increasing b it predicts a 3-body system (3B), with the formation of a cold project-like and a target-like nuclei and an excited middle system, for high b the interaction is the inelastic scattering (INEL-SC). Once the type of process is determined with the BME theory, the FLUKA module of evaporation-fission-fragmentation, like for the RQMD, is used.

3.4 Comparison with experimental data

This section describes the comparison test between FLUKA simulations and the results of two experiments with ions, performed respectively in Japan, at HIMAC, and in South Africa, at IThemba Labs, are presented. In the experiment at HIMAC data on double differential spectra of neutrons produced in the interactions of heavy ions with several targets were collected. These data have also been benchmarked with the code PHITS [49] and the results show a fine agreement between simulated and measured values. In order to prove the reliability of FLUKA in predicting the same quantities, the same data are compared to FLUKA simulations. In the experiment at IThemba Labs, the double differential spectra of secondary ions produced in the interaction of ^{16}O ions with an initial energy of 14.7 MeV per nucleon on a ^{12}C target were measured. The scope of this study is mainly to show the state of the art of the nuclear model, which is still under development, including its limits in estimating the production of fragments.

3.4.1 $^{20}\text{Ne}+^{63}\text{Cu}$ at 100 MeV/u

The secondary neutrons produced by ion beams interacting with accelerator components are of major importance in the estimation of radiation source terms in shielding calculations and of induced activity in the air and in the machine components. In order to assess the shield requirements and the yields of produced radionuclides for the low- and intermediate-energy injector of the beta beams facility, the RCS, which has an injection energy of 100 MeV per nucleon, the FLUKA-BME model must be used. It is of interest to test its capability of reproducing the energy and angle distributions of secondary particles, in particular of neutrons. At higher energies the models have already been extensively validated [50, 51]. At 100 MeV per nucleon, the results of experiments on thick targets bombarded by ^{20}Ne ions, performed at the HIMAC facility [49], are compared with those obtained in FLUKA simulations and are here presented.

3.4.1.1 Experimental set-up

The experiments were performed at the heavy-ion synchrotron, using the time-of-flight (TOF) method for the energy measure. The experimental arrangement is shown in Figure 3.3. The

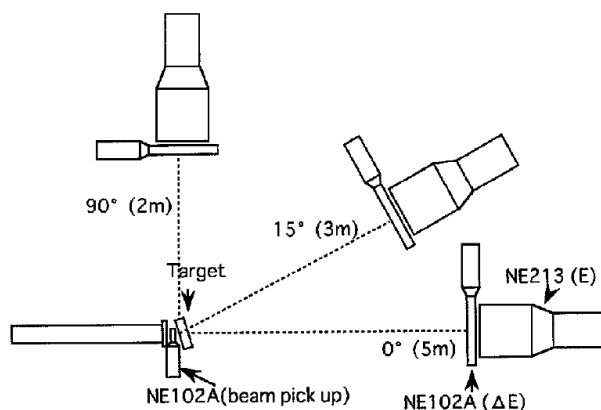


Figure 3.3: The experimental set-up at HIMAC [49].

beam, before hitting the target, was intercepted by a pick-up scintillator, used as the start signal of the TOF and as a counter of the absolute number of projectiles incident on the target. The beam-spot diameter was 1.5 cm on the target and the beam height was 1.25 m from the floor. Several measurements with different targets were performed but in this work only those with the copper target are considered. The copper target had a thickness of 0.5 cm. The detection angles ranged from 0° to 90° and for large angles the target was set at 45° with respect to the beam axis to minimize the attenuation of neutrons in the target. The target was squared with a 10 cm side and with a density of 8.93 g cm^{-3} . For each measured angle there were a liquid scintillator (NE213) coupled to a photomultiplier for the measurement of the energy E and

a plastic scintillator (NE102A) coupled to a photomultiplier for the ΔE measurement. The latter was placed in front of the former in order to discriminate charged from non-charged particles. The ΔE counter indeed does not scintillate when neutrons and γ rays hit it. The distance of the detectors from the target depended on the angle of measurement, ranging from 2 m (for large angles) to 5 m (for small angles) to give better resolution in the detection of high-energy neutrons in the forward directions. In order to minimize the backscattered neutron component no shielding was placed near the detectors. The energy resolution in the collected experimental spectra was evaluated and the statistical uncertainties were estimated to be of the order of 5% for the low- medium- energy region (5-50 MeV) and about 30% for the highest energies.

3.4.1.2 Simulations and results

In the simulations the detectors are represented by cylinders of the same dimensions and all the experimental set-up is described with precisely the same material and dimensions. Also the inclination of 45° of the target is implemented in the geometry. The BME model is activated and only the hadron cascades are detected, while the electromagnetic component is not considered, as it would not contribute to the neutron production and yet increase the CPU time for the simulations. The lethargic spectra for neutrons, i.e. the neutron fluence spectra per unit logarithmic energy, are calculated at several angles. The results of the comparison are presented in Figures 3.4 and 3.5, for the detection angles of 15° , 30° , 60° and 90° . Both experimental and calculated spectra show broad peaks at high energy for forward directions, given by the break-up neutrons: the peak is at nearly 70 MeV. Below 10 MeV, the spectra are constituted by neutrons emitted during the equilibrium process. The component above 10 MeV is given by neutrons produced in the pre-equilibrium stage. For large emission angles the spectra become softer, as the pre-equilibrium process is peaked for forward directions.

The simulation results show a fine agreement with the experimental spectra at small angles, for 15° and 30° , both in energy and in intensity. At 30° the high-energy component of the spectrum is softer in the simulated results than in the experimental data. At 60° , the experimental spectrum ends at nearly 100 MeV, whilst the calculated one has a higher-energy endpoint. Nevertheless, the lower energy component is well simulated. The same behavior at low energies is observed in the 90° case, where the endpoint energy is properly reproduced. There is though a difference in the soft part of the two spectra, which can be accounted for a ratio of nearly 4 (worst case).

This comparison shows that FLUKA can well reproduce the double differential spectra for neutrons, for all angles at which a shielding might be needed, i.e. large angles. The extra component at high-energy which is not present in the experimental data - and that could be due to a energy threshold in the detectors - results in a conservative evaluation of the number of neutrons which translates into a conservative approach in the assessment of the radiological risks.

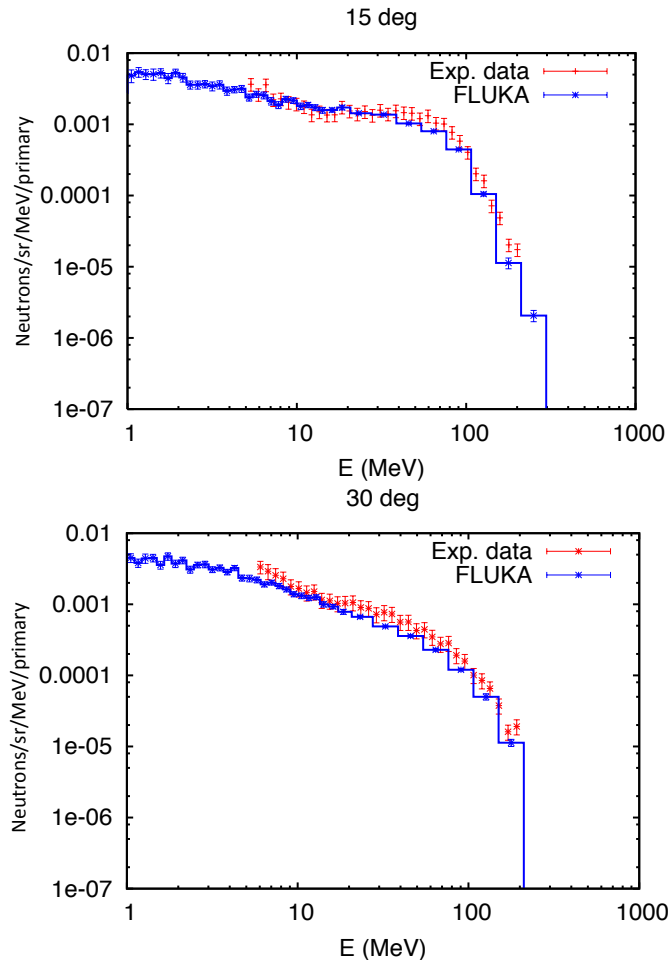


Figure 3.4: Double differential neutron spectra at 15° (top) and 30° (bottom).

3.4.2 $^{16}\text{O}+^{12}\text{C}$ at 14.7 MeV/u

At the end of 2009, within the collaboration between the nuclear physics group of the Department of Physics of the University Statale of Milan (Italy) and the nuclear physics group of the IThemba Labs in Cape Town (South Africa), an experiment was performed at the IThemba Labs which contributed also to the development of the nuclear model BME in the MC code FLUKA. This experiment gave insight on the current capabilities of FLUKA for the transport and interactions of low-energy ions. The choice of this code, even with its limits in the low-energy nucleus-nucleus model, was based on a research on comparative results between experiments and other available codes. Many benchmark measurements for BME have been conducted in the last few years and the results can be found in the literature [47, 52]. Several ion-pair systems have been considered for energies starting from the Coulomb barrier up to several tens of MeV, for instance $^{20}\text{Ne}+^{165}\text{Ho}$ at 11-30 MeV per nucleon and $^{12}\text{C}+^{12}\text{C}$ at 200 MeV per nucleon, just to mention some. In the data in the literature, both neutron spectra and secondary fragments production rates at several angles are presented with a good agreement

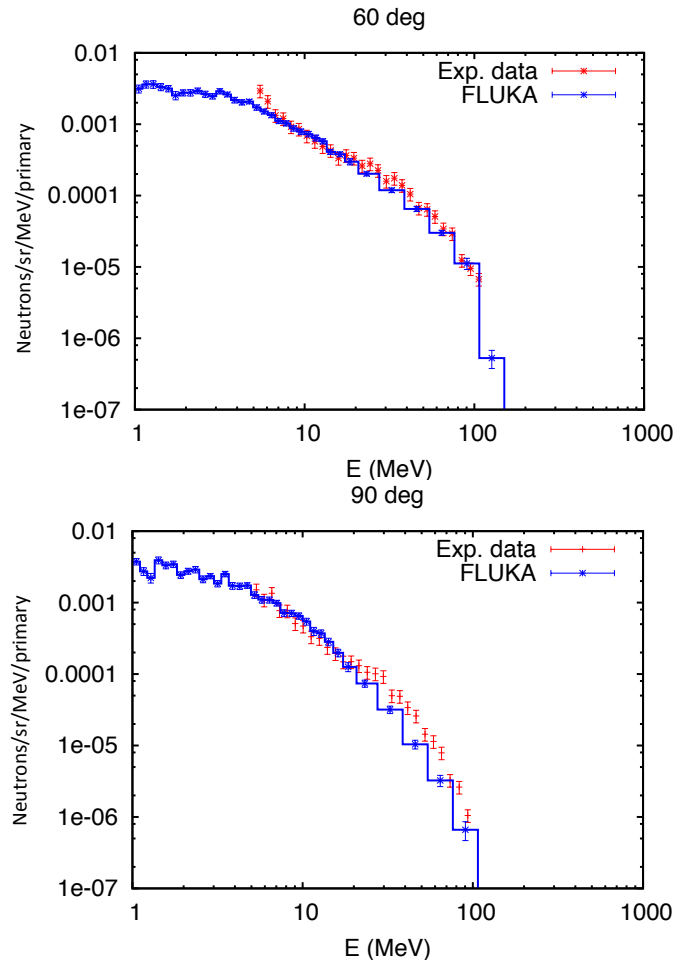


Figure 3.5: Double differential neutron spectra at 60° (top) and 90° (bottom).

between the theory and the experimental data.

3.4.2.1 Experimental set-up

The experiment was performed in the scattering chamber with a diameter of 1.5 m, shown in Figure 3.6 (left). The chamber was equipped with two rotatable arms on which several detectors were mounted. In the center of the chamber there was an aluminum target ladder, which could hold five different targets positioned perpendicular to the beam (Figure 3.6, right). The target angle could also be changed by rotating the target ladder and this resulted in a change of the thickness of the target itself. The detector arms and the target ladder could be controlled from remote. The alignment of the beam spot on the target was performed by using a video-camera and a scintillating ruby target with a hole of 3 mm. On the ladder, permanent magnets were used to deflect electrons so that they could not reach the detectors. The vacuum achieved inside the scattering camera was in the order of 10^{-5} mbar.

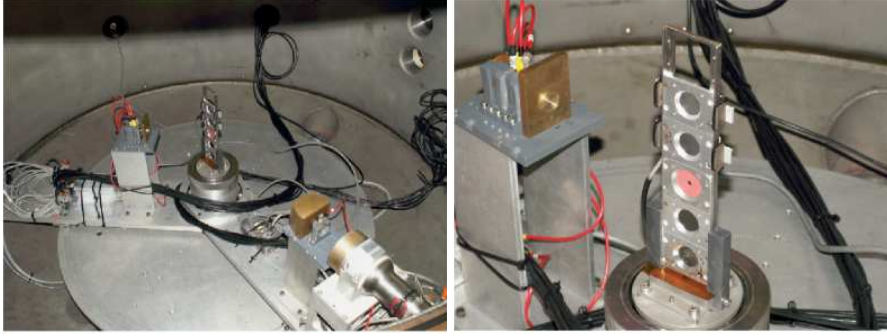


Figure 3.6: Left: scattering chamber with the two rotatable arms. Right: target frame.

A ^{16}O beam, produced by an ECR ion source and accelerated by a cyclotron, was delivered on the ^{12}C target at an energy of 14.7 MeV per nucleon, for a total energy of 235.2 MeV. The target was a ^{12}C plate with a thickness of $220\ \mu\text{g}/\text{cm}^2$, mounted on the aluminum frame, with a diameter aperture of 25 mm. The target frame contained also an empty slot, used to monitor the unwanted events caused by the beam halo. The electronics dead time was kept at the maximum value of 5% by limiting the beam intensities. A detector telescope was mounted on each arm to measure angular distributions of the continuum energy spectra of fragments and evaporation residues produced during the bombardment. One arm called Telescope 1 (T1) was used to measure the Projectile Like Fragments (PLF) from boron to neon isotopes produced in the interaction of ^{16}O and ^{12}C . This arm consisted of a $57\ \mu\text{m}$ -thick silicon ΔE_1 Silicon Surface Barrier (SSB) (T1A) detector, a 1.017 mm-thick ΔE_2 SSB (T1B) detector followed by a 1.017 mm-thick E SSB (T1C) stopping detector. More precisely, T1A was used for IMFs with $Z \geq 5$, T1B was used as a transmission detector for IMFs with $Z \geq 5$, and T1C was used as a stopping detector for IMFs with $Z \geq 5$. Several collimators were employed to avoid radiation damage to the detectors: a 10-mm thick brass collimator block was used to shield the Si telescope; a 8 mm-thick brass collimator insert with an opening of 6 mm diameter was fitted to the collimator block. The solid angle subtended by T1 was 0.9081 ± 0.018 msr. The other arm Telescope 2 (T2) was used to measure the lighter IMFs ($3 \leq Z \leq 4$) and consisted of a $93\ \mu\text{m}$ -thick ΔE SSB detector (T2A), followed by a 3"-diameter and 2.5"-in length E crystal NaI stopping detector (T2B). The NaI was used due to its high stopping power in order to stop all the lighter particles. A 50 mm-thick brass collimator block was used to shield detector telescope T2. A 53 mm-thick brass collimator insert with an opening of 17.1 mm in diameter was fitted to the collimator block. The solid angle subtended by T2 was 1.475 ± 0.024 msr.

The $\Delta E - E$ technique was used for particle identification and for mass separation of the isotopes. The uncertainties in the measurements were estimated to give an error on the data points of 3%. All the experimental data collected in the same campaign are described in the work in progress of J.P. Mira [48]. Figures 3.7 and 3.8 show the Particle Identification Spectra (PID) for the heavy fragments, realized with the particles between T1A and T1B detectors and with particles between the T2A and T2B detectors, respectively [48]. In Figures 3.9 and

3.4. Comparison with experimental data

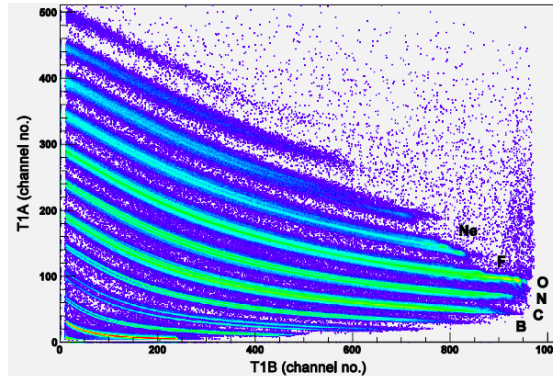


Figure 3.7: Typical 2D PID spectra for heavy IMFs with $Z \geq 5$, between T1A and T1B detectors [48].

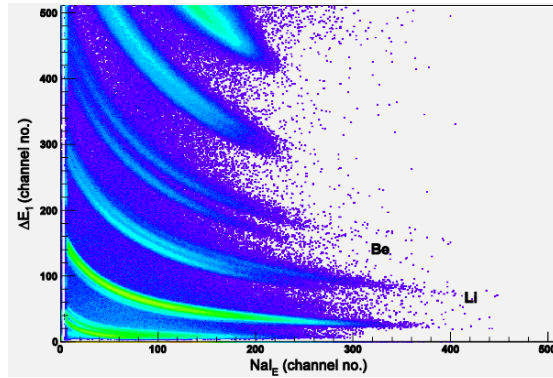


Figure 3.8: Typical 2D PID spectra for IMF with $3 \leq Z \leq 4$ between T2A and T2B [48].

3.10, the Mass Function (M_F) spectra for the isotopes of oxygen and fluorine respectively, are presented. The mass identification is done by using the following expression:

$$M_F = [(E_B + E_A)^P - (E_B)^P] \cdot M_S + M_O, \quad (3.1)$$

where E_B , E_A is the energy deposited in detector B and A, respectively. P is a constant used to optimize the mass-function loci, M_S is a slope factor and M_O is an offset. Both are chosen to get the best characteristics of the mass function spectra.

3.4.2.2 Simulations and results

The nuclear reaction is reproduced with FLUKA-BME: the primary beam hits a thin target, of the same dimensions and characteristics of the real one. The double differential spectra for the fragments produced in the reaction for several angles are calculated. Only the fragments of interest are detected and the other particles are ignored. In the reaction $^{16}\text{O}+^{12}\text{C}$ the produced

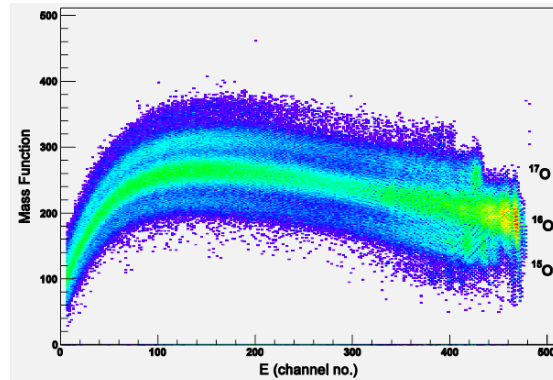


Figure 3.9: Mass function spectra extracted between T1A and T1B with the gates around the loci of O. These gates were used to calculate the double differential spectra of the respective isotope [48].

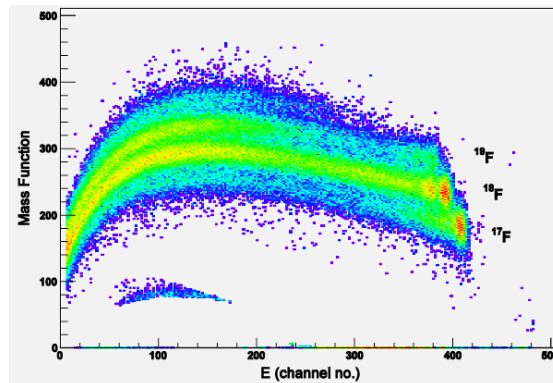


Figure 3.10: Mass function spectra extracted between T1A and T1B with the gates around the loci of F. These gates were used to calculate the double differential spectra of the respective isotope [48].

fragments can be subdivided in high- A fragments, with $A > 16$, and low- A fragments, which have a $A < 16$. Here only results for the O and F are presented. The high- A fragments and high charge such as the fluorine and heavy oxygen isotopes are mainly produced by a mechanism of complete fusion and by the subsequent emission of light particles both in pre-equilibrium and in the evaporation stage, leaving them as residues. Figures 3.11, 3.12 and 3.13 shows the double differential spectra for the fragments of ^{17}F at 10° , 12° and 15° and figures 3.14, 3.15 and 3.16 represent the double differential spectra for the fragments of ^{17}O at 10° , 12° and 15° . These fragments are heavier than the projectile. The total double differential spectra (black line) predicted by the theory are compared to the experimental values (red dots). Also the contribution of the three mechanisms CF, 3B and INEL-SC are shown. These data show an experimental low-energy threshold around a total energy of 80 MeV. In the theoretical curves two different contributions can be clearly identified: a narrow high-energy peak, which is fully

compatible with the experimental findings, and a broader low-energy peak, consistently lower for the fluorine spectra. The former is given by neutron-proton pickup reactions, significantly decreasing for increasing angle, the latter is obtained via the complete fusion mechanism with the composite nucleus de-excitation. From the comparison, it is clear that the theoretical model is missing the intermediate energy-range, which corresponds to the 3B reaction process.

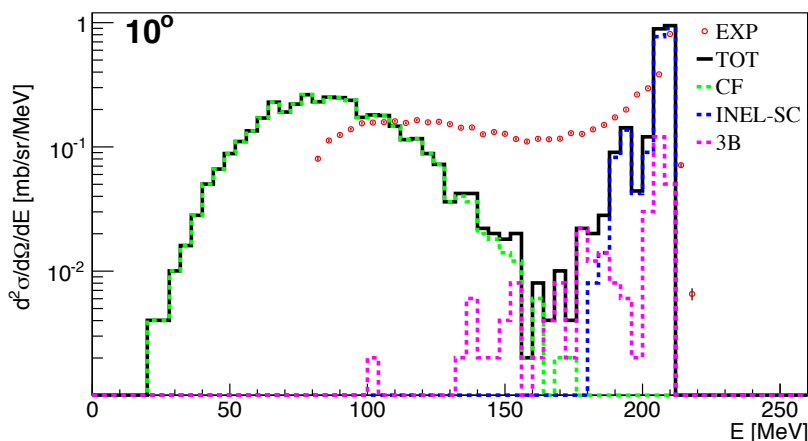


Figure 3.11: Double differential spectra of ^{17}F at 10° . Comparison between experimental data and theoretical prediction. The three components of the theoretical curve are fragments produced in complete fusion, inelastic scattering and in 3-body mechanism with incomplete fusion.

Available experimental data also include lighter fragments like nitrogen and carbon, but the model lacks the specific mechanisms at the data points, like, for instance, the two-nucleon stripping: this is expected to account significantly for the high-energy side of the spectrum.

3.4.3 Conclusions

Secondary ion fragments play an important role in energy deposition processes and their production should be predicted correctly in order to have a correct estimate of the energy distribution. At the same time, it was demonstrated that, while the projectiles are fragmented into radioactive fragments that remain inside the target, secondary particles dominate the activation process in the long interaction range [53]. This can be explained by the fact that the Coulomb interaction with the target electrons stops the ions, i.e. the ions have a Coulomb stopping range shorter than their mean-free path for nuclear interactions. All stages in the life cycle of a high energy accelerator require calculations of induced radioactivity, as the results enter the design of components and the choice of materials as well as environmental impact studies. During operation they provide dose estimates for work on activated components

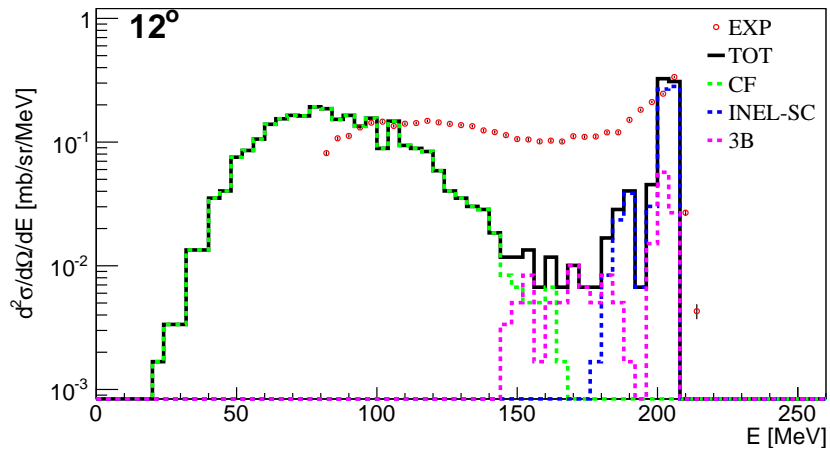


Figure 3.12: Double differential spectra of ^{17}F at 12° . Comparison between experimental data and theoretical prediction. The three components of the theoretical curve are fragments produced in complete fusion, inelastic scattering and in 3-body mechanism with incomplete fusion.

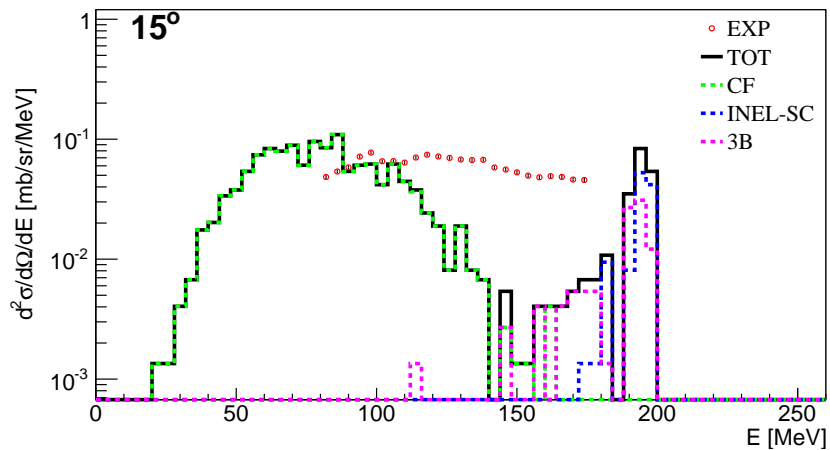


Figure 3.13: Double differential spectra of ^{17}F at 15° . Comparison between experimental data and theoretical prediction. The three components of the theoretical curve are fragments produced in complete fusion, inelastic scattering and in 3-body mechanism with incomplete fusion.

and in the proximity of the machine. The decommissioning of an accelerator is based on studies of the nuclide inventory. MC models used for induced-activity calculations must be able to reliably predict nuclide production at energies ranging from that of thermal neutrons up to several TeV. In particular, the emission by the excited nuclei of neutrons, which are the main protagonist of the induced activity reactions, is of utmost importance. Because the code

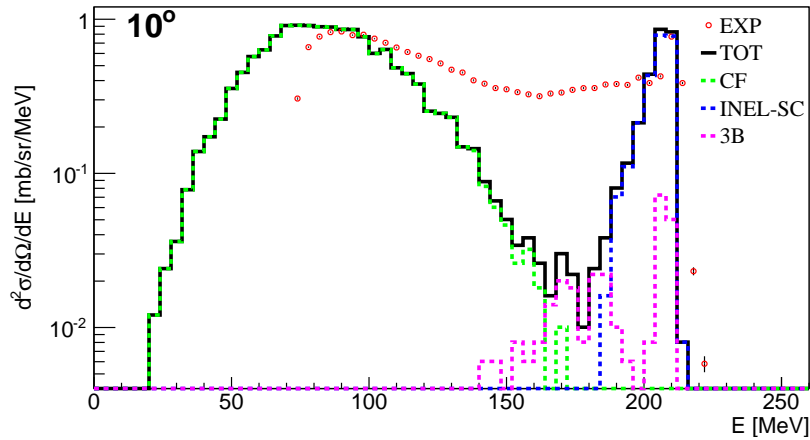


Figure 3.14: Double differential spectra of ^{17}O at 10° . Comparison between experimental data and theoretical prediction. The three components of the theoretical curve are fragments produced in complete fusion, inelastic scattering and in 3-body mechanism with incomplete fusion.

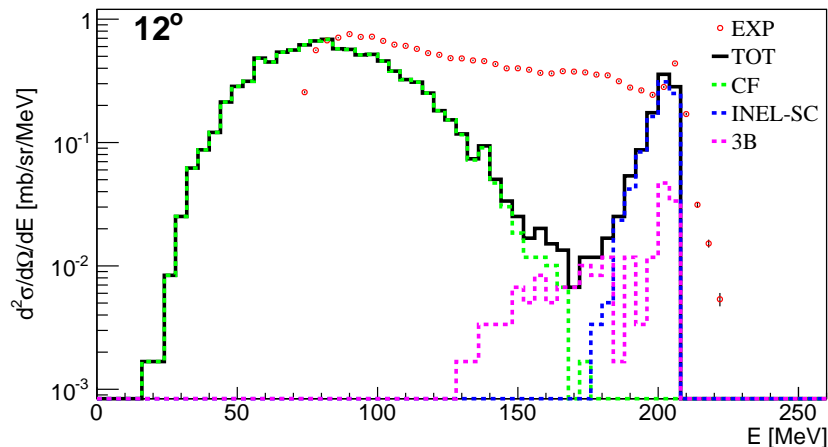


Figure 3.15: Double differential spectra of ^{17}O at 12° . Comparison between experimental data and theoretical prediction. The three components of the theoretical curve are fragments produced in complete fusion, inelastic scattering and in 3-body mechanism with incomplete fusion.

reproduces in a fine way the neutron spectra for primary ^{20}Ne ions on a copper target at 100 MeV per nucleon, it can be concluded that imperfections of the current theoretical model for ions does not have a significant impact on the estimates of quantities for radiation protection because the high-energy secondary hadrons are well predicted by the code. At the same time, the measurements performed in the frame of this thesis suggest that a further development of

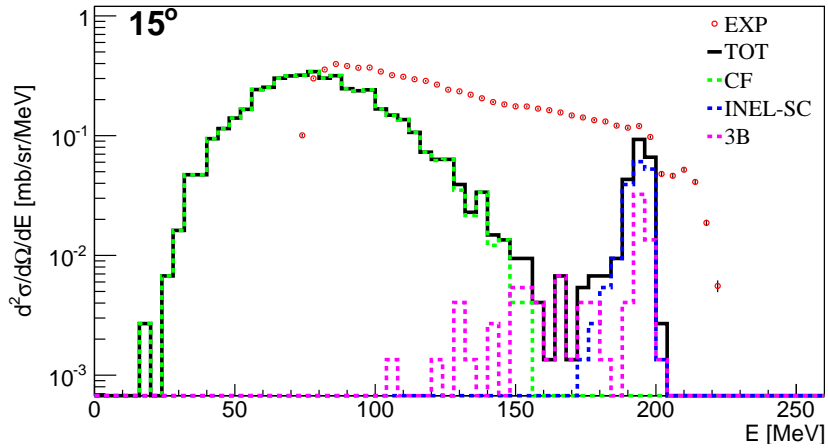


Figure 3.16: Double differential spectra of ^{17}O at 15° . Comparison between experimental data and theoretical prediction. The three components of the theoretical curve are fragments produced in complete fusion, inelastic scattering and in 3-body mechanism with incomplete fusion.

the BME is needed for studies which concern energy distribution of energy deposition.

3.5 Comparison between protons and ions

Given the lack of experimental data on nuclear reactions with heavy ions, especially in the low-intermediate energy range, the behavior of protons and heavy ions was analyzed in order to assess analogies and discrepancies in the production of secondary particles. While the analogy is more obvious at high energy, where the nucleons in the ion behave as almost free nucleons, the analogy at low-intermediate energy is less immediate, given the strong intra-nuclear effects that the nucleons undergo. In order to investigate such analogy at an energy of 100 MeV per nucleon, the secondary neutron fluence spectra produced by proton and ion beams hitting a target are calculated with MC simulations. The geometry used is a simplified representation of an accelerator component (magnet or RF cavity): the beam impinges onto a small copper target placed inside a stainless steel cylinder (2 mm thick, like in a standard beam pipe), surrounded by an iron cylinder, that could be imagined to represent a magnet yoke (Figure 3.17). The double differential fluence spectra are calculated at the surface separating the beam pipe from the iron cylinder and at the surface separating the iron cylinder from the air in the tunnel. Results at 100 MeV per nucleon are shown in Figure 3.18 for helium ions and protons and in Figure 3.19 for neon ions and protons. The spectra for the neutrons produced by primary protons are normalized to the number of nucleons of the primary ion used in the correspondent comparison. The main difference between the two normalized spectra, in both comparative cases, is the high energy end-point. Indeed the ions always produce neutrons with a higher energy, which is clearly due to the higher mass number, whilst protons produce

3.5. Comparison between protons and ions

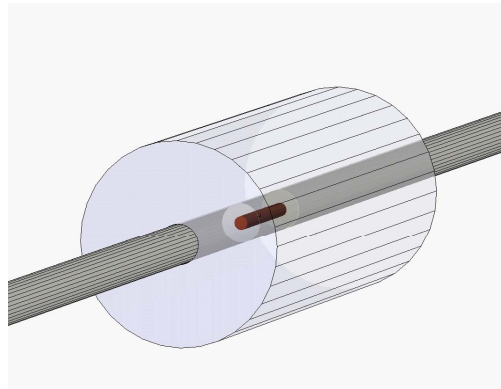


Figure 3.17: Representation of a beam line element, i.e. a magnet yoke around a beam pipe.

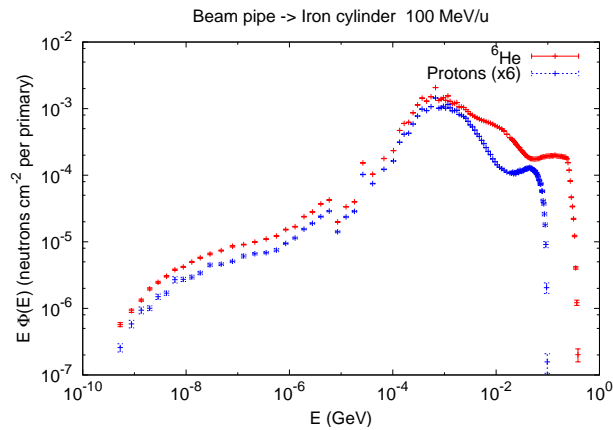


Figure 3.18: Neutron fluence at 100 MeV per nucleon at the boundary between the beam pipe and the magnet yoke. Comparison between ${}^6\text{He}$ ions and protons (intensity normalized to the ${}^6\text{He}$ intensity).

neutrons with a top energy of 100 MeV. This corresponds to the elastic recoil with protons. In the helium case, the nucleon-neutron recoil peak is also present, but another noticeable shoulder in the spectra is present from an energy of nearly 10 MeV to 100 MeV. In the neon case, the elastic peak is missing at the end-point energy and the spectra in the high-energy region is softer than the proton one. This could be due to high number of nucleons which would then interact with the material giving more evaporation neutrons in the low-energy range. Given the different shapes of the fluence spectra for neutrons produced by primary protons and those produce by primary ions, it is not possible to find a simple scaling factor for the normalization of the spectra. The neutrons are indeed produced by different reaction mechanisms. The excess at high-energy, present in the neutron spectra generated by the ions, cannot be parameterized as its shape changes with the ion type.

Chapter 3. Theoretical framework

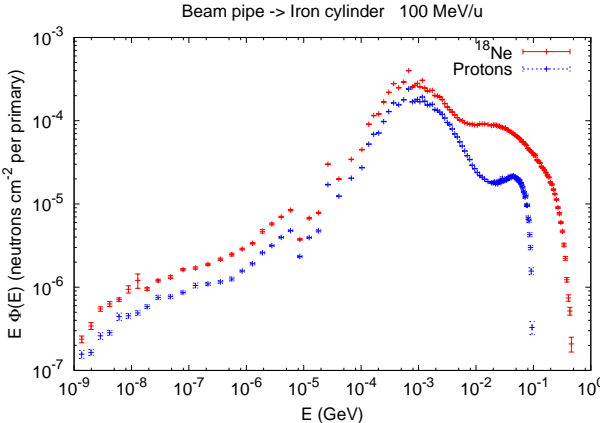


Figure 3.19: Neutron fluence at 100 MeV per nucleon at the boundary between the beam pipe and the magnet yoke. Comparison between ¹⁸Ne ions and protons (intensity normalized to the ¹⁸Ne intensity).

4 Radiation protection parameters and methods

4.1 Radiation protection aspects

Radiation protection aims at protecting humans and their environment from the effects of ionizing radiations by preventing any deterministic pathology caused by irradiation and by minimizing stochastic effects [54], [55]. According to the publication 103 of the International Commission on Radiological Protection (ICRP), three exposure conditions are to be considered:

- planned exposure: e.g. use of radioactive sources with a well-defined procedure;
- emergency exposure: unexpected situation of exposure which requires a urgent action;
- pre-existing exposure: situations which are already existing when a decision on control has to be taken (natural exposure, residual activity, radon, etc.).

In addition, three exposure categories have been defined: occupational exposure, public exposure and medical exposure (the latter includes the patient, the patient's family, anyone exposed within the framework of biomedical research). In order to set protection levels two approaches can be employed: source-oriented or individual-oriented. In the former case the individual dose (*dose constraint*) in planned exposures is assessed with respect to the source and must not be exceeded, but it does not represent a true legal limit. In the latter case, which only applies to planned exposures, the dose (*individual dose limit*) is fixed and it is equal to the sum of doses arising from all regulated sources. The source-related restriction for emergency and existing exposures is the *reference level*.

Radiation protection is based on three main principles: Justification, Optimization and individual dose Limits (JOLI). According to the justification principle, any activity involving a radiological risk must be justified and alternative procedures must be taken when necessary. In order to determine the justification, a cost-benefit analysis should be used, i.e. the net benefit of an activity involving ionizing radiation is given by the difference between the

gross benefit and the sum of three components: the cost of production, the cost necessary to guarantee a selected protection level and the cost of damages. As many factors cannot be easily quantified, when damage is to be estimated, collective dose is often used. This quantity represents the sum of all individual doses received by individuals in a population. Stochastic effects due to radiation do not have a known threshold, therefore their detection is not possible. Optimization is necessary and doses have to be maintained as low as it is reasonably possible, as it is stated in the ALARA (As Low As Reasonably Achievable) principle. Among the possible optimization methods, the cost-benefit analysis is usually employed. However, justification and optimization are not enough to prevent the risk of committing too high doses to a number of individuals: dose limits must be defined. According to ICRP, a dose limit represents a value above which the dose becomes unacceptable, but again the lack of threshold for the stochastic effects represents a problem in the assessment of the limits. To get over it, the ICRP made a study of the risk linked to the annual, regular irradiation at a given dose across 47 years of professional activity, analyzing the following criteria: the probability of death due to irradiation, the years lost following a death due to irradiation, the decrease in life expectancy, the annual distribution of the probability of death due to irradiation and the increase in the mortality rate as a function of the age. In addition, the risk of a non-fatal cancer was estimated to be 20% of the risk of a fatal-cancer, hereditary effects were estimated to represent 20% of the risk of dying from cancer for a population of workers, i.e. 26% of the entire population. These indicators were calculated on the basis of a multiplicative model for annual doses of 10, 20, 30 and 50 mSv and the results show that 20 mSv is the annual effective dose limit that guarantees a “tolerable” risk.

Besides stochastic effects, deterministic risks have to be taken into account. For this purpose some preliminary considerations must be summarized: in a situation of single-organ irradiation stochastic effects have lower thresholds, excluding the skin and the surface of the bones; there are no deterministic effects associated with the irradiation of the bones, whilst the eye’s lens and the extremities are not susceptible to stochastic effects. Given this, additional limits are necessary for preventing deterministic effects and they concern the equivalent dose (see next section) to eye’s lens, skin and extremities.

- $H_{lens} < 0.15 \text{ Sv/year}$
- $H_{skin} < 0.5 \text{ Sv/year}$
- $H_{extremities} < 0.5 \text{ Sv/year}$

4.1.1 Quantities and units in radiation protection

“The determination of quantities relevant to radiation protection often entails significant uncertainties, and approximations will need to be introduced. However, it is essential that the quantities employed be unambiguously defined, and that the approximations be clearly identified”. This is stated at the beginning of the report 51 of the International Commission on Radiation Units and measurements (ICRU) [56], which aims to provide a single clear

presentation of a coherent system of quantities and units for use in radiation protection dosimetry in compliance with dose limitations. Only the quantities relevant for this work are described in the following.

The absorbed dose D is the energy absorbed per unit mass of any material and is defined as:

$$D = \frac{\Delta E}{\Delta m} [J \cdot kg^{-1}] = [Gy]. \quad (4.1)$$

It characterizes the quantity of energy deposited locally at a given location in matter and can be defined for any type of indirectly or directly ionizing radiation; it is a pure physical parameter which does not include biological effectiveness of the radiation and the energy distribution throughout a radiation trace. Depending on the type of radiation, the effects on living organisms can be very different, up to two orders of magnitude between electrons and heavy charged particles. This phenomenon is due to the differences in the microscopic energy distribution in matter which is characterized by a Linear Energy Transfer (LET), i.e. the energy lost per unit of track length by secondary electrons. In order to take into account the biological effects of radiation the quantity of Relative Biological Effectiveness (RBE) was introduced and it is defined as:

$$RBE = \frac{D_{ref}}{D} \quad (4.2)$$

where D_{ref} is the absorbed dose of a reference radiation and D is the dose of the radiation of interest. In few words the RBE gives the ratio needed to reach the same effect level.

For radiation protection calculations RBE, which is dependent on tissue type and other parameters, is not commonly used. Instead, the radiation is qualified by a radiation weighting factor w_R . Table 4.1 summarizes the w_R for different radiations defined in the publication ICRP 103. In Fig. 4.1 the curve for neutron weighting factors is showed: indeed w_r for neutrons is not a constant factor but a function of the energy, described by the following relations:

$$w_R = \left\{ \begin{array}{ll} 2.5 + 18.2e^{-[\ln(E_n)]^2/6}, & E_n < 1MeV \\ 5.0 + 17.0e^{-[\ln(2E_n)]^2/6}, & 1MeV \leq E_n \leq 50MeV \\ 2.5 + 3.25e^{-[\ln(0.04E_n)]^2/6}, & E_n > 50MeV \end{array} \right\}. \quad (4.3)$$

The dose equivalent H is a quantity derived from the absorbed dose through the w_R :

$$H = w_R D_R [J \cdot kg^{-1}] = [Sv] \quad (4.4)$$

The unit for H is called Sievert. Even if it has the same dimensions as D ($J \cdot kg^{-1}$), it was given a different name to remind that both biological and physical principles were taken into

Chapter 4. Radiation protection parameters and methods

Radiation type	Radiation weighting factor, w_R
Photons	1
Electrons and muons	1
Protons and charged pions	2
Alpha particles, fission fragments, heavy ions	20
Neutrons	A continuous function of neutron energy (see Fig. 4.1)

Table 4.1: Radiation weighting factors according to ICRP 103.

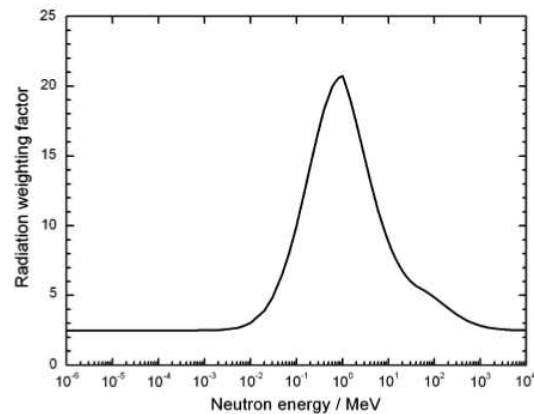


Figure 4.1: Recommended radiation weighting factors for neutrons as a function of neutron energy.

consideration. In the case of different radiations the dose equivalent can be expressed as the weighted sum over the radiations R of the absorbed doses:

$$H = \sum_R w_R D_R \quad (4.5)$$

As dose equivalents cannot be directly measured, in operational radiation protection operational parameters were defined: for ambient dosimetry it is the ambient dose equivalent $H^*(d)$ and for personal dosimetry it is the personal deep dose H_p . $H^*(d)$ in a radiation field is the dose equivalent that would be produced by the corresponding expanded and aligned field at a depth d in millimeters on the radius of the reference ICRU sphere in the direction of the aligned field (Figure 4.2). The ICRU sphere is 0.3 m in diameter with a density of 1000 kg m^{-3} and a mass composition equivalent to tissue of 76.2% oxygen, 11.1% carbon, 10.1% hydrogen and 2.6% nitrogen. The field is expanded so that it encompasses the sphere and aligned so that the quantity is independent of the angular distribution of the radiation field. For the measurement of radiations that are strongly penetrating into the body the reference depth in the sphere is 10 mm, and the quantity is denoted as $H^*(10)$. For the estimation of

the dose to the skin and eye lens, particularly from less penetrating radiations, the reference depths of 0.07 mm and 3 mm respectively with the notations $H^*(0.07)$ and $H^*(3)$ are used. $H_p(d)$ is the dose equivalent in soft tissue beneath a thickness of d (mm) in correspondence of the chest.

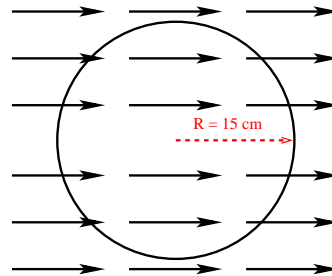


Figure 4.2: The ICRU sphere.

When the irradiation is heterogeneous the dose equivalent has different distributions in the body. The ICRP thus introduced the notion of effective dose E , in order to express the risk from an exposure of a single organ or tissue in terms of the equivalent risk from an exposure of the whole body:

$$E = \sum_T w_T \cdot H_T. \tag{4.6}$$

In Table 4.2 the radiation weighting factors w_T , for several organs and tissues, are summarized. They express the fraction of radiation risk associated with the organ or tissue in the case where all organs and tissues receive the same dose. The unity of E is Sievert. The remainder

Organ or tissue	w_T	$\sum_T w_T$
Surface of the bone, skin	0.01	0.02
Bladder, breast, liver, esophagus, thyroid, remainder	0.05	0.30
Bone marrow, colon, lung, stomach	0.12	0.48
Gonads	0.20	0.20
Total		1.00

Table 4.2: Radiation weighting factors w_T per organ group, according to ICRP 103.

is composed of adrenal glands, brain, upper part of the intestine, small intestine, kidneys, muscle, pancreas, spleen, thymus and uterus.

Finally, the dose by intake, due to ingestion or inhalation, is called committed effective dose E_{50} and represents the sum of the effective doses per unit of time $E(t)$ received over 50 years

after the intake:

$$E_{50} = \int_{t_0}^{t_0+50\text{years}} E(t) dt, \quad (4.7)$$

where t_0 is the moment of intake. E_{50} depends on the half-life of the radionuclide and on its physiological effect, and, for a given nuclide, can be deduced from the knowledge of the inhaled and ingested activities and of the activity-to-dose conversion coefficients:

$$E_{50} = e_{inh} \cdot A_{inh} \quad (4.8)$$

$$E_{50} = e_{ing} \cdot A_{ing} \quad (4.9)$$

The activity-to-dose coefficients for inhalation and ingestion for public and workers can be found in a cd-rom issued by ICRP in 1998 [57].

4.1.2 Radiation protection at CERN

Radiation protection at CERN is performed in compliance with the rules of the CERN Safety Code [58], which is based on the most advanced standards set out in the European and other relevant international legislations. It applies to all people working at CERN and its environment, including the underground areas. Where no direct reference to the legislations is possible, the European Union directives, the ICRP recommendations and the IAEA standards are employed [55].

Following the JOLI principle, individual dose limits are applied at CERN. The effective dose received in a 12-month period by occupationally exposed-to-radiation workers must not exceed 20 mSv and the dose equivalent must not exceed 150 mSv for the eye's lens and 500 mSv for the skin and the extremities. The effective dose for non occupationally-exposed people, for the same period, must not exceed 1 mSv. Exceptional exposures to radiation, exceeding the limits, are permitted in case of emergencies: 50 mSv in a 12-month period (or 250 mSv for the saving of human lives) is allowed. There are two categories of exposed people:

- Category A: people who may be exposed in the exercise of their profession to MORE than 3/10 of the limit in terms of effective dose in 12 consecutive months.
- Category B: people who may be exposed in the exercise of their profession to LESS than 3/10 of the limit in terms of effective dose in 12 consecutive months.

Limits to prevent radiation hazards are also applied to the areas, which are classified according to the framework in Table 4.3. Non designated-areas are accessible to the public and

4.1. Radiation protection aspects

dosimeters are not required, whilst supervised and controlled areas can only be entered by radiation workers equipped with a personal and/or operational dosimeter. Inside the con-

Type of Area	Max annual effective dose	Max ambient dose equivalent rate		Access, personnel categories
		At permanent workplace	In low-occupancy areas	
Non designated	1 mSv	$<0.5 \mu\text{Sv h}^{-1}$	$<2.5 \mu\text{Sv h}^{-1}$	no restriction, all
Supervised	6 mSv	$<3 \mu\text{Sv h}^{-1}$	$<15 \mu\text{Sv h}^{-1}$	supervised, radiation workers
Controlled radiation areas				
Simple controlled	$<20 \text{ mSv}$	$10 \mu\text{Sv h}^{-1}$	$< 50 \mu\text{Sv h}^{-1}$	controlled radiation worker
Limited stay	$<20 \text{ mSv}$		$< 2 \text{ mSv h}^{-1}$	"
High radiation	$<20 \text{ mSv}$		$< 100 \text{ mSv h}^{-1}$	" "
Prohibited	$<20 \text{ mSv}$		$>100 \text{ mSv h}^{-1}$	"

Table 4.3: CERN Radiation Safety Code: classification of radiation areas

trolled radiation areas, a further classification distinguishes in simple-controlled, limited-stay, high-radiation and prohibited areas. Apart from the simple-controlled ones, all the other ones are low-occupancy areas. In particular, in the limited-stay and high-radiation areas, the dose rates can lead to individual doses beyond the limit if the exposure last 2000 hours per year, which is the reference scenario. This implies that the workers can only spend a short time in these areas, unless they are authorized to emergency interventions.

CERN monitors the impact that all facilities have on the environment: the direct exposure to stray radiation, the airborne activities, the contaminated liquid releases, the elimination of radioactive waste and the transport of radioactive parcels. A quantitative impact study [59] led to the definition of activity constraints based on dose limits for people living in the surrounding of CERN. The constraints are conservative and take into account other sources of exposure, like natural irradiation (cosmic particles and earth radioactivity), radon, clean radiation (in the body), medical exams, professional exposure and other artificial sources. Hence the effective dose resulting from CERN's activities received by the public outside the

site boundaries must not exceed 0.3 mSv per year, including external and internal exposure; the equivalent dose must not exceed 15 mSv per year for the eye's lens and 50 mSv per year for the skin. For airborne releases, a maximum effective dose of 10 μ Sv per year was chosen as the limit for all CERN installations.

4.2 Monte Carlo calculations and analytical methods

In order to assess all the radiological risks of the beta-beam facility, both Monte Carlo (MC) calculations and analytical models are employed. The former are required because of the lack of available experimental data in literature for radiation protection at ion facilities and more in general for nucleus-nucleus reactions. Indeed, information about the radioactive ions ${}^6\text{He}$ and ${}^{18}\text{Ne}$ is not available for the energy range of beta beams which is considered in this work. The MC code FLUKA is used for the simulations with the interface to the BME model for reactions occurring below 100 MeV per nucleon. It is employed for the calculations of particle track-length spectra, for the residual nuclide production and the consequent residual doses, for the on-line conversion of particle fluence to dose. Besides MC, also analytical methods are used, for the calculation of shielding thicknesses and for the diffusion of the activated air through the ventilation outlets.

4.2.1 Prompt radiation and shielding: models and biasing techniques

In accelerator design, shielding plays an important role, as it reduces exponentially the intensity of radiation. An optimized design thus allows people to access the accelerator-annexed areas during operation and also reduces the construction costs. In order to draw an optimized shield, a three-stage procedure is followed: assessment of the source terms, definition of the dose constraints and finally design of the shield taking into account effectiveness and costs. In the next section the model used for the assessment of the source term is described.

4.2.1.1 Point source and line of sight model

Models that aim at simplifying the calculations are usually used in shield calculations [55]. They are effective with point losses and lateral shielding, but less so for shielding continuous losses characterized by non-uniform distributions and in forward shieldings. A noticeable review of these methods, with their strengths and limits, can be found in [60], where it is demonstrated that the point-of-source/line of sight model, or its extended version (Moyer model) for the GeV range, can be used when losses are punctual. In such models, the attenuation of the dose through the shield follows an inverse square law of the distance from the source. Two main assumptions are made:

- the source can be approximated to a point-source S (see Figure 4.3), if it is localized in a region small in size compared with the dimensions of the shielding situation so that the

inverse square law of geometrical dilution holds;

- the dose, as a function of position, can be described only in terms of the point source coordinates and of the point of interest P, without contributions from other secondary sources.

All these elements are summarized in the two-parameter formula:

$$H(E_p, \theta, \frac{d}{\lambda}) = \frac{H_0(E_p, \theta)}{r^2} \exp \left[-\frac{d}{\lambda_\theta g(\alpha)} \right], \quad (4.10)$$

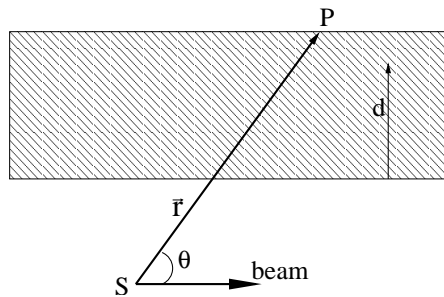


Figure 4.3: Point-source/Line of sight sketch.

where H is the dose behind the shield, r is the line-of-sight distance between the source S and the point P , E_p is the primary particle energy, θ is the polar angle of the vector r with respect to the beam axis, H_0 is the source term, d is the depth in the shield, $\lambda(\theta)$ is the attenuation length at the emission angle θ that depends on the shielding material, α is the angle between the direction of r and the normal to the surface. The function $g(\alpha)$ is equal to 1 in spherical geometries and to $\cos(\alpha)$ in all the other cases. When losses are not punctual, an approximation is still possible, that allows using the model. It was demonstrated in [61] that also uniform continuous losses occurring in a section of length l can be approximated as point losses every l , provided that the total power is conserved, as shown in Figure 4.4.

In the case of non-uniform distribution, when precise loss maps are available, MC simulations with realistic geometries can be exploited to calculate the source terms and the attenuation lengths in the shield. Both in the case of point sources and distributed losses, particle fluences in the concrete layers are scored and converted into ambient dose equivalents with an on-line routine [62], which applies the conversion coefficients from fluence to dose based on spline-fits of coefficients suggested by ICRP74 [63] and of values calculated by Pelliccioni with FLUKA [64, 65].

4.2.1.2 Biasing

Biasing is a MC technique that allows the user to reduce the calculation time (CPU) by estimating average, instead of exact, quantities. The CPU time is reduced by sampling from

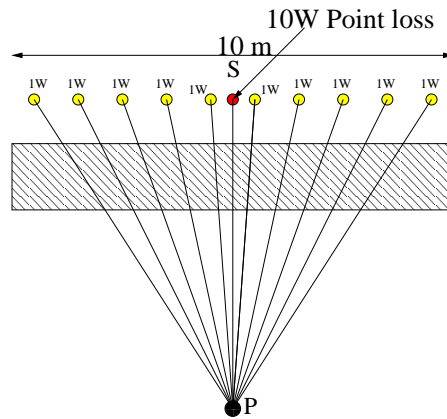


Figure 4.4: Sketch for the approximation of a uniform loss with a point loss.

biased distributions [36]. In shielding studies, especially when the shield thickness becomes important, biased MC should be used instead of analogue MC [66]. In the analogue MC, events are sampled according to their actual physical probability, while in a biased MC the distribution function is modified (“biased”) in order to produce a more efficient calculation. In an analogue MC simulation there are many advantages: sampling from the actual phase space distributions, correlations are preserved, fluctuations can be reproduced as long as the same physical models are used. But it has three main drawbacks: it fails in predicting rare events, it is inefficient and requires excessive CPU time when trying to reduce the statistical error. Biased MC samples from an artificial distribution and applies a weight to the particles, predicts average quantities and has the same mean with a small variance. Of course, besides faster convergence, it also presents some disadvantages: correlations and fluctuations cannot be reproduced, the modified probabilities must be evaluated according to the actual physics model. There are several biasing techniques, of which some reduce the CPU time t , some reduce the standard deviation σ . The most commonly used is the *importance biasing*, which maintains a uniform particle population, otherwise decreased by absorption or distance. It combines two techniques, called *surface splitting* and *Russian roulette*: the former increases t and reduces σ , the latter does the opposite. With both, each geometry region in the simulation is assigned a relative importance based on the expected fluence attenuation in passing to other regions and on the probability of contribution to the scored quantity given by particles entering the region itself. The *surface splitting* applies to those cases where a particle crosses a boundary, going from a region of importance I_1 to a region with higher importance I_2 : the particle is replaced by a quantity $\frac{I_2}{I_1}$ of identical particles with a weight equal to $\frac{I_1}{I_2}$. In the *Russian roulette*, the particle passes to a region of lower importance, therefore a survival test is performed: the particle survives with a chance $\frac{I_2}{I_1}$ and its weight is increased by a factor $\frac{I_1}{I_2}$; otherwise it is suppressed with a chance $\frac{1-I_2}{I_1}$.

Other techniques are available. The *weight windows* is a biasing technique based on the absolute value of particle weight, which is assigned between a lower and a higher limit. It

is essential whenever the other biasing techniques generate large fluctuations; the *leading particle biasing* for electromagnetic showers and the *multiplicity tuning* for secondary hadrons can be employed to reduce the number of secondary particles and the CPU time by discarding a fraction of them and re-adjusting the weight of all left particles in order to preserve the total weight; the *non-analogue neutron absorption*, which is also called *survival biasing*, is used for low-energy neutron transport: at each interaction one can choose between either analogue scattering or absorption according to the physical probability $\frac{\sigma_s}{\sigma_T}$ and $1 - \frac{\sigma_s}{\sigma_T}$, or systematic survival reduced by a factor $\frac{\sigma_s}{\sigma_T}$, where σ_s is the scattering probability and σ_T is the total probability; the *biasing mean-free paths* is generally adopted to enhance statistics in muon or neutrino production by shortening the mean life of unstable particles, to increase the probability for beam interactions in a thin target or in a low-density material by decreasing the mean free path for nuclear interactions.

In all the shielding calculations, the *importance biasing* with the *surface splitting* option, is used and Figure 4.5 gives a pictorial representation of how it works. From a particle with weight w in a geometry region of importance 1, two new particles are generated in the following region with importance 2 and each one is assigned a weight $w/2$.

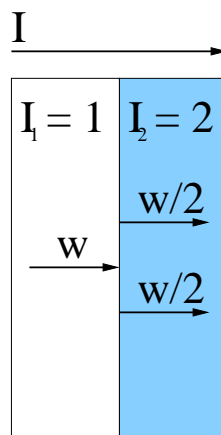


Figure 4.5: Pictorial representation of the *surface splitting* biasing technique.

4.2.2 Induced activity: residual doses, radionuclide inventory, airborne activity

The evaluation of induced activity in high-energy accelerators is of major importance to keep the exposure of the personnel and the impact on the environment as low as reasonably achievable. Therefore it plays a decisive role in the facility design phase, in planning interventions and in the decommissioning. In the assessment of induced radioactivity there are several methods that can be used, and among them three are commonly employed [67]: the multiplication of the density of inelastic interactions by hadrons with energies higher than 50 MeV (*stars*) with pre-calculated conversion factors (ω factors), the convolution of predicted particle track-length spectra with isotope cross sections and an explicit calculation of isotope

production through hadronic interaction models. Depending on the situation, one of the three methods can be used: the multiplication of star densities represent a rough estimate, the convolution method applies to low-density materials, the explicit calculation is the most used approach for solid materials as it would fail in low-inelastic interaction probability cases (i.e. in gases).

4.2.2.1 Residual doses and radionuclide inventory

The assessment of residual doses is done entirely with FLUKA calculations, using detailed geometries that include all major beamline components, i.e. bending magnets, quadrupole, injection septa, beam-pipe, collimators, the walls and the floors in the tunnels, etc. During the same simulation, when radioactive residual nuclides are produced, their build-up and decay are calculated for a certain irradiation profile and for an arbitrary number of waiting times. The implementation is based on the exact analytical solution of the Bateman equations [68] and on the transport and interactions of the emitted gamma and beta radiation in the materials. Ground states and isomeric states are distinguished, heavy-residue emission and coalescence are taken into account, the electromagnetic component of the radiation is activated only in the decay part and de-activated, via a threshold setting, in the prompt part. Low-energy neutrons are transported down to thermal energies. The explicit calculation of the produced radionuclides cannot be replaced by simplified analytical calculations except for limited cases. For example, the so-called ω -factors are limited to homogeneously irradiated objects and assume that the production is proportional to the density of high-energy interactions. As these hypotheses are not valid for the present study, the method of the ω -factors has not been used. The activation of materials is caused by several types of nuclear reactions, like high-energy inelastic hadron interactions, neutron radiative capture and photonuclear reactions [69], just to mention the most important ones. Both primary ions and secondary particles produce radionuclides by interacting with the target materials. In summary, in a simulation the residual ambient dose equivalent rate is assessed in the implemented geometry, following the irradiation profile and the waiting time set. The list of the produced radionuclides and their specific activity is also calculated. This information is particularly useful for an evaluation of the future radiological characterization of the materials, when they have to be disposed of as waste. Also, it can be used as guideline for optimizing the choice of the materials at the design stage. Depending on the expected levels of residual dose rates, the accelerator sections are classified according to the CERN Safety Code, as summarized in Table 4.3.

4.2.2.2 Air activation

In the calculation of airborne induced activity and of the subsequent effective dose, the convolution of particle track-length spectra with isotope-production cross sections is commonly used. Track-length energy spectra are calculated through simulations, involving the transport of protons, neutrons and charged pions through air. The convolution of the spectra with the isotope production cross sections, summed over all target nuclei and hadron components,

gives the yield Y_i of a radionuclide i through the following relation:

$$Y_i = \sum_{j,k} n_j \int \sigma_{i,j,k}(E) \Lambda_k(E) dE, \quad (4.11)$$

where n_j is the atomic concentration of the element j in the target, $\sigma_{i,j,k}(E)$ is the production cross-section for the radionuclide i created in the reaction of the particle k of energy E with a nucleus in the element j ; $\Lambda_k(E)$ is the sum of the track lengths of the particle k . For the beta-beam study a data base with evaluated particle interaction cross-sections for the production of the most abundant radionuclides in the air has been used [70]: it was calculated for the air activation of the LHC. It covers the energy range from 10 MeV to 10 TeV for charged hadrons. Low-energy neutrons are scored in the 72-energy group structure (now a 260 one is available within the FLUKA code) of the neutron scattering cross sections. In the calculations, the simulated track-length spectra are folded with the cross-sections and then the obtained yields are normalized to the total number of particles lost in a year N_p .

The airborne activity represents a concern for workers accessing the accelerator tunnels and for people living in the surrounding of the release stacks. Therefore both the doses to workers and to the public must be estimated at the design phase of a machine. For the former one, the calculations are done for the case of failure of the ventilation system. Indeed, the inhalation dose would be negligible under normal conditions: the ventilation system removes the radioactive air before the access. Several scenarios are considered in terms of irradiation and waiting times (the time elapsed between the end of the irradiation and the access). A 1-hour intervention is assumed in all calculations. If the activity is distributed homogeneously over the air volume, after a given irradiation time t_{irr} and a waiting time t_{wait} , the specific activity can be expressed by:

$$A_{rel}^{tunn} = \frac{1}{V} \sum_i A_s (1 - e^{-\lambda_i t_{irr}}) e^{-\lambda_i t_{wait}}, \quad (4.12)$$

where $A_s = Y_i \cdot N_p$ is the saturation activity of the airborne radionuclide i , V is the irradiated volume of air and λ_i is the decay constant of the radionuclide. In the conversion from activity to dose several factors are taken into account: the breathing rate b_r [71] and the inhalation conversion factors e_{inh} given by the Swiss legislation [72]. The standard breathing rate for a worker is $1.2 \text{ m}^3 \text{ h}^{-1}$. Eq. (4.12), integrated over the intervention time t_{int} , via the conversion coefficients, gives the inhalation dose D :

$$D_{inh} = A_{rel}^{tunn} e_{inh} b_r \sum_i \frac{(1 - e^{-\lambda_i t_{int}})}{\lambda_i}, \quad (4.13)$$

Besides the inhalation dose, workers are also undergoing an external exposure due to the activity in the air and this is accounted through conversion coefficients for air submersion: for each radionuclide the organ equivalent dose coefficient h_T and the effective dose coefficient

Chapter 4. Radiation protection parameters and methods

h_E , based on the ICRP weighting factors and calculated by Eckerman and Ryman in [73], are used. They take into account the external exposure to photons and electrons emitted by the airborne radionuclides and include the results of calculations of the energy and angular distributions of the radiation incident upon the human body and the transport within it. Only photons, including *bremsstrahlung*, and electrons are considered because they are sufficiently penetrating to contribute to the dose to tissues and organs. For each radionuclide the organ dose equivalent coefficients and the effective dose equivalent coefficient are provided, based on the ICRP weighting factors, which apply for air at a density of 1.2 kg m^{-3} .

For the estimate of doses to the public, both diffusion due to the winds and deposition in environmental matrices must be considered. For the external exposure, the effective dose integrated over one year shall be calculated. For the internal exposure, the effective dose committed during the rest of life due to inhalation and/or ingestion of radioactive substances in one year shall be evaluated. These factors, together with dispersion and deposition factors, were considered in a previous study [59] and the resulting conversion coefficients from activity to dose are employed for the beta-beam impact evaluation. The available coefficients were calculated for several facilities at CERN and in this work the set chosen for each machine depends on its location, whether it is in France or Switzerland, and on its distance from dwellings or work places. For all machines an irradiation time of 10^7 seconds (\sim three months of operation) per year is considered. For the air diffusion in the tunnel and through the ventilation outlets until the stacks, the laminar flow model is used. This implies that the air is driven to the stack without turbulence at a constant speed. Considering N_p the number of particles lost as a function of time in a tunnel section of length L and cross section \mathcal{S} , F the ventilation flow rate, R_i the yield of nuclides of type i produced per primary particle, T_{irr} the annual operation time, then the total activity released in one year is:

$$A_{rel}^{env} = \sum_i \frac{F}{\mathcal{S}L} N_p R_i T_{irr} (1 - e^{-\frac{L\lambda_i}{F}}) e^{-T_{decay}\lambda_i}. \quad (4.14)$$

The total activity is then converted into annual effective dose through the conversion coefficients. The contributions from the several machines in beta beams are taken into account and compared with the reference value for the total allowed emission into the environment from CERN installation, which corresponds to $10 \mu\text{Sv}$ per year.

In the characterization of the airborne activity, radionuclides are usually divided into two groups, according to their half-life, whether it is less or more than a day. In the list of short-lived radionuclides of environmental importance, ^{11}C , ^{13}N , ^{15}O and ^{41}Ar can be listed: the latter is a product of low-energy neutron capture on argon whilst the other ones are spallation reaction products. In particular, ^{11}C comes from reactions on nitrogen and oxygen with channels of large cross-section, typically $^{14}\text{N}(p,\alpha)^{11}\text{C}$ and $^{14}\text{N}(\pi,^3\text{H})^{11}\text{C}$; ^{13}N is produced in $(n,2n)$ reactions on nitrogen; ^{15}O is only created in reactions with oxygen, such as neutron removal (π,n) or $(n,2n)$. ^3H and ^7Be dominate at long half-lives and are produced by spallation reactions on nitrogen and oxygen at high energy, but other isotopes contribute to this group:

^{14}C by (n,p) reactions on nitrogen, ^{10}Be by (n, α p) on nitrogen, ^{37}Ar in spallation reactions on ^{40}Ar or capture on ^{36}Ar , ^{39}Ar in (n,2n) reactions, ^{36}Cl in reactions of neutrons on argon.

4.3 Conclusions

In this chapter, a review of the principles underlying the foundations of radiation protection and of the consequent implementations was given. Quantities used in all calculations were described from their derivation to the units in which they are expressed. The CERN Safety Code was summarized with respect to the radiation protection rules: the dose constraints used as reference values for beta beams were reported. The MC and analytical methods employed for calculations were described. Models available in literature, which aim at simplification, and biasing techniques which help at improving the statistics in shield calculations were summarized. Finally, the methods used for induced-activity studies, i.e. airborne activity and residual doses, which make use of both MC simulations and analytical calculations, were described. In the next chapters, the results of the radiological risk assessment based on these methods, are presented for the RCS, PS and DR.

5 The Rapid Cycling Synchrotron (RCS)

The Rapid Cycling Synchrotron (RCS) is conceived to bunch and accelerate the beam in the intermediate-energy range, from 100 MeV per nucleon to 787 MeV per nucleon (${}^6\text{He}$) and to 1.65 GeV per nucleon (${}^{18}\text{Ne}$). The intensity rates of the circulating beam in the ring are $8.6\text{E}12$ ${}^6\text{He}$ ions per second and $2.92\text{E}12$ ${}^{18}\text{Ne}$ ions per second [74]. A schematic layout of the RCS is given in Figure 5.1. It has three-fold symmetry lattice, with three arcs and three straight sections, divided into 24 FODO (i.e. focusing and defocusing) cells: 6 in each arc and 2 in each straight section. It has a physical radius of 40 m and a length of 251.32 m. The RCS main parameters are summarized in Table 5.1. The betatron phase advance per cell (i.e. quadrupole

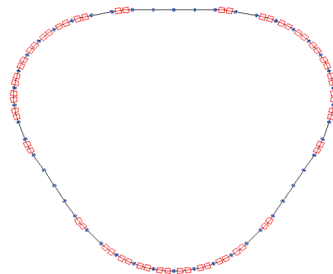


Figure 5.1: Layout of the RCS.

strength) and the length of the 2 sections without dipoles in the arcs have been adjusted so as to cancel the dispersion function in long straight sections. Lattices function of one period calculated with the code BETA [75] are shown in Fig. 5.2. Dipoles are only 1.4 m long in order to obtain a maximum magnetic field of 1.08 T and therefore to avoid a large ramping rate for the 10 Hz operation. Quadrupoles have a length of 0.4 m and a maximum gradient of less than 11 T/m.

Circumference	251.32 m
Physical radius	40 m
Injection energy	100 MeV/u
Maximum magnetic rigidity	14.47 T·m
Repetition rate	10 Hz
Number of dipoles	60
Number of quadrupoles	48

Table 5.1: Main parameters of the ring.

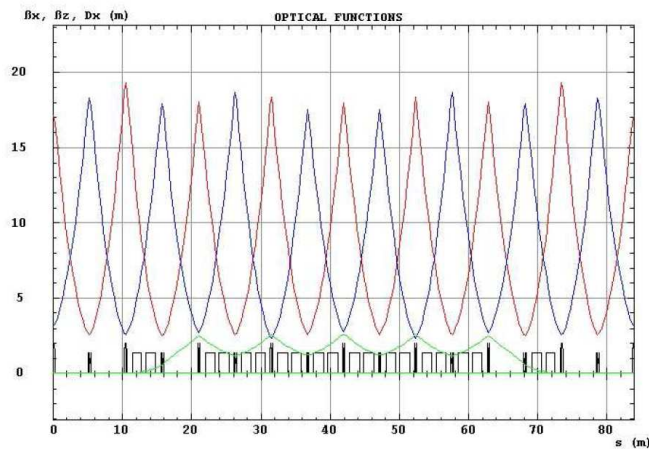


Figure 5.2: Optical functions for one super-period [74].

5.1 Beam losses

Losses in the RCS are located at the injection septum and in the arcs. They are divided into injection, decay, Radio-Frequency capture (RFc) and acceleration losses. Figure 5.3 portrays the positions in the machine where they occur.

The multi-turn injection process takes place over 26 turns in the machine. Ions are injected into one of the long straight sections through an electrostatic septum and by two pulsed kickers, which produce a local closed orbit bump. The distorted orbit is placed near the septum for the first injected turn and moved away from the septum on the following turns until it has collapsed. In this way, the number of injected ions is maximized within the specified transverse emittance. In spite of the parameter optimization, part of the beam is lost against the septum blade. The injection efficiency is 70%. Decay losses are uniformly distributed all over the machine and affect, in terms of power deposited, the dipoles in the arcs. In total, they account for 3.6% of the beam intensity for ${}^6\text{He}$ and 1.35% for ${}^{18}\text{Ne}$. Radio-frequency capture (RFc) and acceleration losses represent the most relevant percentage of losses in the machine after injection losses, as it can be seen in Figure 5.4, where the decay and RFc-acceleration loss

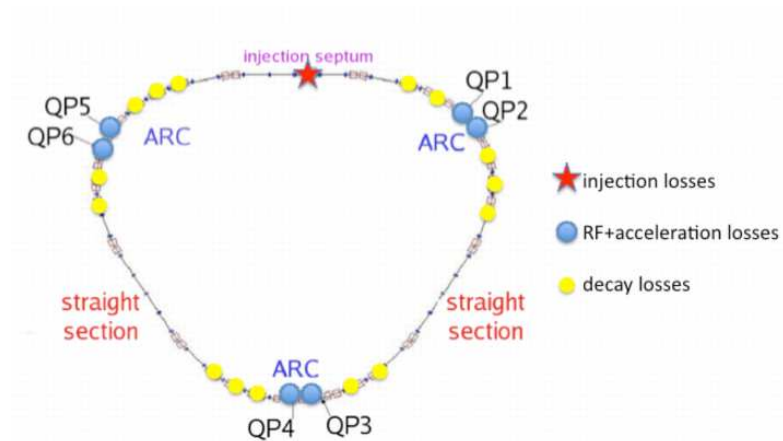


Figure 5.3: Layout of the RCS with the different kinds of losses and their locations in the ring.

intensities along the ring are plotted for ${}^6\text{He}$ (top) and for ${}^{18}\text{Ne}$ (bottom): the x-axis represents the position along the RCS circumference, the y-axis the losses, on the left in arbitrary units, on the right in percentages of the injected beam intensity. They are point losses and occur in the families of quadrupoles in the arcs (13.3% of the beam for ${}^6\text{He}$, 23% of the beam for ${}^{18}\text{Ne}$). In Table 5.2 all losses are given with their production mechanism and percentages of the beam intensities.

Energy (MeV/u)	Injection	Decay	RFc+acceleration
100	30%	0.10(0.45)%	5.70(9.40)%
400(640)	-	0.80(0.20)%	2.85(8.50)%
787(1650)	-	1.80(0.70)%	4.75(5.05)%

Table 5.2: Loss percentages for several energies and for the production mechanism for ${}^6\text{He}$ (${}^{18}\text{Ne}$).

5.2 Shielding calculations

For the shielding calculations, the attenuation lengths and the source terms in concrete are calculated at 4 different energies in the RCS energy range for both the ions with the MC simulations. A simplified geometry is employed (Figure 5.5): the ion beam impinges onto a cylindrical copper target, of several thicknesses (depending on the energy of the primaries) along the beam axis and 10 cm in the lateral direction. A 10 m long hollow iron cylinder with 6 cm inner radius and 2 mm thick wall, filled with the FLUKA material vacuum, represents the beam pipe. The whole assembly is located in a cylindrical tunnel ($r = 2$ m) filled with air, surrounded by a 5 m thick concrete cylinder. The concrete has a density of 2.35 g cm^{-3} , with a mass fraction of hydrogen equal to 0.006. The concrete wall is divided into 20 cm

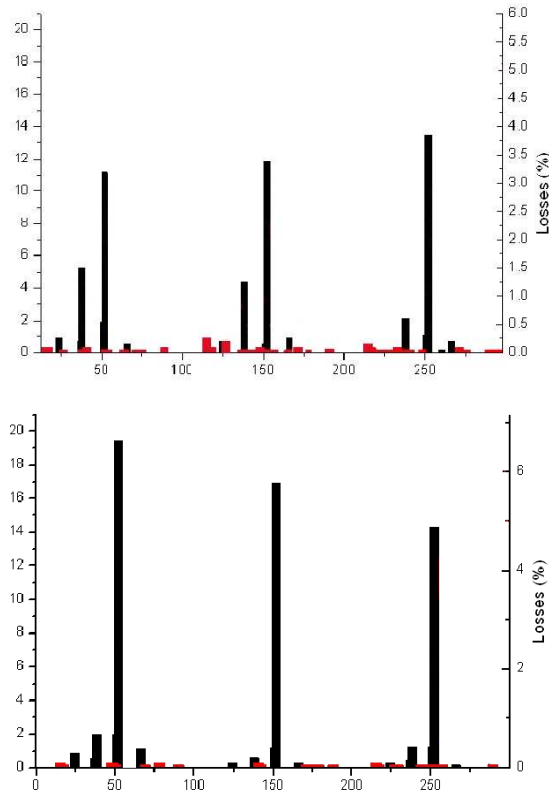


Figure 5.4: Intensities for decay (red) and RFC-acceleration (black) losses for ${}^6\text{He}$ (top) and for ${}^{18}\text{Ne}$ (bottom); the x-axis represents the position along the RCS circumference (m) and the y-axis the loss in arbitrary units on the left, in percentages of the injected beam intensity on the right.

thick concentric layers. Fluences are scored in each layer and converted into ambient dose equivalents as explained in Chapter 4. The importance biasing with the surface-splitting option is performed on the concrete layers, with a splitting weight of $w/2$ (see Chapter 4, Section 4.2.1.2, for details on the method). From the interpolation of the ambient dose equivalent as a function of the concrete depth, the source term H_0 and attenuation length λ are calculated [55]. In Figures 5.6 and 5.7 the attenuation curves in concrete at an angle of 90° are shown together with the interpolating curves, for ${}^6\text{He}$ at 100, 200, 400 and 787 MeV per nucleon and for ${}^{18}\text{Ne}$ at 100, 250, 640 and 1650 MeV per nucleon, respectively. Indeed, RCS losses take place in the entire energy range of the machine. The results, which are used for calculating the shielding thicknesses, are shown in Table 5.3. Depending on the location in the machine, the shielding design takes into account the dominant loss mechanism and is calculated for the three dose-rate constraints $H_{Constraint}^*$ of $0.5 \mu\text{Sv h}^{-1}$, $3 \mu\text{Sv h}^{-1}$ and $10 \mu\text{Sv h}^{-1}$. For injection losses, which are point losses, the shield thickness for a given dose rate is calculated according to formula (5.1), where the source term H_0 is multiplied by the loss intensity, in particles per second. r is the distance from the source to the concrete wall, d is

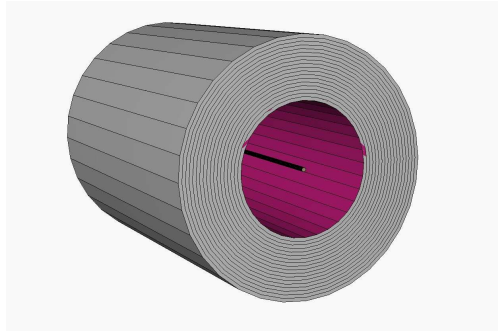


Figure 5.5: Simplified geometry used for the calculation of the source terms and of the attenuation lengths in concrete. 3D visualisation with SIMPLEGEO [76].

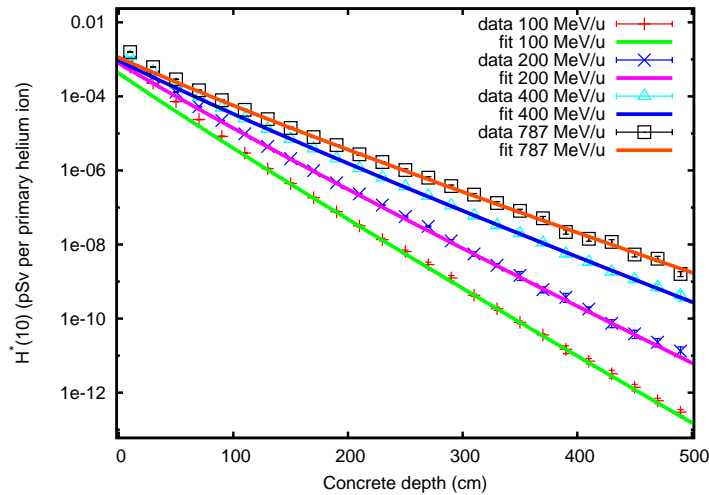


Figure 5.6: Attenuation curves in concrete at 90° for several ${}^6\text{He}$ -beam energies. The data are fitted by eq. (7.1) in Chapter 4.

the depth in concrete, λ is the attenuation length.

$$H_{Constraint}^* = I \frac{H_0}{(r+d)^2} \cdot e^{-\frac{d}{\lambda}}, \quad (5.1)$$

The recommended values, summarized in Table 5.4 include an extra attenuation length as safety margin. Around the injection septum the shielding shall be designed for ${}^6\text{He}$ losses, which represent the worst case. Decay losses occur everywhere in the machine but mainly in the arcs (mostly in the dipoles and to a lower extent also in the families of quadrupoles). It is here used the assumption for the approximation of uniform losses as point losses (for explanations see Section 4.2.1.1 in Chapter 4). As these losses occur during the entire magnetic cycle, the total ambient dose equivalent rate is calculated as the sum of the doses of the three energy intervals i in which the machine range has been divided, namely 100-200 MeV, 200-400

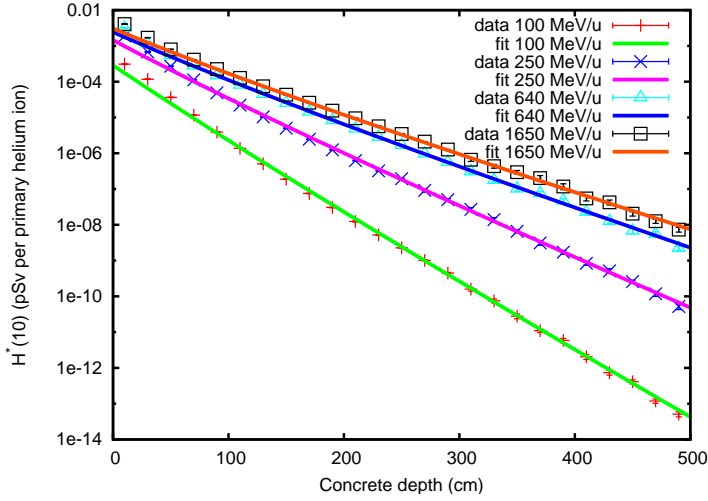


Figure 5.7: Attenuation curves in concrete at 90° for several ^{18}Ne -beam energies. The data are fitted by eq. (7.1) in Chapter 4.

Ion	Energy (MeV/u)	Attenuation length (g cm^{-2})	Source term (E-15 Sv m^2 per primary)
^6He	100	61.6 ± 0.7	1.68 ± 0.12
^6He	200	73.09 ± 0.7	3.14 ± 1.48
^6He	400	94.1 ± 0.2	3.69 ± 0.09
^6He	787	108.5 ± 0.9	4.51 ± 0.14
^{18}Ne	100	58.4 ± 0.7	1.15 ± 0.10
^{18}Ne	250	78.3 ± 1.1	5.79 ± 0.36
^{18}Ne	640	102.9 ± 0.3	9.72 ± 0.09
^{18}Ne	1650	113.7 ± 0.4	12.22 ± 0.08

Table 5.3: Attenuation lengths in concrete and source terms for several energies in the machine range.

and 400-787 MeV per nucleon for ^6He and 100-250, 250-640, 640-1650 MeV per nucleon for ^{18}Ne :

$$H_{\text{Constraint}}^* = \sum_{i=1}^3 \frac{H_{0,i} I_i}{(r+d)^2} e^{-\frac{d}{\lambda_i}}, \quad (5.2)$$

where $H_{0,i}$ and λ_i are the source term and the attenuation length for the energy interval i and I_i is the fraction of particles lost in the energy interval i ($I_i = \text{lost particles s}^{-1} \times 10 \text{ m} \times (120 \text{ m})^{-1}$). Table 5.5 contains the shielding thicknesses for decay losses in the dipoles. ^6He represents the worst case between the two ions. Also RfC-acceleration losses are point losses occurring in the quadrupoles in the arcs, QP1-QP6. Unlike injection losses, they happen for the whole energy range of the machine. The total ambient dose equivalent is thus given by

Injection losses (30%) at nominal intensity:				
		Dose equiv. rate $\mu\text{Sv h}^{-1}$		
		0.5	3	10
ion	energy (MeV/u)	Concrete shield thickness (cm)		
^6He	100	345 (370)	300 (325)	275 (300)
^{18}Ne	100	310 (335)	270 (295)	240 (265)

Table 5.4: Concrete shield thicknesses for injection losses. The values in parentheses represent the recommended values.

Decay losses (3.65% ^6He , 1.35% ^{18}Ne) at nominal intensity:				
		Dose equiv. rate $\mu\text{Sv h}^{-1}$		
		0.5	3	10
ion	energy (MeV/u)	Concrete shield thickness (cm)		
^6He	100-787	390 (435)	325 (370)	275 (320)
^{18}Ne	100-1650	375 (425)	305 (355)	255 (305)

Table 5.5: Concrete shield thicknesses for decay losses. The values in parentheses represent the recommended values.

the sum of the contributions from each energy interval, like in (5.2). The intensity I_i is the number of particles lost per second in a given position in the ring. The results are summarized in Table 5.6. In correspondence of the quadrupole families, the shielding shall be designed for the worst case between the two ions. When considering the families of quadrupoles in the arcs for both decay and RfC-acceleration losses, the recommended values for the shield are those in Table 5.7 (values in parentheses). With respect to the values for only RfC-acceleration losses in quadrupoles, the shield thicknesses appear to be slightly larger but the difference is within the uncertainties of the calculations and well covered by the additional attenuation length, included in all the recommended values.

5.3 Induced activity

For induced-activity calculations, the detailed geometry of the machine sections where losses occur is represented in the MC simulations. In particular, the exact masses are implemented for the calculation of the residual nuclide production. For the injection losses three RCS elements are implemented in the geometry input file: the electrostatic septum, with a tungsten blade (0.2 mm thick, 1.6 m long) and a titanium cathode, and two quadrupoles that follow it in the ring, as shown in Figure 5.8. A detailed image of the inner part of the septum is given in Figure

RFc+acceleration losses (13.3% ⁶ He, 22.95% ¹⁸ Ne) at nominal intensity:					
			Dose equiv. rate $\mu\text{Sv h}^{-1}$		
			0.5	3	10
ion	energy (MeV/u)	Quad (QP)	Concrete shield thickness (cm)		
⁶ He	100-787	QP1	430(475)	360(405)	315(360)
	100-787	QP2	480(525)	410(455)	365(410)
	100-787	QP3	420(465)	350(395)	305(350)
	100-787	QP4	480(525)	405(450)	360(405)
	100-787	QP5	475(520)	405(450)	360(405)
¹⁸ Ne	100-1650	QP1	515(565)	440(490)	390(440)
	100-1650	QP2	470(520)	400(450)	350(400)
	100-1650	QP3	525(575)	450(500)	405(455)
	100-1650	QP4	470(520)	400(450)	350(400)
	100-1650	QP5	510(560)	435(485)	390(440)
	100-1650	QP6	475(525)	405(455)	355(405)

Table 5.6: Concrete shield thicknesses for RFc+acceleration losses.

RFc+acceleration and decay losses at nominal intensity:					
			Dose equiv. rate $\mu\text{Sv h}^{-1}$		
			0.5	3	10
ion	energy (MeV/u)	Quad (QP)	Concrete shield thickness (cm)		
⁶ He	100-787	QP1	440(485)	370(415)	325(370)
	100-787	QP2	485(530)	415(460)	365(410)
	100-787	QP3	435(480)	365(410)	320(365)
	100-787	QP4	485(530)	410(455)	365(410)
	100-787	QP5	480(525)	410(455)	365(410)
¹⁸ Ne	100-1650	QP1	515(565)	440(490)	390(440)
	100-1650	QP2	475(525)	400(450)	355(405)
	100-1650	QP3	525(575)	455(505)	405(455)
	100-1650	QP4	475(525)	405(455)	355(405)
	100-1650	QP5	510(560)	440(450)	390(440)
	100-1650	QP6	480(530)	410(460)	360(410)

Table 5.7: Concrete shield thicknesses for RFc+acceleration and decay losses.

5.9, where the cathode and the blade together with the two beam pipes can be seen. For decay and RF-acceleration losses an arc segment is represented with a quadrupole and two dipoles (Figure 5.10). They have a simplified cylindrical geometry. The return-yoke composition for all magnets is a compound of iron (98%), silicon (1.5%), manganese (0.2%), aluminum

(0.2%) phosphorus (0.05%), carbon (0.001%) and sulfur (0.0005%). The beam pipe, 0.3 mm in thickness, is in stainless steel with a 0.11% of cobalt. Such thin thickness is necessary because of the eddy currents. It has an elliptical cross section in dipoles and a circular cross section in quadrupoles. Because the RCS tunnel has not yet been designed, a standard arrangement is chosen, with 6 m width and 4.2 m height. The tunnel wall is represented by a concrete layer. Power cables and water pipes are placed close to the magnets and on the lateral wall for prediction of all material activation.

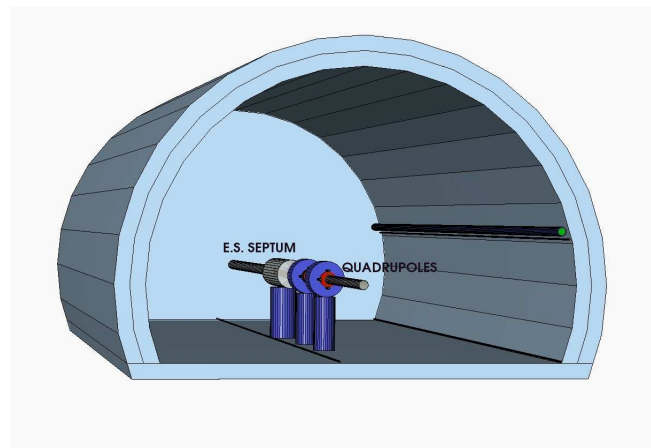


Figure 5.8: 3D visualisation of the geometry of the injection area.

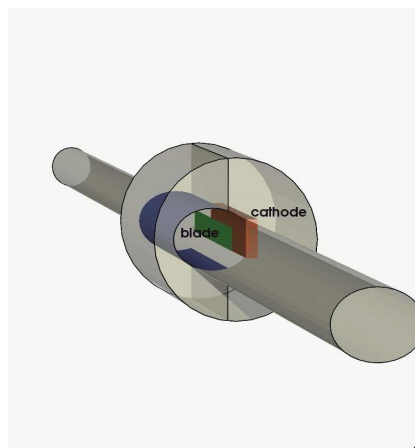


Figure 5.9: 3D visualisation of the geometry of the electrostatic septum.

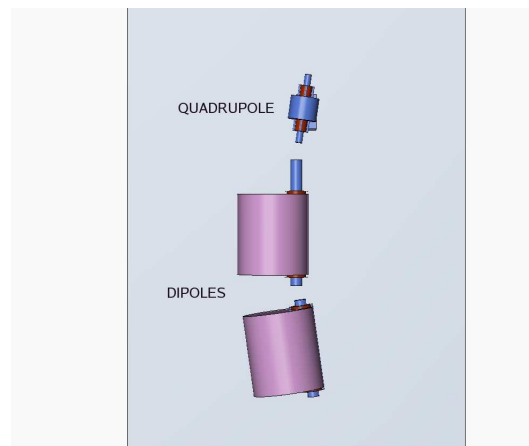


Figure 5.10: 3D visualisation of the geometry of an arc section (top-view).

5.3.1 Air activation

5.3.1.1 Dose to the reference population

The one-year activity of the radionuclides produced in the tunnel and transported to the release stack is calculated, assuming that the RCS stack coincides with the one of ISOLDE, and then converted, through the previously calculated coefficients [77], to effective dose. The choice of the ISOLDE coefficients arises from the possible location of the RCS in Swiss territory. For the continuous releases through the ventilation outlets during the machine operation, a constant ventilation rate is considered. The yields of radioactive nuclides produced in the air of the RCS tunnel are obtained by folding the particle (n , p , π^+ , π^-) track-length spectra, calculated with FLUKA, with isotope production cross-sections (see Chapter 4). Concerning operation, an irradiation time of 10^7 seconds per year is taken and the laminar flow model is used for the activity assessment. The air is driven to the stack without turbulence and at a constant speed. Using $F = 10000 \text{ m}^3 \text{ h}^{-1}$, $A_{\text{surface}} = 18 \text{ m}^2$, $l = 250 \text{ m}$ and $T_{\text{decay}} = 0$ the total activity released during a one-year operation is nearly 3.85 GBq, which corresponds to an effective dose to the reference population of $0.7 \mu\text{Sv}$. In Figure 5.11 the contributions to the total annual dose from the main radionuclides is shown for the worst-case ion, i.e. ^{18}Ne : excluding ^7Be , they are all short-lived radionuclides, with a half-life between a second and a hour. According to Swiss legislation the total effective dose given to the reference population by all CERN installations should not exceed $10 \mu\text{Sv}$. When considering T_{decay} greater than 0 and a lower ventilation rate, the total dose is further reduced. The results for two different F and T_{decay} are shown in Table 5.8, always for ^{18}Ne . The decay times of 8.1 s and 16.2 s correspond to an exit-duct volume of 22.5 m^3 . This value is chosen considering a depth of 10 m for the tunnel and an exit duct cross section of nearly 2 m^2 : to a volume increase would correspond a decrease in the released activity.

F (m^3h^{-1})	T_{decay} (s)	Total Annual Effective Dose(μSv)
5000	0	0.453
5000	16.2	0.447
10000	0	0.679
10000	8.1	0.676

Table 5.8: Annual effective dose given to the reference population for several combinations of F and T_{decay} .

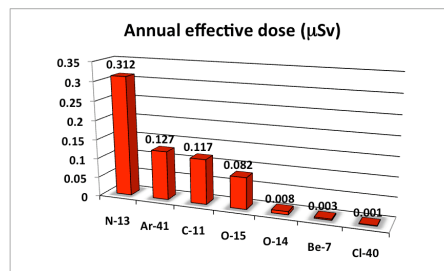


Figure 5.11: Annual effective dose to the reference population: contributions from the main radionuclides.

5.3.1.2 Inhalation dose and external exposure to activated air for workers

The inhalation dose to workers under normal conditions would be negligible because the radioactive air is removed by the ventilation system before access. In this section the dose is calculated for the case of failure of the ventilation system. Several scenarios are considered for irradiation and waiting times, while a one-hour intervention is assumed. The results are shown in Table 5.9 for ^{18}Ne operation, i.e. the worst case: for the several situations considered, doses are less than $1 \mu\text{Sv}$ in a hour of intervention. Besides inhalation dose, also external exposure to the radiation emitted by the airborne radionuclides must be assessed. The conversion coefficients calculated by Eckerman and Ryman, that can be found in Table III-1 of their work (see Chapter 4), are used to convert the fluence track-length spectra into effective dose. The results for the external exposure of workers to airborne radionuclides are reported in Table 5.9, in the last column, and they are assessed for the same irradiation, waiting and intervention times as for the inhalation dose calculation. The values are much higher than those for inhalation but still under the limit of $10 \mu\text{Sv h}^{-1}$ (maximum ambient dose equivalent rate in simple-controlled areas for controlled-radiation workers), below which no further optimization is required. Furthermore, both inhalation and external exposure doses are negligible with respect to external doses due to the activation of materials in the tunnel (see next section).

t_{irr}	t_{wait}	t_{int}	Inhalation dose (μSv)	External exposure (μSv)
1 hour	0	1 hour	7.87E-2	2.42
1 day	0	1 hour	4.07E-2	5.12
1 week	0	1 hour	9.84E-2	5.12
1 month	0 hour	1 hour	4.11E-1	5.13
1 month	1 hour	1 hour	3.92E-1	2.71
3 months	0 hour	1 hour	4.34E-1	5.14
3 months	1 hour	1 hour	4.15E-1	2.72

Table 5.9: Inhalation and external-exposure dose to workers for several irradiation and waiting times, coming from induced activity in the air.

5.3.2 Residual Doses

The beta-beam complex will be operated for three months per year. In order to assess the residual ambient dose equivalent rates during the shutdown or maintenance periods, three waiting times of one hour, one day and one week are chosen. The yields of radionuclides produced in all the materials are calculated, with their specific activities and the consequent residual doses are then assessed for the several waiting times. The three loss scenarios are considered: injection losses in the electrostatic septum area, decay losses in the arcs and RfC-acceleration losses in the families of quadrupoles in the arcs. In Figure 5.12, the dose rate profiles, for ^{18}Ne operation, at the septum, for the three waiting times are given as a function of the distance from the beam-line.

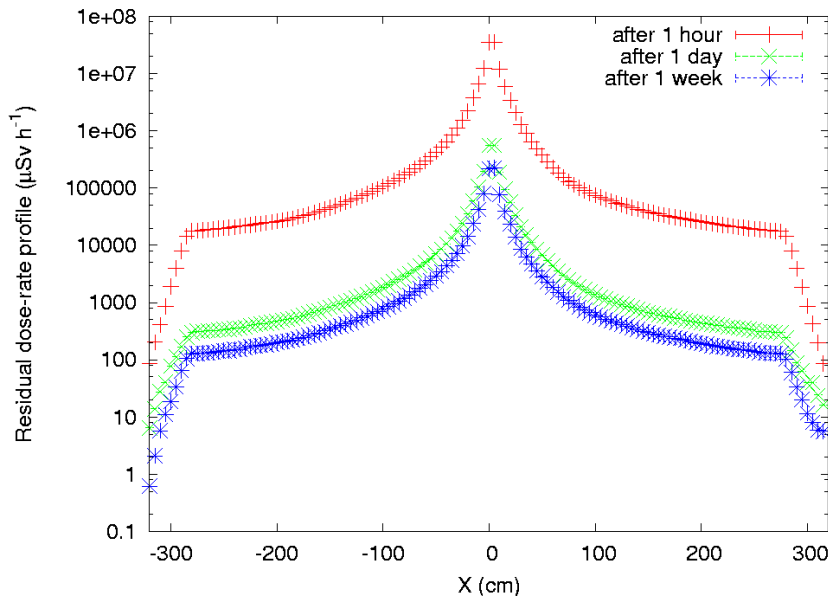


Figure 5.12: Residual dose rate profile near the septum as a function of the distance from the beam line, for the 3 waiting times, for ^{18}Ne .

There is a considerable difference between 1 hour and 1 day of waiting time, but after 1 week the residual dose rate does not change much, especially near the machine components. This is due to the fact that in the first 24 hours most of the short-lived nuclides (^{24}Na , ^{61}Cu , ^{60}Cu , ^{56}Mn), which largely contribute to the total dose, rapidly decay; the most relevant nuclides, left after 1 week, are ^7Be , ^{47}Ca , ^{55}Co , ^{56}Co , ^{51}Cr , ^{52}Mn , ^{54}Mn , ^{57}Ni , ^{44}Sc , ^{48}V . In Figure 5.13 some of the radionuclides, produced in the beam pipe in the septum, with the highest specific activities and characterized by high-energy gamma emissions are summarized. The data points indicate the specific activities after one hour, one day and one week from the shutdown, while the dashed lines indicate the exponential decay curves. From these curves it is possible to deduce the specific activity of the radionuclides at a given time. The value at $t = 0$ corresponds to the initial specific activity of the radionuclide. Among the short-lived radionuclides produced

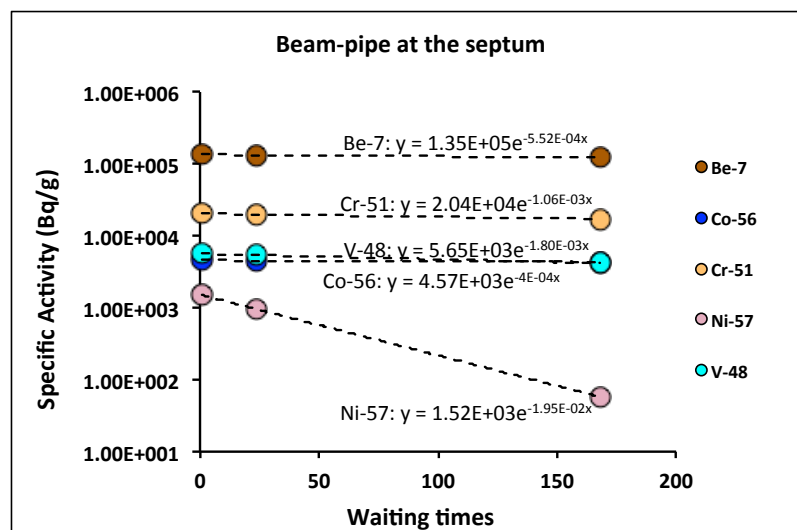


Figure 5.13: Specific activities (Bq/g) for some radionuclides produced in the beam pipe at the septum, given for the three waiting times (^{18}Ne operation).

in the beam pipe, ^{18}F must be mentioned, as it has the highest specific activity after 1 hour in the beam pipe, corresponding to 1.97 MBq/g. Since its half-life is of nearly 110 minutes, it decreases rapidly, down to a hundred Bq/g after one day. In Figures 5.14, 5.15, 5.16, the specific activities of the residual radionuclides produced in the quadrupoles in the arcs are presented for the three waiting times, for ^{18}Ne operation. The specific activities are given for the radionuclides produced in the coils, in the pipe and in the yoke.

In the coils, ^{64}Cu has the highest specific activity: 3.54 MBq/g after one hour. In a week its value decreases to 390 Bq/g, as its half-life is of 12 hours. The same behavior is followed by ^{24}Na with an activity decrease of 99%. Other radionuclides, like ^{59}Fe , ^{56}Co , ^{57}Co , ^{58}Co , ^{54}Mn and ^{59}Fe keep an almost constant high specific activity, due to their long half-lives. ^{22}Na activity remains also constant but with an initial much lower intensity, of the order of 100 Bq/g. In the quadrupole yokes, which are made for 98% of iron, besides $^{n>55}\text{Co}$, ^{59}Fe and

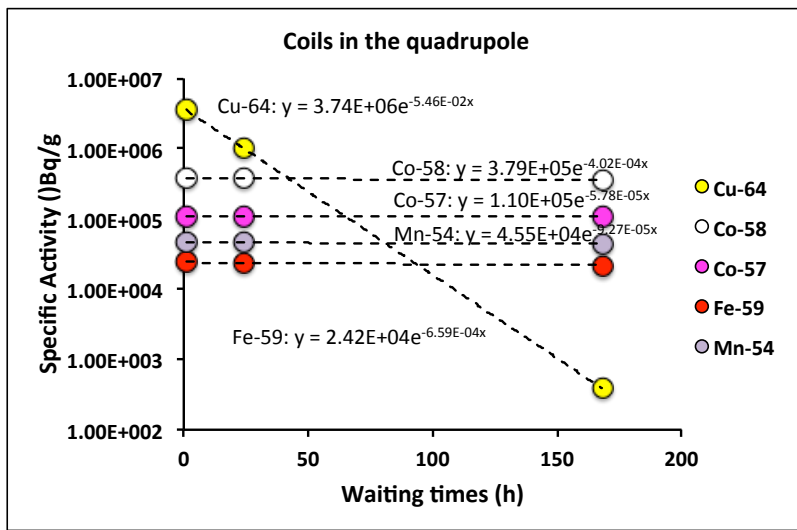


Figure 5.14: Specific activities in Bq/g for some radionuclides produced in the coils in the quadrupole, given for the three waiting times (^{18}Ne operation).

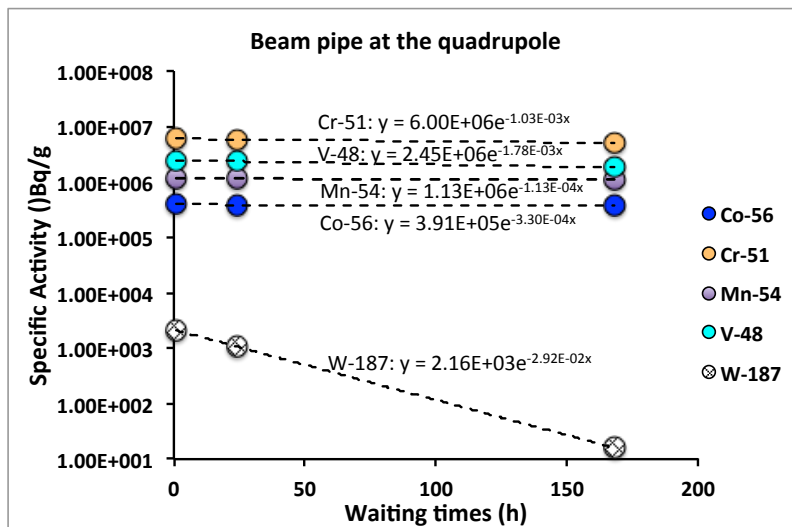


Figure 5.15: Specific activities in Bq/g for some radionuclides produced in the beam-pipe inside the quadrupole, given for the three waiting times (^{18}Ne operation).

^{54}Mn , ^{48}V also presents a specific activity which persists in time, with an initial value of 40 kBq/g. Among the shorter-lived nuclides, ^{48}Cr and ^{55}Co decrease down to a specific activity of few Bq. Specific activities are in general higher in the coils than in the yoke, but the maximum values are attained in the beam pipe, where the beam is lost and makes the first interactions. With respect to yokes and coils, in the beam pipe also ^7Be , ^{48}Sc and ^{187}W are produced. ^{51}Cr presents the highest specific activity of nearly 6 MBq/g.

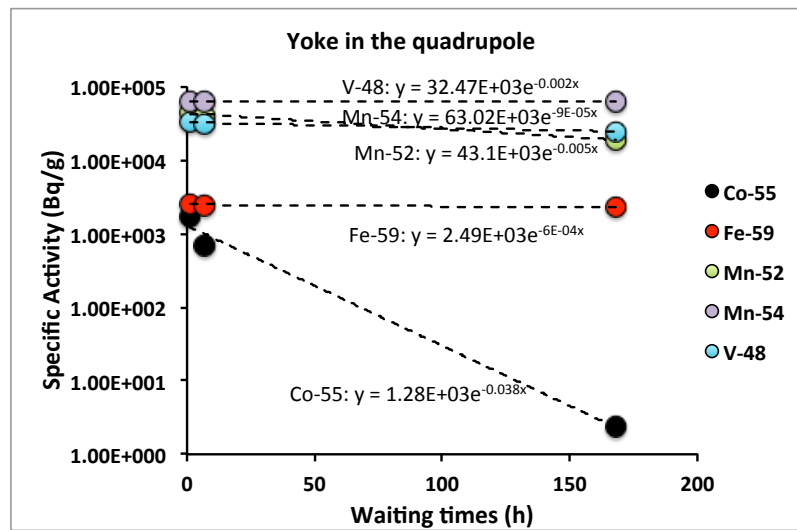


Figure 5.16: Specific activities in Bq/g for some radionuclides produced in the yoke in the quadrupole, given for the three waiting times (^{18}Ne operation).

In Appendix A, the residual dose-rate maps at the several locations where losses occur, for the three-month irradiation and the waiting times of one hour, one day and one week, for both ions, are shown. In Table 5.10 a summary of the values on the maps is presented. The values for dipoles are given with a range, as there are two dipoles in the considered section. Considering only the values after one week, in the septum area the worst case is represented by ^6He operation, which causes a residual dose rate of 6 mSv h^{-1} at a distance of 1 m from the beam-line axis. Losses at the septum blade are indeed higher for helium than for neon, i.e. $2.58\text{E}12$ particles per second for the former and $0.87\text{E}12$ particles per second for the latter. After one hour though, the induced activity in the septum components is higher with neon, due to high specific activity of ^{18}F which is the daughter nucleus of ^{18}Ne and therefore abundantly produced. Its specific activity rapidly decays in few hours. According to the reference dose rates and the classification of areas and personnel, the RCS tunnel could be classified as a limited stay controlled area, accessible after 1 week. As the activity in the tunnel close to the machine elements remains high even after one-week waiting, a remote-handling system may be considered for the maintenance.

^{18}Ne : residual dose rates at 1 m from the loss points (mSv h^{-1})			
t_{wait}	Septum	Quadrupoles	Dipoles
1 hour	60	25	7 ÷ 20
1 day	1.5	8	2 ÷ 6
1 week	0.5	6	1 ÷ 2.5

Table 5.10: Residual dose rates at 1 m from the loss points (mSv h^{-1}) for ^{18}Ne operation.

⁶ He: residual dose rates at 1 m from the loss points (mSv h ⁻¹)			
<i>t_{wait}</i>	Septum	Quadrupoles	Dipoles
1 hour	30	20	4 ÷ 15
1 day	10	5	0.8 ÷ 4
1 week	6	3	0.3 ÷ 2.5

Table 5.11: Residual dose rates at 1 m from the loss points (mSv h⁻¹) for ⁶He operation.

5.3.3 Possible countermeasures to high residual doses

The high residual dose rates represent a concern in terms of radiation protection but also in terms of machine costs. This issue could be overcome by changing the optics of the ring in order to decrease the losses in the families of quadrupoles in the arcs, which cause the activation of the machine components. A study addressed to this problem was started immediately after the first radiation protection results for residual doses during maintenance [78]. It aims at reducing acceleration losses, which represent 10-15% of the beam for both ions, by changing the time structure of the beam at injection. Decay losses would not be reduced by this countermeasure but they only represent a small fraction of all losses. Acceleration losses are due to those particles which are outside the bucket and therefore do not have a stable longitudinal motion [74]: they move away from the stable orbit and hit the vacuum chamber. In the proposed new scenario the injected beam would have a shorter time structure that aims at avoiding particles close to fix points in the longitudinal phase space. This result could be achieved with a beam chopper at low energy, upstream the LINAC, which would cut the beam at injection. In this scenario only decay losses would affect the magnets in the arcs by induced activity and the maximum residual dose rate after one week would be of 1 mSv h⁻¹, as shown in Figure 5.17. This countermeasure has also a drawback: while improving the efficiency in acceleration, it would diminish the injection efficiency. In fact 28% of the beam would be lost before injection. This would have consequences: the ion source should deliver a 28% longer pulse with the same intensity or a shorter pulse with a 28% higher intensity. In the former scenario, the efficiency of the multi-turn injection will be decreased but the losses will be localized at lower energy and therefore it represents a preferable solution from the point of view of radiation protection.

5.4 Summary and conclusions

The areas around the RCS tunnel will be classified as supervised radiation areas during operation, with a maximum ambient dose equivalent rate of 3 μSv h⁻¹: the respect of this value would require concrete shielding thicknesses ranging from 3 to 5 m, depending on the position in the tunnel. In those places where different kinds of losses occur, the thickness imposed by the dominating mechanism is considered.

In the released airborne activity study a constant rate of 10000 m³ h⁻¹ is chosen for the

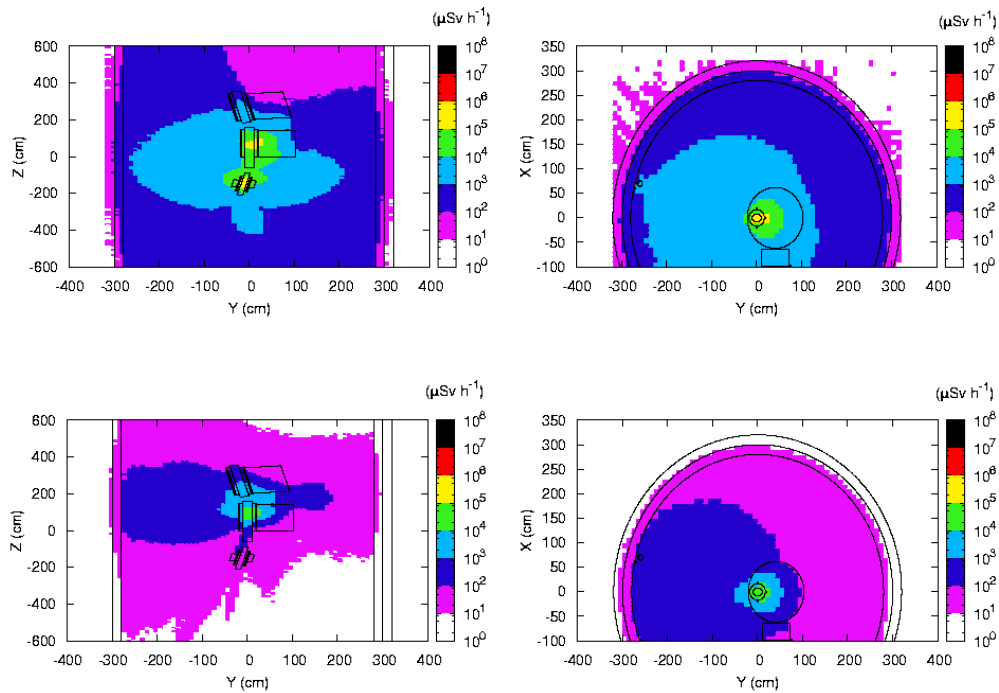


Figure 5.17: Top: Residual dose rate after one week with both RfC-acceleration and decay losses. Bottom: Residual dose rate after one week with decay losses only.

ventilation system in the RCS tunnel. The effective dose given to the reference population in one year of operation is below the reference value for CERN emission and could be further decreased by enlarging the ventilation outlet dimensions. For the inhalation dose to workers that could access the tunnel during shutdown periods a conservative assumption is made: the ventilation system is not operating. The intervention time depends on dose rates and on whether or not the ventilation system is on. For a 1-hour intervention the integrated dose does not exceed the constraints, even without any waiting time. Furthermore, if the ventilation system is working a waiting time before access of nearly 20 minutes is enough to completely change the air in the tunnel. The external exposure to activated air determines dose rates for the workers which range between 2 and 6 $\mu\text{Sv h}^{-1}$. These values, much higher than those for inhalation, are negligible if compared with the doses arising from the material activation. Indeed the results for the residual doses, calculated for a 3-month continuous operation and three different waiting times, show that, one hour after the shutdown, the dose rate varies from 4 to 60 mSv h^{-1} . After a week, the rates are of nearly 0.3 to 6 mSv h^{-1} . According to CERN area classification, the RCS tunnel is likely to be classified as a limited stay area, accessible 1 week after the shutdown. The doses do not decrease much after one week because the residual radionuclides that mostly contribute to the total dose have half-lives longer than one week. The high activation of the machine elements that remains after one week may require a remote handling system for the maintenance. In order to reduce the residual dose rates during the

Chapter 5. The Rapid Cycling Synchrotron (RCS)

maintenance of the machine, mainly caused by losses in the families of quadrupoles in the arcs by means of RF capture and acceleration, changes in the machine optics were explored. In the new scenario, losses in quadrupoles would be only due to particle decays and would give rise to dose rates of 1 mSv h^{-1} one week after the shutdown.

6 The Proton Synchrotron (PS)

The Proton Synchrotron (PS) is one of the oldest accelerators built at CERN which are still operating. In Figure 6.1, the PS complex is shown: it comprises the injection LINAC (II and III), the ion accumulator LEIR, the booster and finally the PS. Presently, part of this complex represents the injection chain for the Large Hadron Collider (LHC). With a circumference of

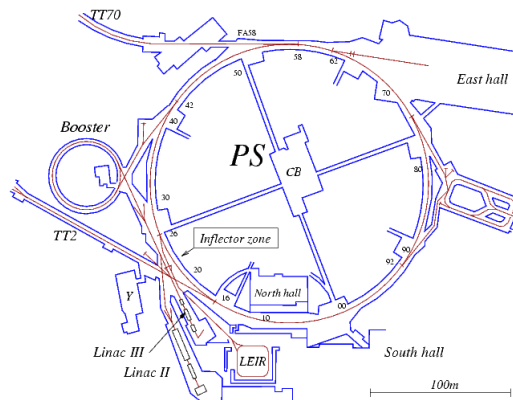


Figure 6.1: The PS complex (from CERN PS webpage).

628 m (100 m diameter) (see Table 6.1 for some parameters), the PS will accelerate ${}^6\text{He}$ ions up to 7.757 GeV/u and ${}^{18}\text{Ne}$ ions up to 13.5 GeV/u within the beta-beam project. As reported in

Circumference	628.3 m
Physical radius	100 m
Injection energy	787 MeV/u - 1.65 GeV/u
Maximum magnetic rigidity	86.93 T·m

Table 6.1: Main parameters of the ring within beta beams.

Chapter 2, nearly $1.1\text{E}13$ ${}^6\text{He}$ ions and $4.5\text{E}12$ ${}^{18}\text{Ne}$ ions are injected during a cycle, 64% of ${}^6\text{He}$ ions and 20% of ${}^{18}\text{Ne}$ ions are then lost by decay in a cycle, in the bending areas. The PS has

277 electromagnets, including 100 bending dipoles; the arcs consist of a regular cell structure composed by three magnets. One of the main issues related to the use of the existing PS in the beta-beam accelerator chain is represented by the survival of the magnets to the high power deposited on the coils. Studies on the energy deposition in the coils of the bending magnets were performed at GSI and the results show that the survival time of the actual coils would reach nearly 36 years [79], without considering the precedent irradiation, for the nominal beta-beam operation of 10^7 s per year. From the point of view of radiation protection, the activation of the magnets must be investigated: indeed residual dose rates near the magnets can affect the access to the accelerator for maintenance or other kinds of intervention.

6.1 Beam losses

Decay losses will play a major role for PS and were calculated in a previous study [80]. It has been estimated that 1.17×10^{12} ${}^6\text{He}$ ions are lost in one second in the entire machine and 2.88×10^{10} in one cell (three magnets). In the ${}^{18}\text{Ne}$ case, 2.4×10^{11} ions are lost in one second in the entire machine, 6.08×10^9 in one cell. In Figure 6.2 the decay losses, calculated with the Strahlsim code, developed at GSI [81], are shown for both the ions in a characteristic cell of the PS, at injection energy. These losses present a characteristic pattern: they have a high peak in between the magnets and they are uniformly distributed all along the magnets in the case of ${}^6\text{He}$, while in the case of ${}^{18}\text{Ne}$ they have high peaks in the drift sections and in the first half of the magnet. In the calculations of the shielding, a point-loss approximation is used in order to take into account the magnets which are likely to be exposed to point losses. In the induced-activity calculations, the beam losses are represented by a linear source located at the surface of the beam pipe on the side near the center of the yoke for ${}^6\text{He}$, and as point losses in the first half of the magnet for ${}^{18}\text{Ne}$. Concentrating losses which in reality are distributed over the whole magnet corresponds to a worst-case scenario in terms of residual dose rate. However, the total production of secondary particles is not affected by this concentration and therefore the shield thickness is not overestimated.

6.2 Shielding calculations

For the shielding thickness evaluation, the calculations are performed at the extraction energy of the machine, namely 13.5 GeV/u for ${}^{18}\text{Ne}$ and 7.5 GeV/u for ${}^6\text{He}$. The source terms and the attenuation lengths in concrete at the injection energies can be found in the previous chapter, as they are calculated for the RCS extraction energies. Losses are concentrated in one point loss with an intensity which is the sum over all the particles lost along the magnet. This assumption is conservative because in the general case losses will be distributed along the magnet. The attenuation curves in concrete for the two ions are shown in Figures 6.3 and 6.4. The results of the fit of these curves via two parameters are summarized in Table 6.2: they are the source term H_0 (Sv m^2 per primary ion) and the attenuation length in concrete λ_0 (g cm^{-2}). Thanks to extensive MC simulations, the statistical uncertainty of these parameters was taken

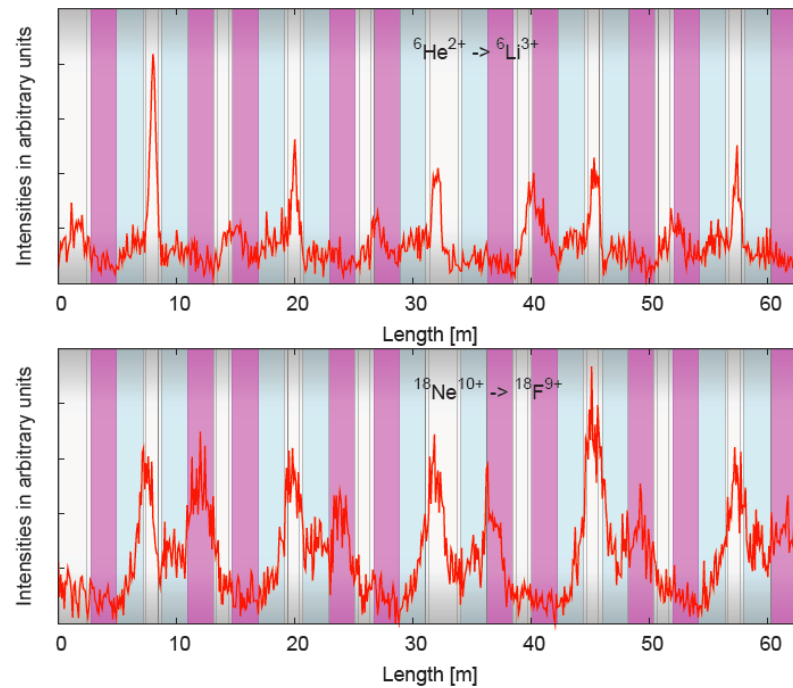


Figure 6.2: Decay losses in the PS, calculated via the Strahlsim code [81], for ${}^6\text{He}$ (top) and ${}^{18}\text{Ne}$ (bottom), at injection energy. The magnets are indicated in blue/magenta [24].

down to less than 1% in spite of considerable thickness (5 m) of the shielding simulated. The attenuation lengths in concrete for helium and neon do not differ much from each other and the thickness of concrete in the bending sections of the PS, calculated for the three possible classifications for the areas at CERN, ranges from 250 to 360 cm, taking into account an extra attenuation length as safety margin.

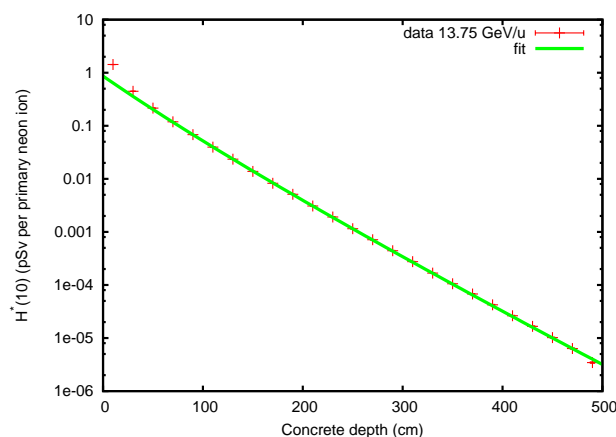


Figure 6.3: Attenuation curves in concrete for neon at the extraction energy of the PS.

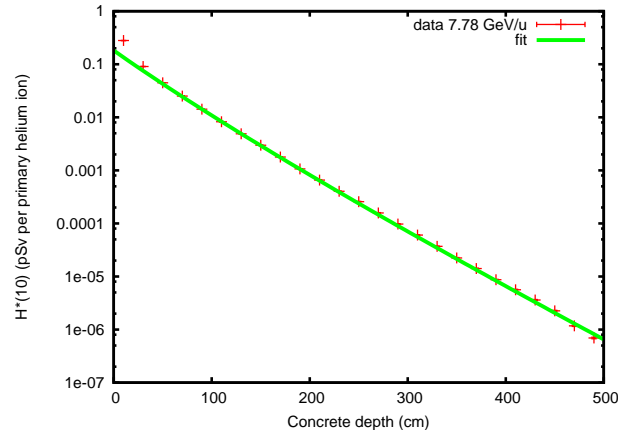


Figure 6.4: Attenuation curves in concrete for helium at the extraction energy of the PS.

Table 6.2: Source terms H_0 (Sv m² per primary ion) and attenuation lengths λ_θ in concrete (g cm⁻²) for ¹⁸Ne and ⁶He at the extraction energies.

	Neon		Helium	
	Fit results	% Error	Fit results	% Error
H_0	$(3.5 \pm 0.05)E-12$	0.05%	$(0.7 \pm 0.006)E-12$	0.85%
λ_θ	117.39 ± 0.36	0.31%	116.6 ± 0.5	0.41%

Decay losses (⁶ He, ¹⁸ Ne) at nominal intensity:				
		Dose equiv. rate $\mu\text{Sv h}^{-1}$		
		0.5	3	10
ion	energy (GeV/u)	Concrete shield thickness (cm)		
⁶ He	0.787-7.5	310 (360)	245 (294)	203 (253)
¹⁸ Ne	1.65-13.5	312 (362)	246 (296)	204 (254)

Table 6.3: Concrete shield thickness for decay losses of ¹⁸Ne and ⁶He. The values in parentheses contain a safety margin.

The small difference between the shielding for the helium case and the neon case can be explained with the higher percentage of decay losses of helium which compensates for the lower energy and for the lower number of nucleons with respect to neon. Following the results for the shielding calculations, the area outside PS could be classified as public area with a 360 cm-thick concrete wall. This value represents the thickness required for the helium operation. As other sources of losses are not known, like, for instance, injection losses, the resulting shielding cannot be estimated. Nevertheless, the results here obtained can be normalized to

the number of particles lost in any position of the machine.

6.3 Induced activity

In the geometry for induced activity calculations, where results are affected by the precision with which materials and masses are represented, one single cell structure has been implemented as representative of the entire arcs. It is composed of three combined-function magnets (both bending and focusing). Figure 6.5 represents the actual PS tunnel cross section in correspondence of a combined-function magnet. The error introduced by disregarding the tunnel curvature in FLUKA geometry reduces to a sagitta of 28 cm over 18 m. This error is negligible because it affects the radiation environment far away from the beam loss points. The girder for the magnet is also reproduced with precision both in terms of shape and material composition. The FLUKA geometry of the combined-function magnet is shown in Figure 6.6.

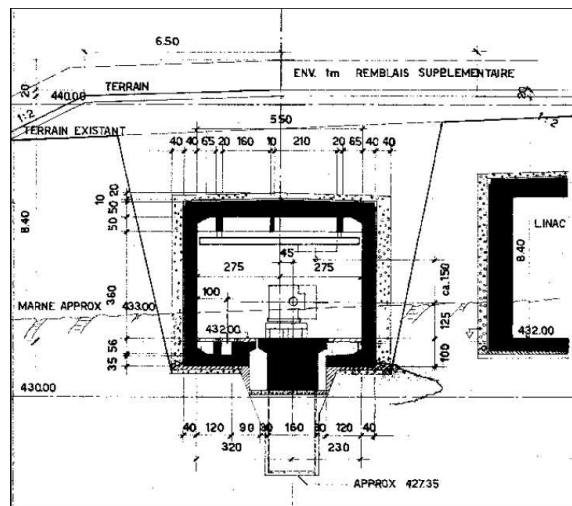


Figure 6.5: The PS tunnel section (original drawing).

The return yoke is C-shaped and has polar expansions in proximity of the coils. The coils are pancake coils in copper. Each magnet is 427 cm long and connected to the next one by a 160 cm-long beam pipe. The cell structure is therefore nearly 18 m in length. The simulated section of the tunnel actually extends over several meters before and after the cell structure, in order to include the backscattering of neutrons from the walls. The chemical compositions of all the components are taken from the specifications of the combined-function magnets in the PS and are expressed, for each element, as mass fractions. The vacuum pipe, made in stainless steel, with a density of 7.62 g cm^{-3} , has the following chemical composition, where the values in parentheses represent the mass fractions: Fe (70.3), Cr (17.3), Ni (11.4), Si (5.2E-1), Ti (3.55E-1), S (1.78E-2), P (2.58E-3) and C (1.48E-5). The steel supports ($\rho = 8 \text{ g cm}^{-3}$) are composed by Fe (62.823), Cr (18), Mn (11.6), Ni (6.7), Si (3.9E-1), Co (1.1E-1), C (9.4E-2), Cu (8E-2), Mo (8E-2), V (7E-2), P (2.2E-2), Nb (1E-2), Ti (1E-2) and W (1E-2). The coils are made of copper

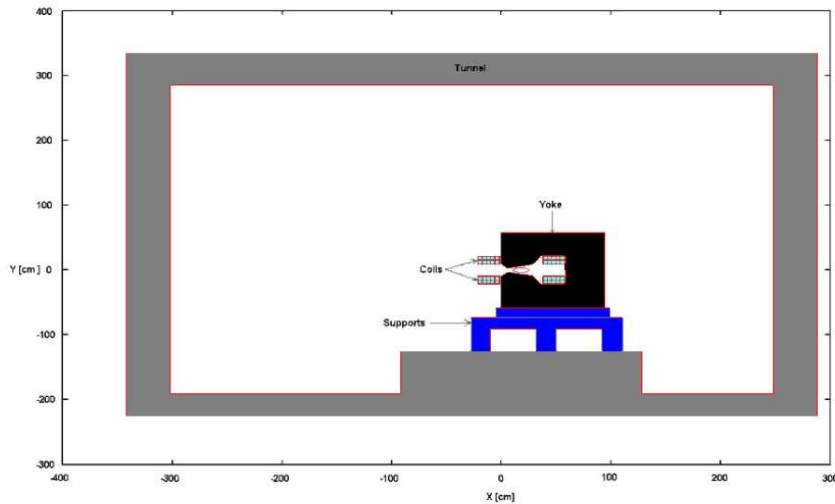


Figure 6.6: Cross section of a combined-function magnet in the PS tunnel, as it is represented in the FLUKA simulations.

with density equal to 8.96 g cm^{-3} and have been implemented with the water cooling system. The tunnel walls are made of concrete with density equal to 2.35 g cm^{-3} , with the following chemical composition: O (49.288), Ca (20.091), Si (18.867), C (5.621), Al (2.063), Fe (1.118), Mg ($6.63\text{E-}1$), K ($6.56\text{E-}1$), H ($6\text{E-}1$), Na ($4.53\text{E-}1$), Sr ($3.99\text{E-}1$), Ti ($3.47\text{E-}1$), P ($4.8\text{E-}2$), Pb ($4.64\text{E-}2$), Mn ($3.87\text{E-}2$), Zn ($2.41\text{E-}2$), Ba ($1.79\text{E-}2$), S ($1.2\text{E-}2$), Zr ($7.4 \text{E-}3$) and Eu ($5\text{E-}5$). The induced activity is estimated in the machine elements and in the air for the annual operation of beta beams, for both the primary ions. The considered waiting times are one hour, one day and one week.

6.3.1 Air activation

In Figure 6.7 and in Figure 6.8 the characteristic lethargy spectra for secondary protons, pions and neutrons produced in the air are shown. Lethargy is a function of the particle energy as it slows down and the lethargy spectra are particle fluence spectra per unit logarithmic energy ($\frac{d\Lambda}{d(\text{Log}E)}$). Neutrons represent the most relevant component of the integral spectra of produced secondary particles and, at high energy, they arise from quasi-elastic interactions of secondary protons. The number of neutrons produced is higher for neon ions, with respect to helium ions, due to the higher number of nucleons of neon.

6.3.1.1 Dose to the reference population

For the assessment of the airborne activity, released from the stacks into the environment, the following assumptions are considered: the machine is operated continuously for one year, i.e.

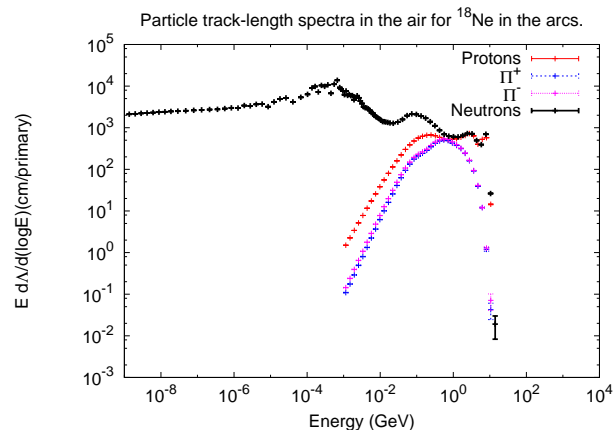


Figure 6.7: Characteristic lethargic spectra for secondary protons, pions and neutrons produced in the air by ${}^6\text{He}$.

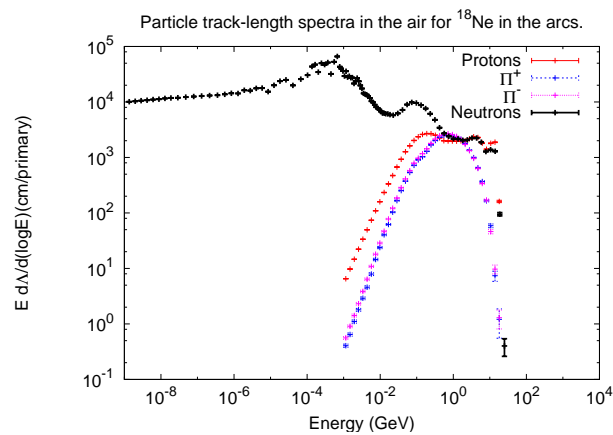


Figure 6.8: Characteristic lethargic spectra for secondary protons, pions and neutrons produced in the air by ${}^{18}\text{Ne}$.

1E7 seconds; the ventilation rate in the tunnel corresponds to $F=4E4 \text{ m}^3 \text{ h}^{-1}$ and the air is released through one stack. The volume of irradiated air is $V=7892 \text{ m}^3$ and 10^{19} helium ions are assumed to be lost in a year. The reference population is the same as for the RCS, namely for ISOLDE. These assumptions are made considering the position of the PS on CERN site and on ventilation parameters of the actual PS. Based on the model described in Chapter 4, the track-length spectra of the secondary particles are convoluted with the radionuclide production cross-sections in order to evaluate the yields of each radionuclide and the analytical model is used for the diffusion through the tunnel and the stack. Tables 6.4 and 6.5 summarize the radionuclides produced in the air which mostly contribute to the released activity. For each radionuclide the single contribution to the total annual effective dose is given. The total annual effective dose delivered to the reference population during ${}^6\text{He}$ operation is of 0.2

Chapter 6. The Proton Synchrotron (PS)

μSv . In the neon case, in the same conditions for ventilation parameters for an annual loss of

Radionuclides	Annual effective dose
^{13}N	0.084 μSv
^{11}C	0.041 μSv
^{15}O	0.040 μSv
^{41}Ar	0.008 μSv
^{14}O	0.006 μSv
^{39}Cl	0.002 μSv
^{35}P	0.002 μSv
^{38}Cl	0.001 μSv
^7Be	0.001 μSv
^{40}Cl	0.001 μSv
^{37}S	0.001 μSv

Table 6.4: Contribution to the total annual effective dose of the most relevant radionuclides produced by air activation in the PS tunnel during a one-year ^6He operation and released into the environment.

nearly 10^{18} ions, the total annual effective dose to the reference population is of 0.7 μSv . In

Radionuclides	Annual effective dose
^{13}N	0.157 μSv
^{11}C	0.152 μSv
^{15}O	0.040 μSv
^{41}Ar	0.032 μSv
^{14}O	0.021 μSv
^{39}Cl	0.008 μSv
^{35}P	0.007 μSv
^{38}Cl	0.005 μSv
^7Be	0.004 μSv
^{40}Cl	0.003 μSv
^{37}S	0.002 μSv

Table 6.5: Contribution to the total annual effective dose of the most relevant radionuclides produced by air activation in the PS tunnel during a one-year ^{18}Ne operation and released into the environment.

Figure 6.9 a comparison between the individual contribution of each radionuclide to the total dose for the two ions is shown. In both cases the highest dose comes from the shortest-lived radionuclides, such as ^{13}N , ^{11}C and ^{15}O . The ratio between the values for helium and neon is not constant, as expected. The yield of a certain radionuclide depends on the loss intensity, on the number of nucleons involved in the nuclear reaction that produces it and on the energy of the primary particle. Some of the produced radionuclides can be filtered, like ^7Be and do not represent an issue in terms of mitigation. Other radionuclides, which are in the form of

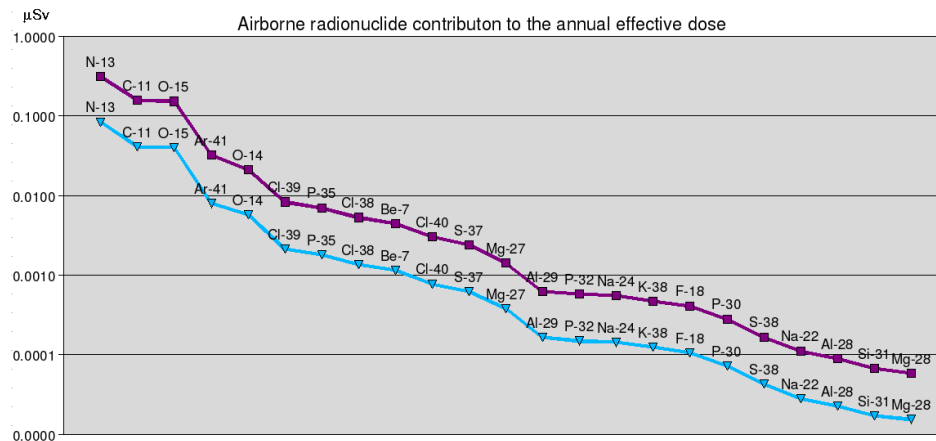


Figure 6.9: Contribution of airborne radionuclides to the total annual effective dose given to the reference population: comparison between the radionuclides produced by ¹⁸Ne (purple) and by ⁶He (blue).

aerosols, cannot be filtered and must be monitored if produced in high quantities. In the case of PS, the calculations show that this risk is not present.

6.3.1.2 Inhalation dose and external exposure to activated air for workers

Following the analytical methods explained in Chapter 4, the inhalation dose and the external exposure to the activated air for workers in the PS tunnel are calculated for several scenarios of intervention, in the hypothesis of ventilation failure. The results are summarized in Table 6.6. Both inhalation dose and external exposure values are close to the ones found for the workers

t_{irr}	t_{wait}	t_{int}	Inhalation dose (μSv)	External exposure (μSv)
1 hour	0	1 hour	4.38E-2	1.35
1 day	0	1 hour	2.27E-2	2.85
1 week	0	1 hour	5.48E-2	2.85
1 month	0	1 hour	2.29E-1	2.86
1 month	1 hour	1 hour	2.18E-1	1.51
3 months	0	1 hour	2.42E-1	2.86
3 months	1 hour	1 hour	2.31E-1	1.52

Table 6.6: Inhalation and external-exposure dose to workers for several irradiation and waiting times, coming from induced activity in the air.

in the RCS. This is not unexpected as, even if the energy of the secondary particles from which the radionuclides are produced in the air in the PS is higher than in the RCS, nevertheless the loss intensities are smaller and the volume of air is larger. In fact, the PS tunnel is nearly 3 times longer than the RCS one and the loss intensity in the RCS is 10 times higher than in the

PS. All the values are under the limit of $10 \mu\text{Sv h}^{-1}$.

6.3.2 Residual Doses

The residual dose rates in the PS tunnel, arising from a year irradiation, followed by several waiting times, are calculated and compared to the survey measurements collected from 2009 to 2012, period in which the PS was operated also as an injector for the LHC [82, 83]. The dose rate maps calculated for the PS in beta beams are presented in Figures 6.10, 6.11 and 6.12 for the helium case. In Figure 6.13 the dose rate profile at the main loss point in the section is shown for the three waiting times of 1 hour, 1 day and 1 week. At 40 cm from the beam line, in

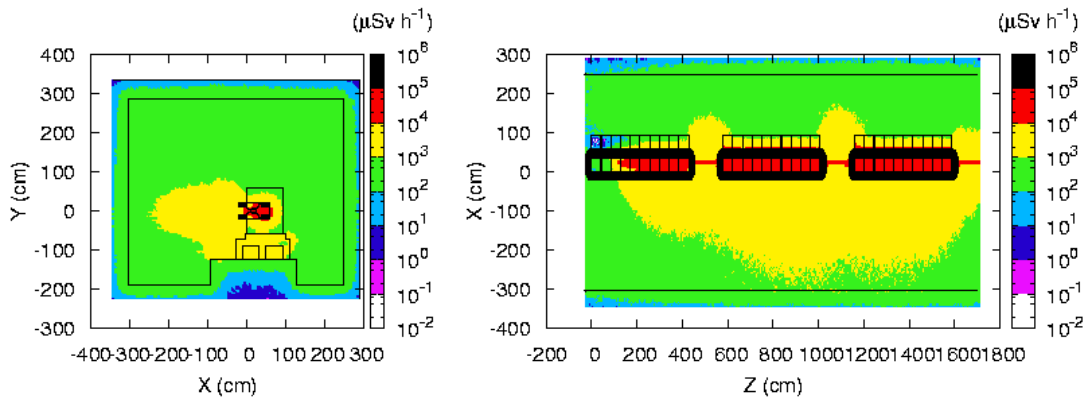


Figure 6.10: Residual dose rate map for ${}^6\text{He}$, one hour after the end of the yearly operation of the PS.

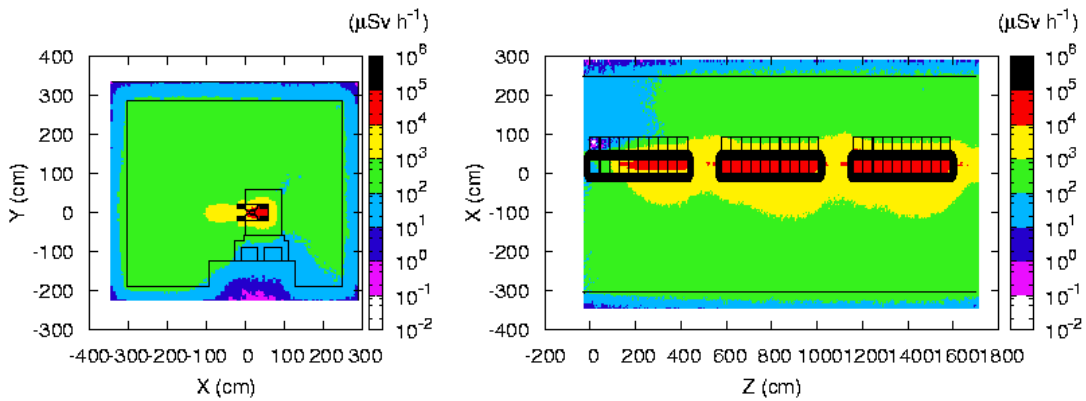


Figure 6.11: Residual dose rate map for ${}^6\text{He}$, one day after the end of the yearly operation of the PS.

the main loss point, the residual dose 1 hour after the shutdown is of 4.1 mSv h^{-1} and drops to 1.3 mSv h^{-1} in a week time. 40 cm corresponds to the distance used for the measurements

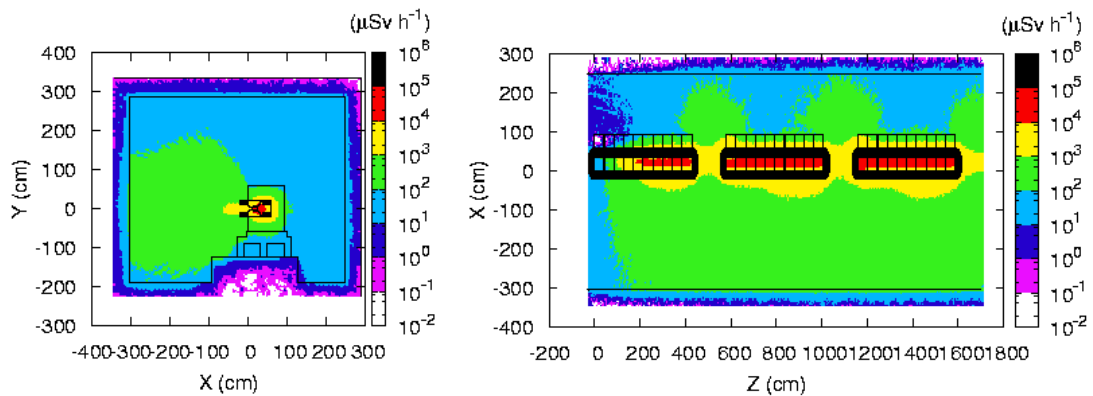


Figure 6.12: Residual dose rate map for ${}^6\text{He}$, one week after the end of the yearly operation of the PS.

performed during the surveys. In Figures 6.14, 6.15 and 6.16, the residual dose rates for the

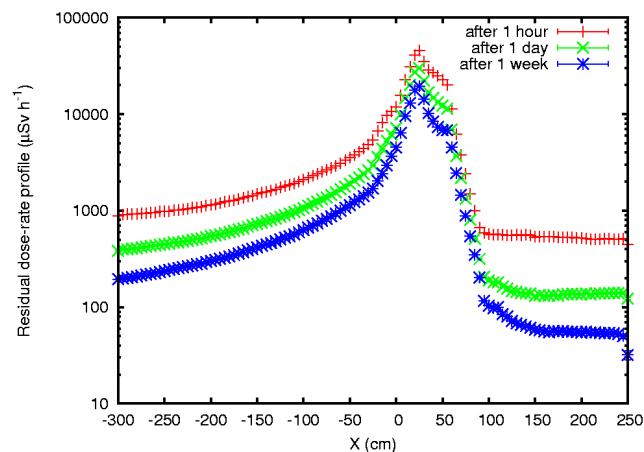


Figure 6.13: Residual dose rate profiles for ${}^6\text{He}$, for three waiting times after the yearly operation of the PS. The profiles are taken at the worst loss point in the magnets.

neon case are presented for the same waiting times as in the helium case. In Figure 6.17 the dose rate profile, for the worst loss point in the dipole, is shown. The values for the residual doses after 1 hour, 1 day, 1 week are 4.3 mSv h^{-1} , 2.3 mSv h^{-1} , 1.4 mSv h^{-1} , respectively, at the worst point. Whilst in the other machines the residual dose rates are higher for the neon operation, in the PS there is no relevant difference between the two operation modes as the loss percentage for the helium is three times bigger than the percentage for neon. The PS surveys from 2009 to 2011 here reported were performed in the beginning of December of each year. the measurement taken in 2012 corresponds to a waiting time of 2 months after the shutdown in the end of 2011. They show the residual dose rates at 40 cm from the beam line in the PS section where the main losses occur, nearly 1 day after the beam shutdown; the

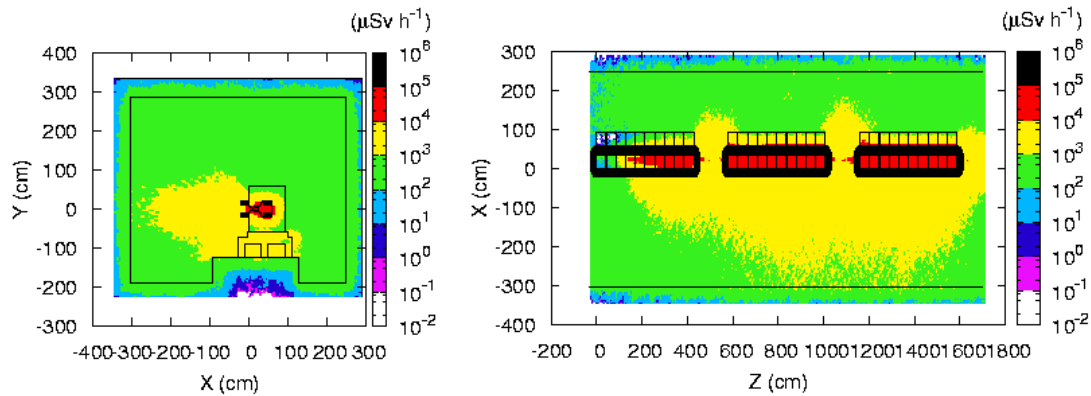


Figure 6.14: Residual dose rate for ^{18}Ne , one hour after the end of the yearly operation of the PS.

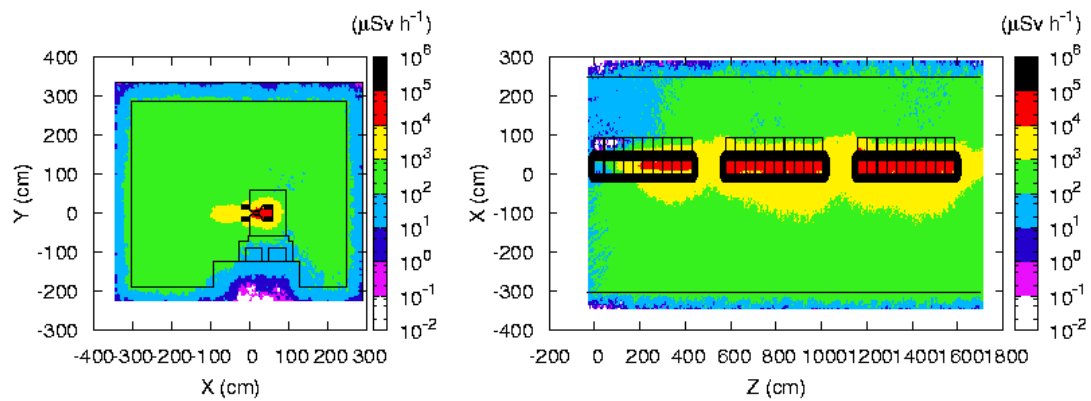


Figure 6.15: Residual dose rate for ^{18}Ne , one day after the end of the yearly operation of the PS.

instrument employed for all measurements is a dose rate meter of type Automess 6150 AD 6. The residual ambient dose equivalent rates were collected in several sections of the machine. The highest doses were recorded in both years in SS16, which is the magnetic septum area [84], where the maximum value in 2009 was 9.9 mSv h^{-1} , 7.8 mSv h^{-1} in 2010, 7.9 mSv h^{-1} in 2011 and 2 mSv h^{-1} in 2012. At the end of each operation year, five sections in the PS were classified as high-radiation areas. The values from the surveys are larger than the values estimated for both helium and neon and for the 3 waiting times in the beta-beam operations. Therefore it is possible to conclude that the induced activity in the PS, from the point of view of the residual dose rates, is not a showstopper for the use of the machine within the beta-beam facility.

The yields of the main radionuclides produced in the machine components are also estimated

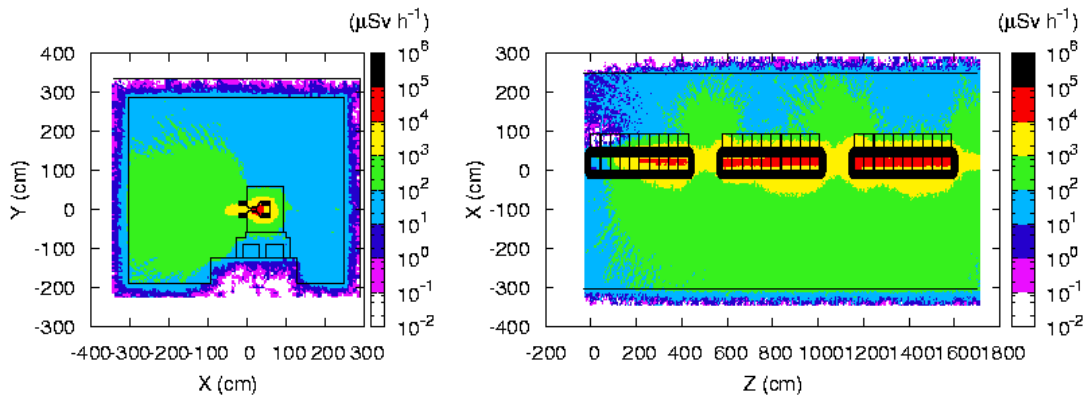


Figure 6.16: Residual dose rate for ^{18}Ne , one week after the end of the yearly operation of the PS.

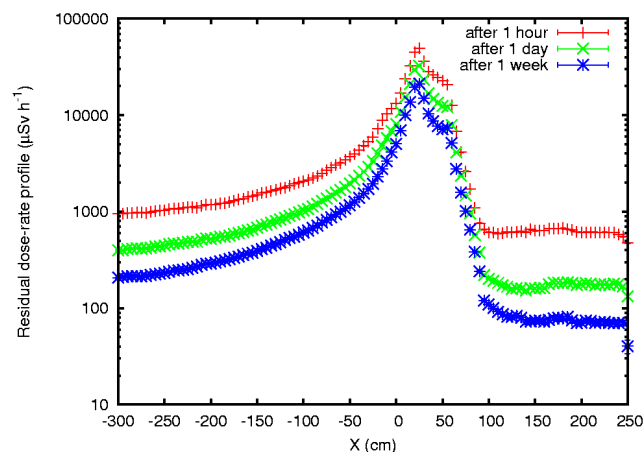


Figure 6.17: Residual dose rate profiles for ^{18}Ne , for three waiting times after the yearly operation of the PS. The profiles are taken at the worst loss point in the magnets.

and their activities are presented for the same waiting times as for the residual doses. In Table 6.7 the total and specific activities of the radionuclides produced in the beam pipe are presented (only those with a total activity higher than 10 MBq). Most of these radionuclides have a long half-life and their concentration, therefore their specific activity, does not decrease significantly in one day. ^{24}Na specific activity reaches low levels after one week, but its production must be monitored as its hydro-solubility represents a risk in terms of contamination of water. In Figure 6.18 the specific activities of some of the radionuclides of Table 6.7 are plotted in overlapping with their decay curve. The plot shows that, known the initial activity, it is possible to predict their specific activity for any waiting time, following the exponential decay law. Furthermore, it is possible to observe that some radionuclides like ^{51}Cr and ^{48}V

Chapter 6. The Proton Synchrotron (PS)

	1 hour		1 day		1 week	
	Activity (Bq)	Spec. Activity (Bq/g)	Activity (Bq)	Spec. Activity (Bq/g)	Activity (Bq)	Spec. Activity (Bq/g)
⁵¹ Cr	1.79E8	1.62E4	1.74E8	1.58E4	1.50E8	1.36E4
⁴⁸ V	1.16E8	1.05E4	1.11E8	1.01E4	8.60E7	7.79E3
⁴⁴ Sc	6.24E7	5.65E3	2.77E7	2.51E3	5.01E6	4.54E2
⁷ Be	5.87E7	5.32E3	5.80E7	5.25E3	5.37E7	4.86E3
⁵² Mn	4.78E7	4.33E3	4.26E7	3.86E3	2.02E7	1.83E3
^{44m} Sc	3.37E7	3.05E3	2.57E7	2.33E3	4.68E6	4.24E2
⁵⁴ Mn	2.83E7	2.56E3	2.83E7	2.56E3	2.79E7	2.53E3
⁴⁹ V	2.83E7	2.56E3	2.83E7	2.56E3	2.79E7	2.53E3
³² P	2.73E7	2.47E3	2.60E7	2.35E3	2.60E7	2.35E3
⁵⁶ Co	1.80E7	1.63E3	1.79E7	1.62E3	1.70E7	1.54E3
⁴⁶ Sc	1.68E7	1.52E3	1.67E7	1.51E3	1.59E7	1.44E3
⁵⁷ Ni	1.67E7	1.51E3	1.07E7	9.69E2	6.47E5	5.86E1
⁴⁷ Sc	1.60E7	1.45E3	1.31E7	1.19E3	3.87E6	3.50E2
³³ P	1.47E7	1.33E3	1.44E7	1.30E3	1.22E7	1.10E3
⁵⁵ Fe	1.31E7	1.19E3	1.31E7	1.19E3	1.31E7	1.19E3
²⁴ Na	1.20E7	1.09E3	4.13E6	3.74E2	5.22E3	4.73E-1

Table 6.7: Total and specific activities of radionuclides produced in the beam pipe by ⁶He, for the waiting times of 1 hour, 1 day and 1 one week. Only the radionuclides with a total activity higher than 10 MBq are listed.

keep a constant activity over one week as they have a half-life of several days. Figure 6.19

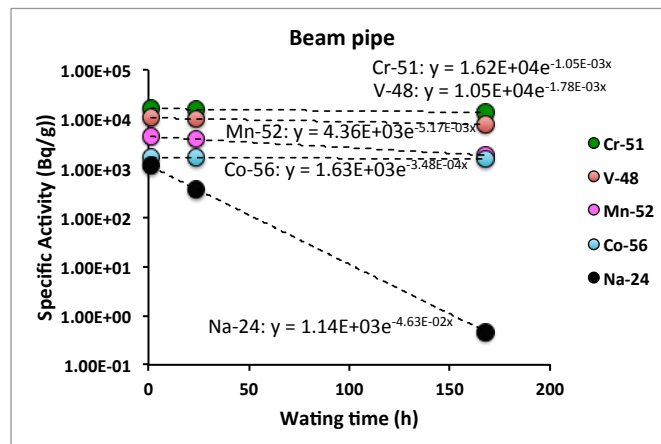


Figure 6.18: Specific activities of radionuclides produced in the beam pipe by ⁶He.

shows a comparison between the specific activities in the C-shaped part of the yoke and in the poles of the bending magnets. The activities are higher in the poles, as expected, since the poles are closer to the beam pipe, where the first interaction with the primary beam loss

occurs. Another comparison is made between the straight and bent parts of the pancake coils.

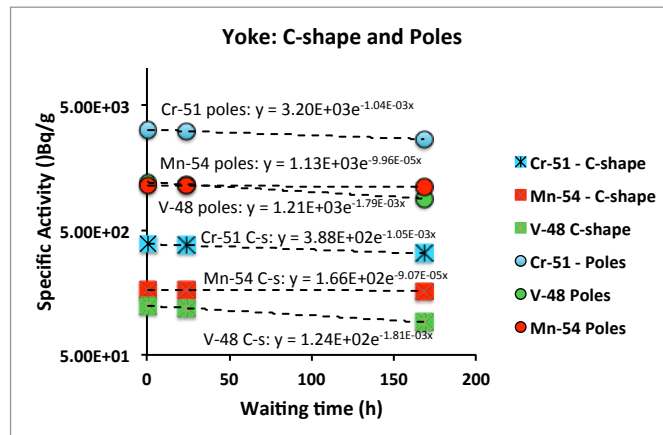


Figure 6.19: Specific activities of radionuclides produced in the yoke by ${}^6\text{He}$: comparison between the C-shaped part and the poles.

In particular, following the naming convention described in Figure 6.20, the straight-right section and the bent-front section of the pancake are analyzed. These two sections are hit by most of the particles lost in the magnet. In the coils, ${}^{61}\text{Cu}$ has the highest activity value which

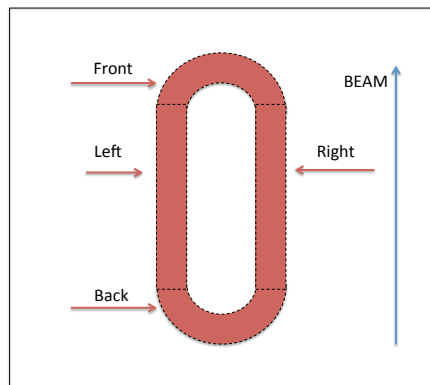


Figure 6.20: Naming convention for the sections of the coils in the induced-activity calculations: “straight” (left and right) and “bent” (front and back).

decreases drastically after few hours, as it has a half-life of nearly 3 hours. Other radionuclides, which are not found in the yoke and in the beam pipe, like ${}^{64}\text{Cu}$, remain longer and are still present after one week. Table 6.8 summarizes the results. A third term of comparison is the Exemption Limit (LE) value, contained in the Swiss legislation for the radioactive waste

disposal: it represents the value of reference for the nuclear waste characterization and reflects the radiological hazard for a given radionuclide. The results show that the specific activities in

	Straight-right section (right)			Front-bent section (front)			LE (Bq g ⁻¹)
	Specific Activity (Bq g ⁻¹)						
	1 hour	1day	1 week	1 hour	1day	1 week	
⁴⁴ Sc	7.29E0	3.24E0	5.85E-1	9.27E0	4.09E0	7.33E-1	30
⁴⁸ V	1.34E1	1.28E1	9.90E0	2.23E1	2.13E1	1.64E1	5
⁵¹ Cr	2.43E1	2.37E1	2.04E1	4.08E1	3.96E1	3.41E1	300
⁵² Mn	7.06E0	6.29E0	3.00E0	1.67E1	1.47E1	7.01E0	6
⁵⁴ Mn	7.81E0	7.80E0	7.70E0	6.44E0	6.37E0	6.30E0	10
⁵⁶ Co	1.44E1	1.43E1	1.35E1	2.10E1	2.07E1	1.97E1	4
⁵⁷ Co	1.88E1	1.87E1	1.84E1	1.72E1	1.70E1	1.68E1	50
⁵⁸ Co	6.14E1	6.10E1	5.76E1	3.71E1	3.66E1	3.45E1	10
⁶⁰ Co	1.32E0	1.32E0	1.32E0	5.67E-1	5.67E-1	5.67E-1	1
⁶⁴ Cu	1.31E4	3.72E3	1.44E0	3.67E3	1.04E3	4.00E-1	80

Table 6.8: Total and specific activities of radionuclides produced in the coils by ⁶He, for the waiting times of 1 hour, 1 day and 1 one week: comparison between the straight and bent sections.

the two sections have close values. And it also shows that many of the produced radionuclides have a long half-life. It should be noted that ⁵⁶Co, ⁵⁷Co, ⁵⁸Co are present and have a specific activities of several tens of Bq g⁻¹, one week after the machine shutdown, which exceed their LEs. ⁶⁰Co values are instead below the exemption limit of 1 Bq g⁻¹.

6.4 Summary and conclusions

The present study assesses the radiological consequences of using the CERN PS machine as injector in the future beta-beam facility. Only decay losses are known and their impact has been evaluated. The prompt radiation outside the accelerator shields and the induced activity in the machine components have been estimated. The areas surrounding the PS, outside the shielding concrete, will remain classified as public or supervised areas, depending on the particular position along the ring. The calculations have considered a conservative case in which the decay losses are all concentrated in one point inside a magnet. When the other sources of point losses are known, these results can be normalized to the number of particles lost and their contribution can be added to the one from decay losses. For the assessment of the induced activity in the machine components and in the air, the real loss distributions are used and the geometry of a single accelerator cell (i.e. 3 combined-function magnets) is implemented in the simulations to represent an arc section. Furthermore, the exact material compositions are here used, based on the chemical analysis of the existing PS magnets. The airborne activity is mainly dominated by the short-lived radionuclides, like ¹³N, ¹¹C and ¹⁵O. The total annual effective dose to the population arising from the operation with neon and

helium ions amounts to $0.7 \mu\text{Sv}$ and to $0.2 \mu\text{Sv}$, respectively. These values are not significantly high but they must be summed to the emissions of the other CERN operating facilities in order to estimate the total effective dose, which cannot exceed $10 \mu\text{Sv}$ per year. The induced activity in the machine components is higher for the neon operation, as expected, and the produced radioactive nuclides are both short- and long-lived. Among the long-lived, ^{51}Cr and ^{48}V are produced in the yoke steel and in the vacuum pipe, but the specific activity is higher in the latter. The residual dose rates, due to the induced activity, are calculated for an annual operation and for waiting times of 1 hour, 1 day and 1 week. For both helium and neon operation, a week after the annual shutdown, the dose rate at a distance of 40 cm from the beam line is of $1.3\text{-}1.4 \text{ mSv h}^{-1}$: there is no relevant difference between the two ions, mainly due to the higher number of lost particles during the helium operation which compensates for neon's higher atomic number. The values for a waiting time of one day are in the range $1.32\text{-}2.3 \text{ mSv h}^{-1}$ and they have been compared to the values collected during the surveys of 2009, 2010, 2011 and 2012 in the PS. The measured data show dose rates in the order of $2\text{-}9.9 \text{ mSv h}^{-1}$ at the worst location. These values, which are higher than the ones due to beta-beam operation, further prove the suitability of the present PS within the beta-beam facility from the point of view of the radiological risks.

7 The Decay Ring (DR)

The Decay Ring (DR) is the high-energy superconducting machine in which the radioactive ions are stored in order to decay into $\nu - \bar{\nu}$ beams. During a cycle $9 \cdot 10^{12}$ ${}^6\text{He}$ ions and $4.26 \cdot 10^{12}$ ${}^{18}\text{Ne}$ ions are injected from the SPS into the DR. The duration of a cycle is of 6 s for ${}^6\text{He}$ and 3.6 s for ${}^{18}\text{Ne}$. This gives an intensity of $1.5 \cdot 10^{12}$ ${}^6\text{He}$ ions and $1.18 \cdot 10^{12}$ ${}^{18}\text{Ne}$ ions every second into the ring at an energy of nearly 92 GeV per nucleon. The ions are not further accelerated in the DR, but only accumulated. The main parameters of the machine are summarized in Table 7.1. A representation of the DR layout is given in Figure 7.1. It is composed of two

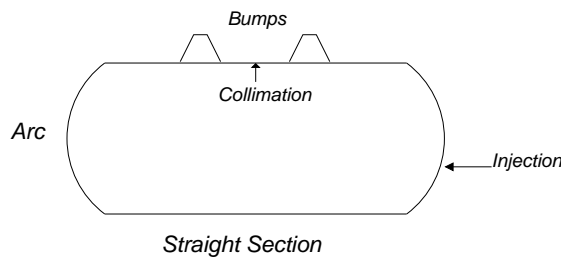


Figure 7.1: Layout of the DR.

Circumference	6911.5 m
Physical radius	1100 m
Straight section length	2468 m
Arc length	988 m
Injection energy	92 GeV/u
Maximum magnetic rigidity	935.03 T·m

Table 7.1: Main parameters of the ring.

long straight sections (SS), one of which is directed towards the detector situated in the Frejus tunnel, and two arcs. The total length is 6911,5 m (the same length of the SPS machine). The SS are optimized in order to maximize the neutrino flux at the detector. The injection

system is hosted in one of the two arcs, whilst one of the SS houses the collimation and the deflectors that create two orbit bumps. The SS consist of fourteen FODO lattices and the distance between each quadrupole is 85 m. Each arc contains ten 38.7 meter-long periods and has the optical functions as shown in Figure 7.2, where the dispersion and the horizontal and vertical betatron functions are presented for one arc [24]. A multi-turn injection system

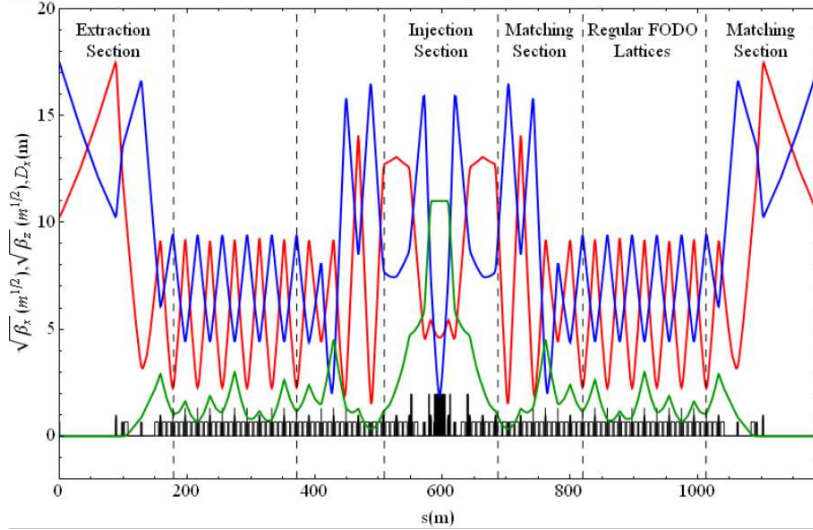


Figure 7.2: Optical functions in the arcs: in red horizontal betatron function, in blue vertical betatron function, in green dispersion function [24].

is used to increase the number of stored ions, as the intensities in the SPS are limited by the space charge effects in the PS and the source [24]. It is necessary to use an injection septum magnet which deflects the incoming beam without perturbing the stored beam. The chosen solution is an off-momentum injection and a system of four quick deflectors to avoid that the fresh beam can hit the septum blade one turn after its incoming: they are switched on at the injection time to do a bump of the closed orbit and are switched off before the fresh beam has made a turn. A specific RF program, with two variable cavity families, is then used to merge both beams and a two-stage collimation section is necessary to intercept the losses due to injection.

7.1 Beam losses

Losses in the DR, besides space-charge effects, injection and merging, which all together account for small percentages, are mainly caused by β^\pm decay and collimation. Figure 7.3 shows the percentages of losses for both ions as a function of the number of injection cycles. The decay of the stored ions causes an average continuous power loss of 10.8 W m^{-1} for ${}^6\text{He}$ and 11.8 W m^{-1} for ${}^{18}\text{Ne}$. This loss corresponds to 45% of the injected ${}^6\text{He}$ beam and 21% of the injected ${}^{18}\text{Ne}$ beam. At the end of the SS the total nominal deposited power in the first dipole of the arcs is of several tens of kilowatts [24]. Two dedicated extraction systems

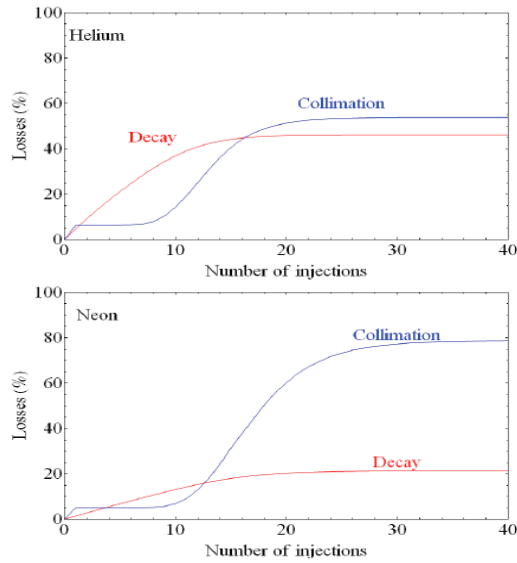


Figure 7.3: Loss amount as a function of injection cycles for ${}^6\text{He}$ (top) and ${}^{18}\text{Ne}$ (bottom) [24].

are needed at the entrances of the arcs. Energy deposition, evaluated through several codes, (BETA [75] as a stand-alone code and ACCSIM [85] coupled to FLUKA), shows that the average power deposited in the dipoles in the arcs is less than 10 W m^{-1} , but the peak values exceed the recommended limit used for the LHC super-conducting magnets (4.3 mW cm^{-3}) for both quadrupoles and dipoles: the maximum calculated value for beta beams corresponds to 30 mW cm^{-3} . The peak energy deposition is located in the bending plane of the magnets, as can be seen in Figure 7.4. For this reason an open mid-plane layout, where coils are not present in the mid plane, has been considered. First estimates of energy deposition show that the peak power is reduced by almost a factor 10 with the second layout [24]. An arc cell, composed of four dipoles and two quadrupoles is represented in Figure 7.5. The loss maps for the entrance of one of the arcs and for a cell in the arc are shown in Figure 7.6: losses in the arcs occur mainly in between the magnets. Nearly half of the decay losses occur in the arc which is after the SS without collimation section. For this arc, the losses in the previous arc and in the previous straight section, which represent in length about half of the decay ring, must be taken into account. A high fraction of the beam is also lost by collimation: 55% of ${}^6\text{He}$ and 79% of ${}^{18}\text{Ne}$ ions. The loss of particles by collimation corresponds to $9.47 \cdot 10^{11}$ ${}^{18}\text{Ne}$ per second and to $8.25 \cdot 10^{11}$ ${}^6\text{He}$ per second. This type of losses affects the collimator straight sections and also one of the bump areas. In the bump, most losses occur after the first dipole, in correspondence of the quadrupole, as shown in Figure 7.7. Figure 7.8 shows the power deposited by collimation losses in the collimation section and in one of the two bump areas.

In the present work, all calculations are performed for the collimation and bump sections, and for the arcs. Both the layouts for the magnets are considered in the estimate of the residual dose rates. The input loss maps are calculated with ACCSIM coupled to FLUKA.

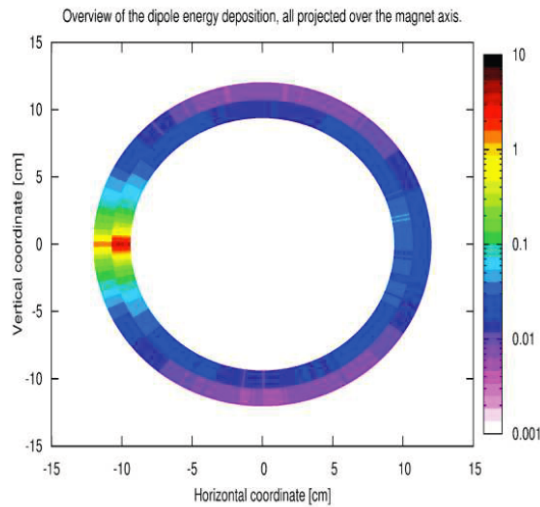


Figure 7.4: Overview of the energy deposition distribution (mW cm^{-3}) in the superconducting coils of the dipole in the lattice cell. The projection is averaged over the length of the magnet [24].

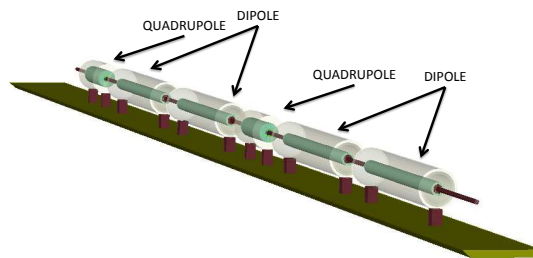


Figure 7.5: A representation of the FLUKA geometry of a cell in the arcs of the DR.

7.2 Shielding calculations

The DR will be located underground, at a depth sufficient to shield the public areas from the direct stray radiation produced during the operation. As no site has been assigned yet it is assumed here that it will be at least at 10 m from the surface. In order to allow the workers to access the areas, the lateral shields of the DR tunnel must be calculated, according to the area classification contained in the CERN Safety Radiation Code (see Chapter 4, Table 4.3). Routine operation is here considered. Since loss maps are known in details, the real distribution has been used to crosscheck the validity of the point-loss approximation. Such approximation, whenever valid, has been introduced to significantly reduce the CPU time of calculations for the evaluation of the source terms and of the attenuation lengths. As described in Section 4.2.1.1, the point-loss approximation can be applied if the losses are uniformly continuous. In

7.2. Shielding calculations

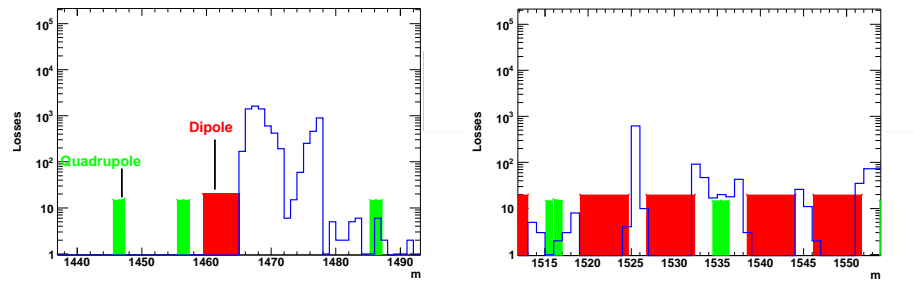


Figure 7.6: ^{18}Ne losses (blue) at the entrance (left) of the arc and in one cell (right), expressed in arbitrary units.

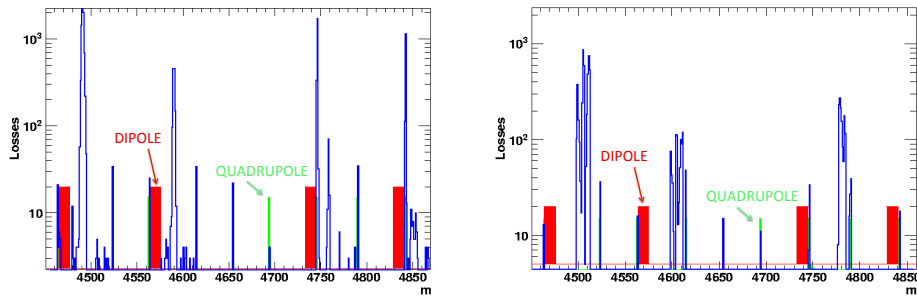


Figure 7.7: ^6He (left) and ^{18}Ne (right) losses in the first bump section, expressed in arbitrary units.

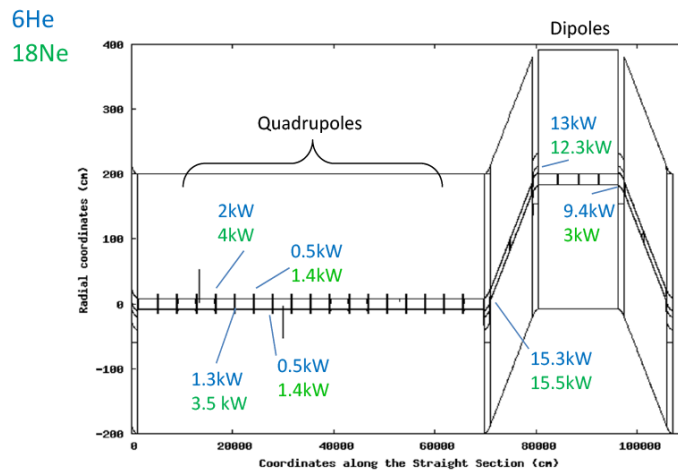


Figure 7.8: Power deposited in the collimation and in the bump sections by collimation losses: in blue for helium and in green for neon.

such case, if they occur in a section of length l they can be approximated as point losses every l , provided that the total power is conserved. The main loss points, as previously shown in Figure 7.6, are situated in between the magnets or at their entrance and are separated from each other by nearly 10 m (one dipole is 6 m long), with a well defined pattern. With these premises, the conditions for the application of the approximation to point-loss are satisfied. In order to verify the validity of the model, first the attenuation lengths and source terms in concrete are calculated for both ions at 92 GeV per nucleon with the point-loss model, using a simplified geometry. Then, given a thickness of the shielding wall for one cell in the arc, a simulation with the actual geometry and the actual loss map is performed. The ambient dose equivalent rate behind the wall is compared to the one obtained with the same wall thickness in the point-loss approximation.

7.2.1 Point-loss approximation

A simplified geometry is used, like the one used for the RCS and the PS calculations, where the beam hits a thick copper target and the beam line is surrounded by a cylindrical shield in concrete, where the ambient dose equivalent $H^*(10)$ is calculated in slabs of 20 cm. The density used for the concrete is 2.35 g cm^{-3} with a hydrogen fraction of 0.006%. From the interpolation of the attenuation curves, (Figures 7.9 and 7.10), the source term and the attenuation length are derived. They are used to calculate the shield thickness in the arcs, in the collimation and in the bump areas. The results of the interpolation are summarized in Table 7.2. The

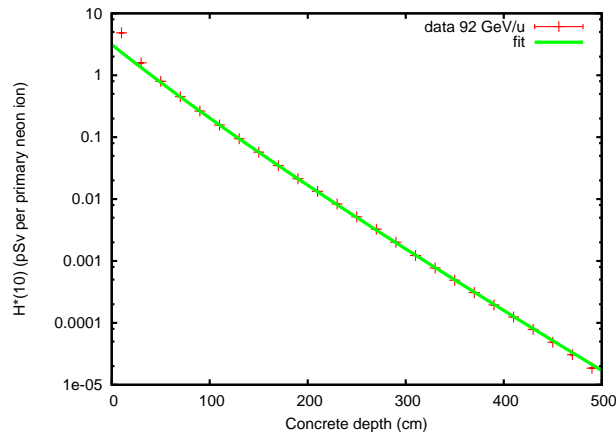
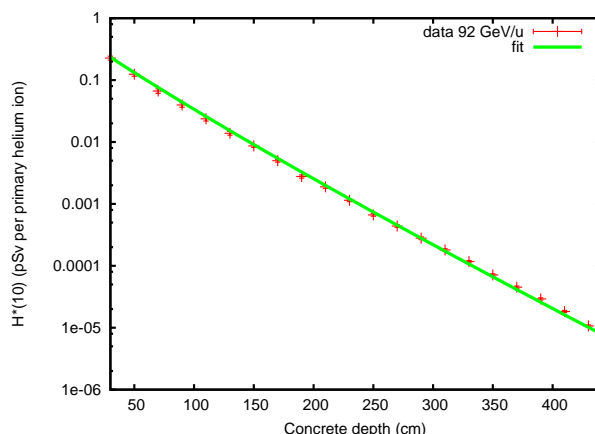


Figure 7.9: Attenuation curve in concrete at 90° for 92 GeV/u ^{18}Ne ions on copper.

results of the point-loss model calculations are shown in Table 7.3 and in Table 7.4, for ^{18}Ne and ^6He , respectively. The values of thickness are obtained by using the linear approximation in the point-loss model. For the arcs, during the ^{18}Ne operation, a maximum thickness of 7 m is required to grant a $0.5 \mu\text{Sv h}^{-1}$ dose rate beyond the shield, which corresponds, in the CERN classification of areas, to a public zone. For a simple-controlled radiation area a maximum thickness of 5.6 m must be used. Only the worst case for the bumps is given in the

Figure 7.10: Attenuation curve in concrete at 90° for 92 GeV/u ^6He ions on copper.

	Neon		Helium	
	Fit results	% Error	Fit results	% Error
H_0	$(12.5 \pm 0.02) \text{E-12}$	0.2%	$(2.26 \pm 0.02) \text{E-12}$	0.7%
λ_θ	122.20 ± 0.10	0.08%	117.07 ± 0.80	0.68%

Table 7.2: Source terms H_0 (Sv m² per primary ion) and attenuation lengths λ_θ in concrete (g cm⁻²).

	$0.5 \mu \text{ Sv h}^{-1}$	$3 \mu \text{ Sv h}^{-1}$	$10 \mu \text{ Sv h}^{-1}$
Arc 1	671.3 cm	588.5 cm	533.4 cm
Arc 2	703.5 cm	620.4 cm	565.1 cm
Bumps (best: 3 rd bend)	582.4 cm	500.7 cm	446.4 cm
Bumps (worst: 2 nd quad)	848.5 cm	764.1 cm	707.7 cm
Collimation	1028.4 cm	942.7 cm	885.5 cm

Table 7.3: Maximum shielding thicknesses for the ^{18}Ne operation in the DR, for each machine section. An extra attenuation length is included in the thickness.

summary, which corresponds to the first quadrupole after the first bend during ^{18}Ne operation and to the first bending magnet and the following straight section during ^6He operation. For the collimation area, a very thick shield would be required around the primary collimator, therefore the only possible way to avoid the construction of a 10 m-thick wall is to consider the installation of a sandwich-like shielding, containing layers of borate concrete and iron slabs. This countermeasure would indeed reduce the total thickness of the wall. Nevertheless, it would not be sufficient to make it thin at reasonable costs. Therefore the construction of a service tunnel on the side of the collimation section will be possible, but the access to it will not be granted during the operation of the machine. The access can be granted during

	$0.5 \mu\text{Sv h}^{-1}$	$3 \mu\text{Sv h}^{-1}$	$10 \mu\text{Sv h}^{-1}$
Arc 1	584.4 cm	505.7 cm	453.3 cm
Arc 2	579.7 cm	501.1 cm	448.8 cm
Bumps (best: 1 st quad)	581.4 cm	502.7 cm	450.4 cm
Bumps (worst: 1 st bend)	796.9 cm	716.0 cm	662.1 cm
Collimation	904.7 cm	823.1 cm	768.5 cm

Table 7.4: Maximum shielding thicknesses for the ${}^6\text{He}$ operation in the DR, for each machine section. An extra attenuation length is included in the thickness.

operation on the other SS of the DR, where the large acceptance of the beam pipe reduces the losses to a very small fraction of the total beam.

7.2.2 MC simulation with real loss maps

A simulation with the actual loss distribution in the arc for ${}^{18}\text{Ne}$ and the actual geometry of the arc cell is performed. The shield used has a thickness of 4.8 m, which represents the average value of the required thicknesses in order to classify as simple controlled the radiation area around the arcs. The results of the MC simulation is shown in Figure 7.11, where the dose rates are expressed in $\mu\text{Sv h}^{-1}$ per unit of primary particle. The most relevant losses occur

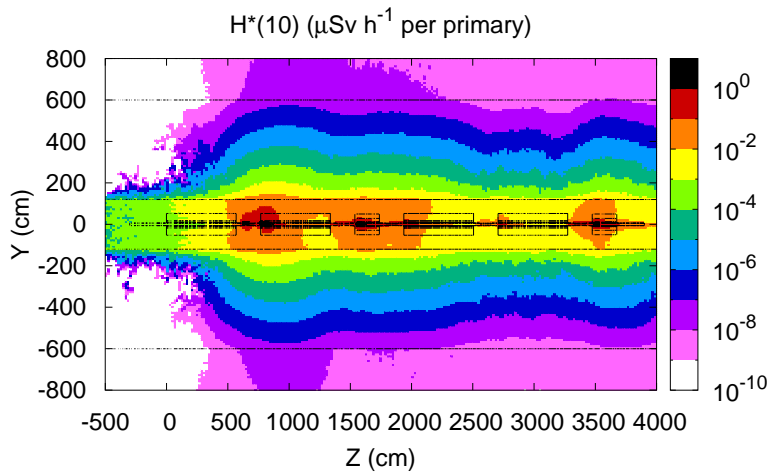


Figure 7.11: ${}^{18}\text{Ne}$ ambient dose equivalent rate map in one cell in the arcs (top view), expressed in $\mu\text{Sv h}^{-1}$ per unit primary particle.

between the first and the second dipole, where $3.4 \cdot 10^8$ particles are lost every second. In correspondence of this point, at 90° , behind the wall of 4.8 m, the ambient dose equivalent

rate is estimated to range from 10 to 20 $\mu\text{Sv h}^{-1}$, over a 10 m distance. In other points along the wall, the dose rate values, normalizing the dose rate values in Figure 7.12 to the loss intensity at these locations, range from 1.7 and 4 $\mu\text{Sv h}^{-1}$, if we only consider the downstream part of the tunnel after the second dipole.

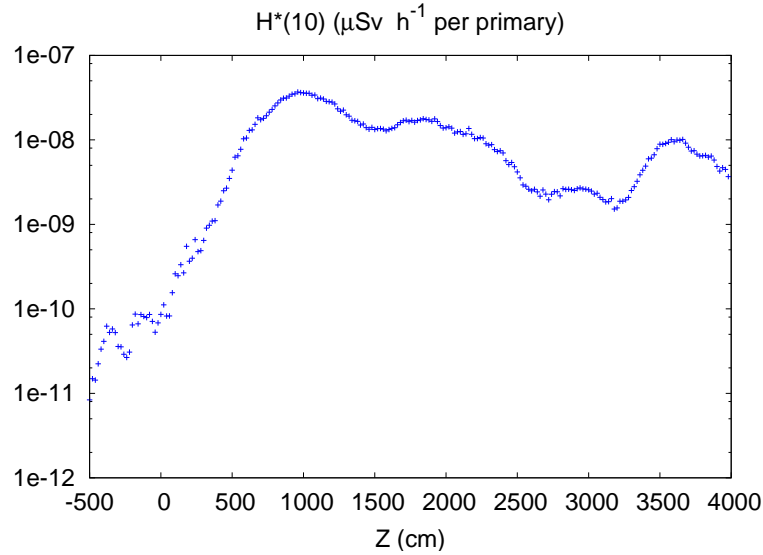


Figure 7.12: ^{18}Ne ambient dose equivalent rate as a function of the distance Z in one cell in the arcs (top view), expressed in $\mu\text{Sv h}^{-1}$ per unit primary particle.

For the same thickness of the shield, in the point-loss approximation, using the source term and attenuation length in Table 7.2 in the expression (see Chapter 4, eq.(7.1)):

$$H(E_p, \theta, \frac{d}{\lambda}, d/\lambda) = \frac{H_0(E_p, \theta)}{r^2} \exp\left[-\frac{d}{\lambda_\theta g(\alpha)}\right], \quad (7.1)$$

we obtain:

$$H^*(10) = \frac{12.5 \cdot 10^{-6} [\mu\text{Sv}] \cdot [m]^2}{6^2 [m]^2} \exp\left[-\frac{4.8 [m]}{0.52 [m]}\right]. \quad (7.2)$$

When normalized to the number of lost particles, the ambient dose equivalent rate becomes 41.65 $\mu\text{Sv h}^{-1}$ for the worst loss point, between the first and second dipole. In the other points it drops to values comprised between 3 to 10 $\mu\text{Sv h}^{-1}$.

The comparison shows that the point-loss model predicts a value for the dose rate which is on average the double of the maximum value calculated in the simulation with the real distribution of losses in the machine. When translated into shield thickness, in the case here considered, this factor corresponds to a difference of 32 cm of concrete. As the attenuation

length for ^{18}Ne in concrete at 92 GeV per nucleon is 52 cm, the extra 32 cm calculated with the point-loss model are already included in the safety margin (one extra attenuation length) usually considered when deciding the thickness for a shielding wall. From this comparison it can be concluded that the simplified model leads to a reasonable and yet conservative estimate of the shielding with respect to fully detailed MC simulations with complete beam losses.

7.3 Induced Activity

Magnets in the arcs are based on the same superconducting technology used for the design of the Large Hadron Collider (LHC) ones, with niobium-titanium cables and copper wedges. The actual geometry and design of the machine are used for the induced-activity calculations. Given the large amount of losses, in order to prevent high energy deposition and magnet quenching, protection systems have to be foreseen all along the arcs. Two types of magnet design are considered. In the first layout, magnets with an aperture of 80 mm are envisaged together with steel absorbers, placed inside the beam pipe in between magnets so that they can absorb part of the lost particles; in the second layout, in the mid-plane of each magnet the coils are replaced by aluminum absorbers. In this case, the aperture can be reduced to 50 mm. The layout for open mid-plane cold dipoles is shown in Figure 7.13. In the layout

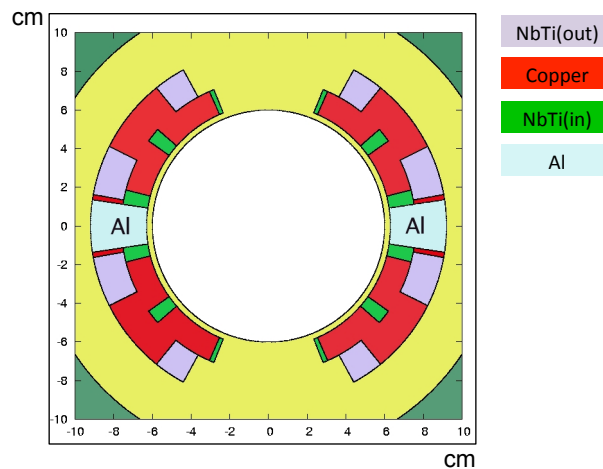


Figure 7.13: Detailed drawing of the cross sections of the coils of the dipoles in the DR, in the open mid-plane layout. The specifications for the material compositions can be found in Table 7.5.

with absorbers the dipoles are straight magnets, 5.7 m long; in the open mid-plane layout, the dipoles are sector magnets, 6 m long. A complete description of the materials composing the yokes and the coils of cold magnets is summarized in Tables 7.5 and 7.6 [86]. The compositions are those used in the LHC magnets, with NbTi cables. In the dipole layout, the cables are mixed with copper wedges. In all magnets the cables have two different composition and density

(NbTi(in) and NbTi(out)), depending on their radial position in the magnet. The outer layers in the dipoles have a higher density than the inner ones. Also liquid helium is considered in the geometry.

		ρ (g cm ⁻³)	Cu	Nb	Liq. He	Kapton	Ti
Dipole	NbTi(in)	6.1	48	10	12	13	17
	NbTi(out)	7.6	47	9	11	17	16
Quadrupole	NbTi(in)	7.0	63	7	10	9	11
	NbTi(out)	6.3	53	8	10	15	14

Table 7.5: Coil composition (volume fraction in %) in the cold magnets in the arcs.

	ρ (g cm ⁻³)	Fe	Ni	Mn	Si	C	Cu
Yoke composition in cold magnets (%)	7.87	98	0.01	0.004	0.001	0.001	0.002

Table 7.6: Yoke composition (weight fractions) in the cold magnets in the arcs.

In the collimation and bump sections only warm magnets are used. The lattice of a bump, represented in Figure 7.14, is composed of four warm dipoles, called BN2 at the entrance and exit, BN3 in the second and third bends, and nine quadrupoles (Q). The design of the warm

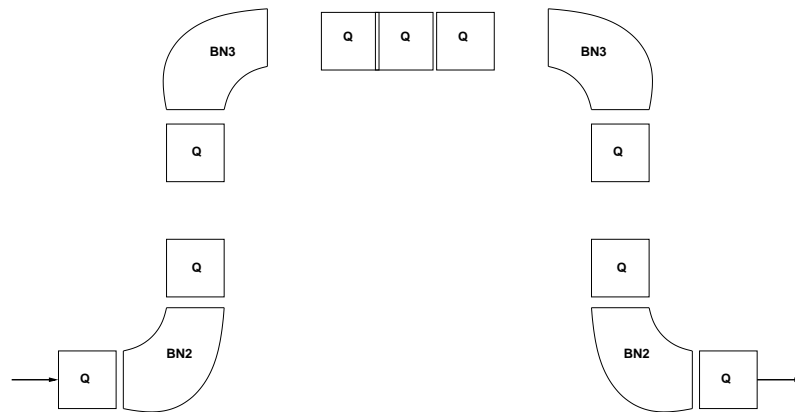


Figure 7.14: Lattice of a bump section in the DR.

magnets in the bump sections is based on the SESAME models [87]: dipoles are C-shaped, 12 m long with flat parallel ends and an aperture radius of 8 cm. The coils are made of copper, the yokes of low-carbon iron: the design of the magnets and the detailed material compositions are given in Figure 7.15 and in Table 7.7. The collimators are carbon blocks, 30 cm thick: the primary one is at a distance of 226 m from the first of the secondary ones. The distance

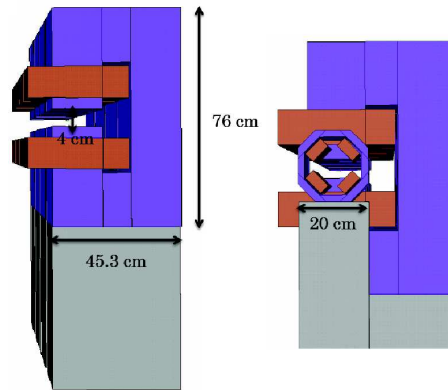


Figure 7.15: Warm quadrupole and dipole in the bumps as they are represented in the geometry of the simulations.

	Fe	C	Si	Mn	P	S	Al
Yoke composition in warm magnets (%)	98	0.001	1.5	0.2	0.05	0.0005	0.2

Table 7.7: Yoke composition in warm magnets in the bumps in %.

between the secondary ones is of 230 m.

7.3.1 Air activation

The characteristic lethargy spectra of secondary neutrons, protons and pions produced in the air by ^{18}Ne are shown in Figure 7.16. Both protons and neutrons present a peak at nearly 120 GeV, which corresponds to the neutron-proton quasi-elastic interaction. The spectra for pions have softer shapes at high energy and a lower energy end-point. In the calculations they are convoluted with the isotope production cross-sections, as explained in Chapter 4, and the yields of the radionuclides produced in the air during the annual operation of the DR is assessed. The impact on doses to the reference population and to the workers is then calculated.

7.3.1.1 Dose to the reference population

The design and the location of the DR tunnel have not been decided yet. Therefore, in order to assess the contribution to the total effective dose given to the reference population, some assumptions have been made on the dimensions, on the ventilation system and on the location. As the SPS is its injector, the position of the DR is in the area close to it. In order to convert the produced activity into effective dose, as explained in Chapter 4, conversion coefficients are

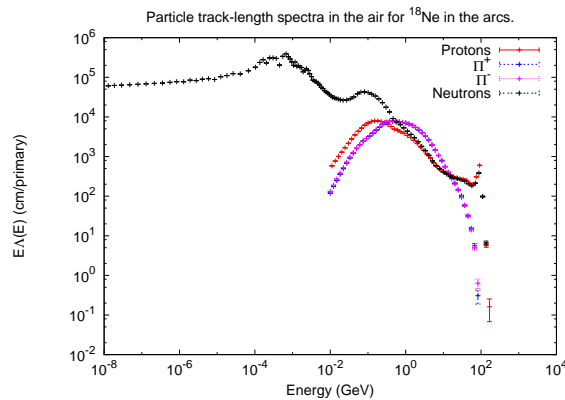


Figure 7.16: Track length spectra for protons, neutrons and pions produced in the air for ^{18}Ne operation.

required. In literature a set of activity-to-dose conversion coefficients, previously calculated for the SPS [88] and for ISOLDE, are available. For the SPS there are six sets that correspond to the six SPS release stacks (TT10, TT20, TT60, TT70, BA3 and BA5), ISOLDE has only one stack. The conversion coefficients present different values depending on many factors including the distance from the stack to the reference population, the population itself (in terms of occupancy time and age) and the wind direction [59]. The SPS stacks are disseminated on French and Swiss territory: TT10, TT60 and TT70 are situated in the CERN Meyrin site and the TT20 is in the south-west end of the Prevezin site. BA3 is in Prevezin and the nearest dwellings are at 500-700 m, BA5 is surrounded by several houses, divided into four reference groups living at an average distance of 200-300 m. For the ISOLDE reference population see Chapter 5 (RCS). A comparison between the SPS and the ISOLDE coefficients is performed to choose those to be used for the DR situation. In Figure 7.17, the conversion coefficients for the most relevant stacks are plotted: on the top, for short-lived nuclides, on the bottom for long-lived ones. Since the exact location of the DR is not known, the worst-case scenario is assumed here: the ISOLDE coefficients are used for the short-lived isotopes and the TT20 for the long-lived ones. Two stacks at least are required for the DR. Their possible locations in the tunnel are shown in Figure 7.18: one that collects losses from the collimation section, the second bump area and one arc (2), and the other for the air activated in the second arc and in the first bump (1). For the air diffusion the following ventilation and geometrical parameters are used: a ventilation rate F of 20000 m^3 and an outlet with a height of 100 m and a diameter of 2 m. These parameters are chosen accordingly to the LHC parameters. The annual irradiation time corresponds to the 10^7 s operation. The results for the collimation and bump sections, for the first and second arcs are summarized in Tables 7.8, 7.9, 7.10, for the ^{18}Ne operation, which represents the worst case between the two ions. The total released annual effective dose exceeds $6 \mu\text{Sv}$: although below the CERN annual limit of $10 \mu\text{Sv}$, the value should be lowered when considering all the other installation releases, namely those from ISOLDE and CNGS. The most contributing nuclides are the short-lived ones, like ^{41}Ar , ^{11}C , ^{38}Cl , ^{39}Cl , ^{13}N , but also

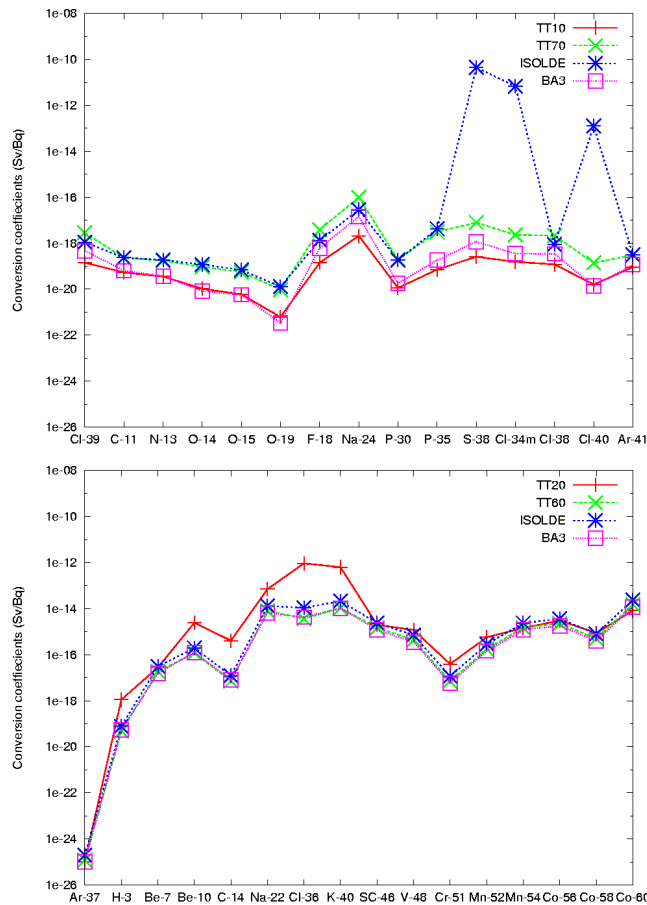


Figure 7.17: Conversion coefficients from activity to dose for several stacks (ISOLDE, TT20, TT60, BA3): comparison between short-lived nuclides (top) and for long-lived nuclides (bottom).

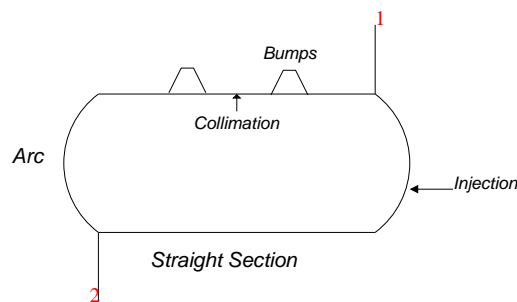


Figure 7.18: Possible layout of the ventilation outlets in the DR.

^7Be , which has a half-life of nearly 53 days and deposits, together with ^{32}P , in the soil and in the grass, with a possible contamination of water and milk produced by grazing cows. The total annual effective dose released with ^6He operation attains the value of $3.7 \mu\text{Sv}$, which is

Annual Effective Dose (μSv)			
Nuclide	Arc 1	Entrance of the arc 1	Total per nucl.
Ar-41	6.66E-1	3.93E-2	7.05E-1
C-11	9.79E-2	1.77E-2	1.16E-1
Be-7	8.77E-2	< 1E-7	8.77E-2
Cl-39	5.62E-2	7.94E-3	6.42E-2
Cl-38	1.96E-2	2.48E-3	2.21E-2
P-32	1.30E-2	2.26E-3	1.53E-2
Na-24	8.25E-3	2.38E-3	1.06E-2
N-13	5.62E-3	7.92E-4	6.41E-3
F-18	3.16E-3	1.04E-3	4.21E-3
S-38	2.60E-3	3.85E-4	2.99E-3
Na-22	1.83E-3	5.66E-4	2.40E-3
Al-28	1.62E-3	4.21E-4	2.04E-3
Mg-28	1.01E-3	2.36E-4	1.25E-3
C-14	8.67E-4	5.11E-5	9.18E-4
P-33	8.65E-4	1.40E-4	1.00E-3
Si-31	8.06E-4	1.89E-4	9.95E-4
S-35	2.91E-4	4.50E-5	3.36E-4
Mg-27	1.13E-5	3.20E-6	1.45E-5
H-3	7.53E-6	< 1E-7	7.53E-6
K-38	9.66E-7	1.70E-7	1.14E-6
Total for all nuclides			1.04

Table 7.8: Contribution to the total annual effective dose from losses in the first arc during ^{18}Ne operation. $F = 20000 \text{ m}^3$, $\text{Vol}_{out} = 31252.4 \text{ m}^3$ (outlet located after the first SS).

below the contribution of ^{18}Ne . It should be considered that with both the ion operations in a year, the total releases due to beta beams would exceed the CERN limit with the only DR. Possible technical solutions could be foreseen for the decrease of the airborne radioactivity: different ventilation rates in different sections of the machine (lower rates in the sections where the most intense losses occur), storage balloons which are already employed at CERN at the ISOLDE facility, machine optics changes in order to decrease the instantaneous particle losses.

7.3.1.2 Inhalation dose and external exposure to activated air for workers

As already done for the RCS and for the PS, the inhalation dose and the external exposure to the activated air for workers in the DR tunnel are calculated for several scenarios of intervention, in the hypothesis of ventilation failure. The results are summarized in Table 7.11. Both inhalation dose and external exposure have values bigger than the PS ones by a factor 1.2. The values for the external exposure are under the limit of $10 \mu\text{Sv h}^{-1}$ and represent a small percentage of the residual dose rate in the tunnel at 1 m from the beam line (see next Section).

Annual Effective Dose (μSv)			
Nuclide	Arc 2	Entrance of the arc 2	Total per nucl.
Ar-41	1.66E0	7.87E-2	1.74E0
C-11	2.45E-1	3.53E-2	2.80E-1
Be-7	2.19E-1	< 1E-7	2.19E-1
Cl-39	1.41E-1	1.59E-2	1.56E-1
Cl-38	4.90E-2	4.95E-3	5.39E-2
P-32	3.26E-2	4.51E-3	3.71E-2
Na-24	2.06E-2	4.77E-3	2.54E-2
N-13	1.40E-2	1.58E-3	1.56E-2
F-18	7.91E-3	2.09E-3	1.00E-2
S-38	6.51E-3	7.71E-4	7.28E-3
Na-22	4.58E-3	1.13E-3	5.72E-3
Mg-28	2.54E-3	4.72E-4	3.01E-3
C-14	2.17E-3	1.02E-4	2.27E-3
P-33	2.16E-3	2.79E-4	2.44E-3
Si-31	2.01E-3	3.78E-4	2.39E-3
S-35	7.28E-4	9.01E-5	8.18E-4
H-3	1.88E-5	< 1E-7	1.88E-5
K-38	2.41E-6	3.40E-7	2.75E-6
Total for all nuclides			2.56

Table 7.9: Contribution to the total annual effective dose from losses in the second arc for ^{18}Ne operation. $F = 20000 \text{ m}^3$, $\text{Vol}_{out} = 31252.4 \text{ m}^3$ (outlet located after the second SS).

7.3.2 Residual Doses

For the calculations of residual ambient dose equivalent rates during the maintenance, 10^7 seconds of annual irradiation and the three waiting times of one hour, one day, one week are assumed. The loss maps, obtained through ACCSIM coupled to FLUKA, are used as the input distribution of particles in the simulations. The magnetic field of the magnets is implemented into the simulations in order to take into account the exact positions where the particles are lost. All the dose rate maps for the several locations in the DR can be found in Appendix B. Here, in Figures 7.19 and 7.20, the residual dose-rate maps are presented for both the ions in the arcs, for the worst case. On the left side the maps represent the situation for the layout with absorbers, whilst on the right side there are those for the layout with open mid-plane dipoles. In general, the layout with absorbers presents a higher dose rate at 1 m from the beam line, due to the activation of the steel that compose the absorbers. The stainless steel indeed usually contains cobalt in traces, of the order of 1000 ppm in mass fraction, which are enough to generate high residual doses: the produced long-lived nuclides, like ^{60}Co , which emits γ radiation at 1.332 MeV, are responsible for the higher dose. In Figure 7.21, the residual nuclides produce by activation of the steel in the absorbers and relevant for the residual dose are shown, with their specific activities after one hour, one day and one week. Besides cobalt isotopes,

7.3. Induced Activity

Annual Effective Dose (μSv)				
Nuclide	Bump 1	Bump2	Collim.	Total per nucl.
Ar-41	1.08E-1	1.73E-1	2.05E-4	2.82E-1
P-32	2.14E-2	2.66E-2	6.06E-1	6.54E-1
Na-24	1.71E-2	2.19E-2	4.36E-1	4.75E-1
Cl-39	1.17E-2	2.39E-2	4.66E-1	5.02E-1
Na-22	4.51E-3	5.60E-3	1.10E-1	1.20E-1
Al-28	3.25E-3	4.12E-3	8.31E-2	9.05E-2
F-18	3.06E-3	4.89E-3	8.44E-2	9.24E-2
S-38	2.07E-3	3.02E-3	6.68E-2	7.18E-2
Mg-28	1.88E-3	2.39E-3	5.05E-2	5.48E-2
Cl-38	1.46E-3	3.81E-3	6.81E-2	7.34E-2
P-33	1.36E-3	1.69E-3	3.94E-2	4.25E-2
Si-31	8.29E-4	1.23E-3	2.34E-2	2.54E-2
C-11	8.19E-4	3.96E-3	4.67E-2	5.14E-2
S-35	4.45E-4	5.53E-4	1.32E-2	1.42E-2
C-14	3.82E-4	4.74E-4	8.88E-5	9.45E-4
Si-32	8.86E-7	1.10E-6	2.32E-5	2.52E-5
N-13	1.38E-7	2.78E-6	1.91E-5	2.20E-5
Total for all nuclides				2.55

Table 7.10: Contribution to the total annual effective dose released in the environment, due to losses in the bumps and the collimation section. $F = 20000 \text{ m}^3$, $\text{Vol}_{out}^{bump1} = 86620.4 \text{ m}^3$, $\text{Vol}_{out}^{coll} = 78012.4 \text{ m}^3$, $\text{Vol}_{out}^{bump2} = 73287.4 \text{ m}^3$ (outlet located after the SS).

t_{irr}	t_{wait}	t_{int}	Inhalation dose (μSv)	External exposure (μSv)
1 hour	0	1 hour	5.26E-2	1.62
1 day	0	1 hour	2.72E-2	3.42
1 week	0	1 hour	6.58E-2	3.42
1 month	0	1 hour	2.75E-1	3.43
1 month	1 hour	1 hour	2.62E-1	1.81
3 months	0	1 hour	2.90E-1	3.44
3 months	1 hour	1 hour	2.77E-1	1.82

Table 7.11: Inhalation and external-exposure dose to workers for several irradiation and waiting times, coming from induced activity in the air.

other long-lived nuclides are present, like ^{48}V , ^{51}Cr and ^{44}Sc . Figure 7.22 shows the specific activities in the yoke a week after the shutdown for the two magnet layouts: with absorber and open mid-plane magnets. The comparison indicates that specific activities are higher in the yoke when the absorbers are not present. The absorbers are indeed intercepting most of the lost particles, becoming highly activated and partially sparing the magnet yokes. On average the ratio between the two values for the same radionuclide is 1.23, except for ^{59}Fe where the

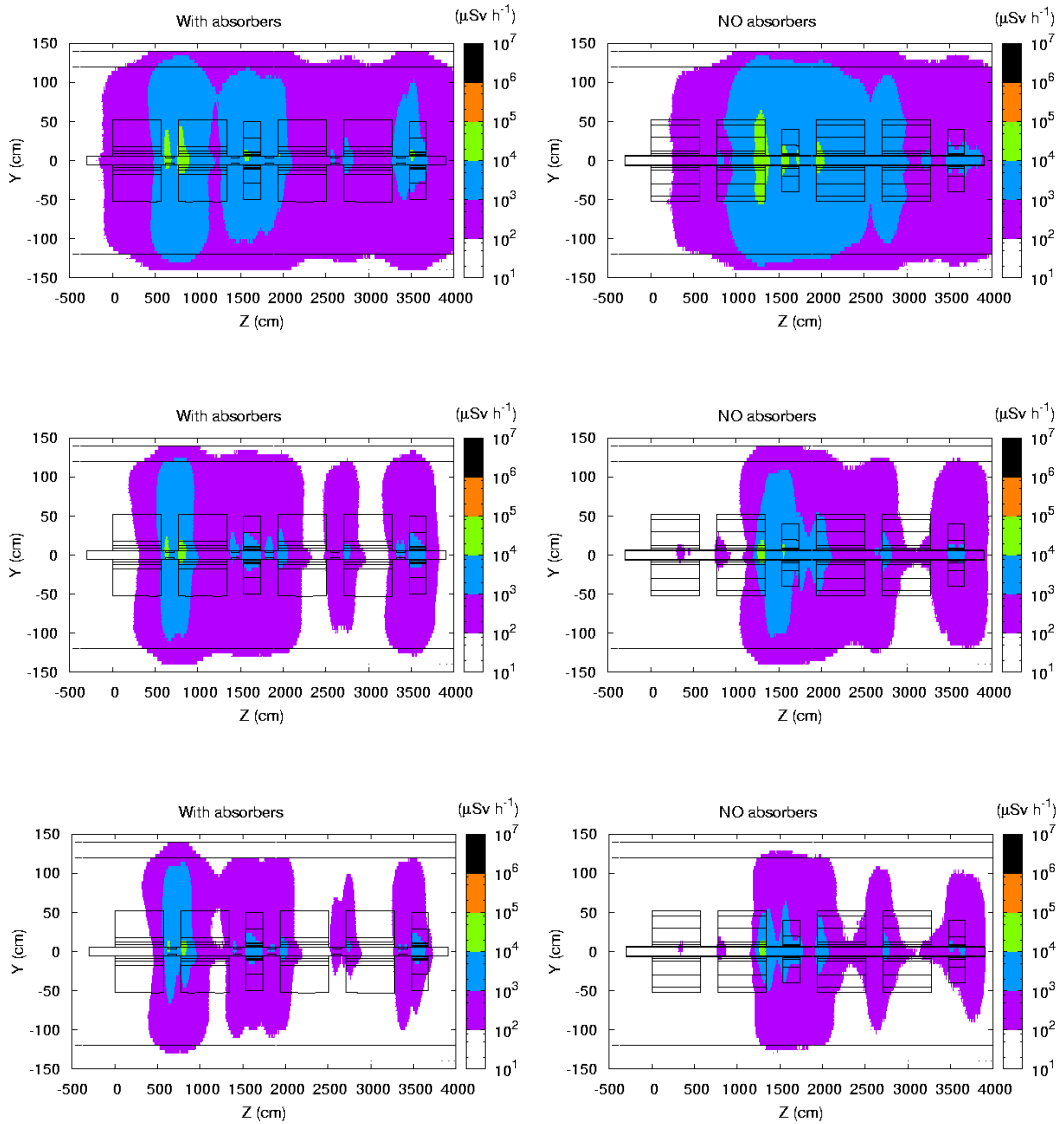


Figure 7.19: Residual dose rates for the waiting times of 1 hour, 1 day and 1 week in one arc cell, for ^{18}Ne : layout with absorbers on left, layout with open mid-plane magnets on the right.

ratio is equal to 6.5. Residual doses are higher for ^{18}Ne than for ^6He and this can be explained with the different amount of losses, with the energy which is slightly higher for neon and also with the different number of nucleons. After a week, the residual dose rate at 1 m from the beam line is in between 1 and 10 mSv h^{-1} in the absorber layout and between $100 \mu\text{Sv h}^{-1}$ and 1 mSv h^{-1} in the open mid-plane layout, for ^{18}Ne operation. For ^6He operation, the doses drop below $100 \mu\text{Sv h}^{-1}$ after one week in both layouts and the difference between them is not as marked as in the neon case. In Appendix B, in Figures B.4, B.5, B.6, B.7, B.8, B.9, B.10 and B.11, the results for the collimation section are shown for neon and helium respectively.

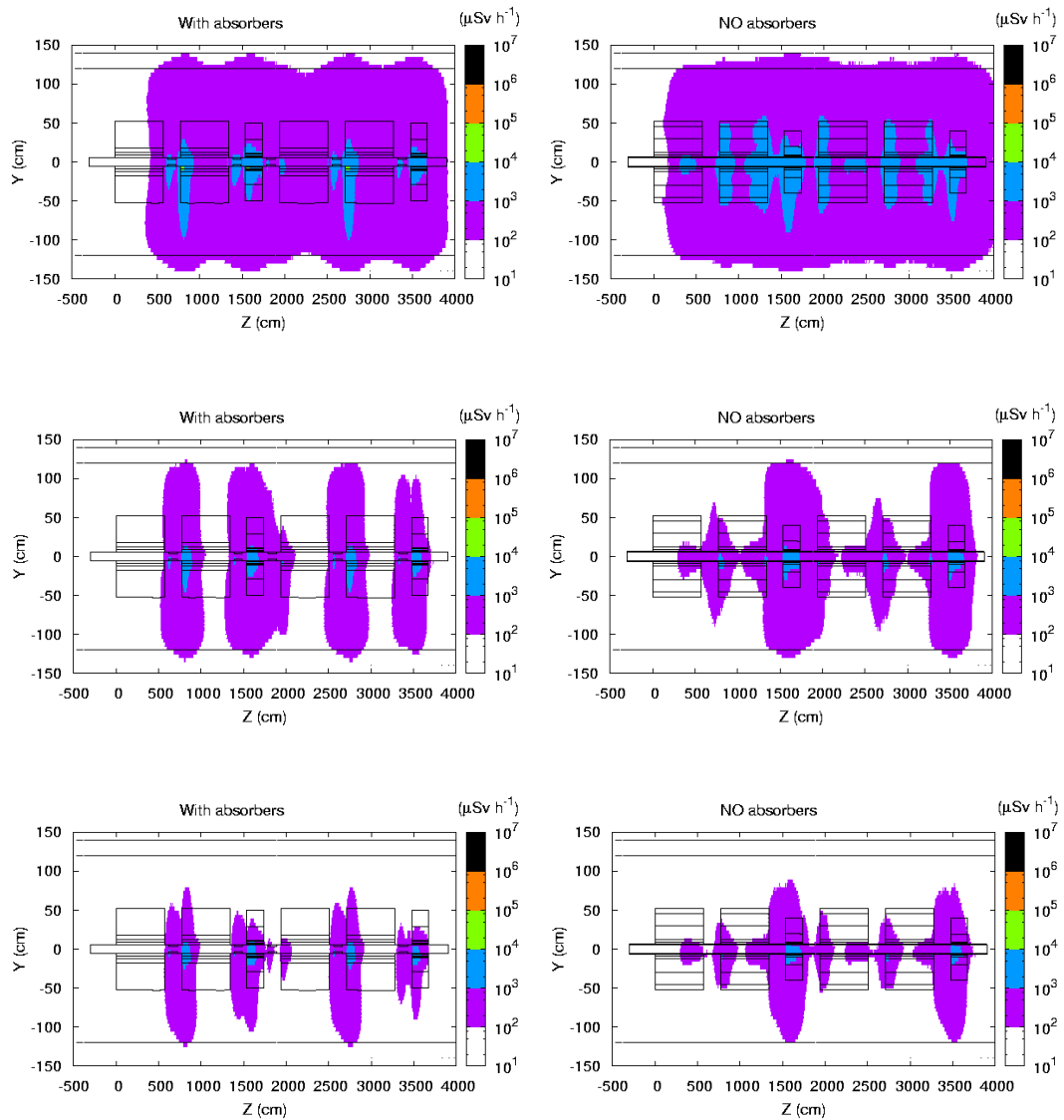


Figure 7.20: Residual dose rates for the waiting times of 1 hour, 1 day and 1 week in one arc cell, for ${}^6\text{He}$: layout with absorbers on left, layout with open mid-plane magnets on the right.

The area around the primary collimator, according to CERN Safety Code, would be classified as a prohibited area for neon operation, even after one week, as the dose rate at 1 m stays in between 100 mSv h^{-1} and 1 Sv h^{-1} . In the case of helium, after a week, the value is between 10 and 100 mSv h^{-1} and it corresponds to a high-radiation area. In Appendix B, in Figures B.6, B.7, B.8, B.9, B.10 and B.11, the worst points in the bump areas for the two primary beams are presented. In both neon and helium cases, the dose rate at 1 m from the beam line ranges from 1 to 10 mSv h^{-1} . In all the areas, the residual dose rate rapidly decreases from a hour to a day waiting time, but the difference between a day and a week waiting time is not significant.

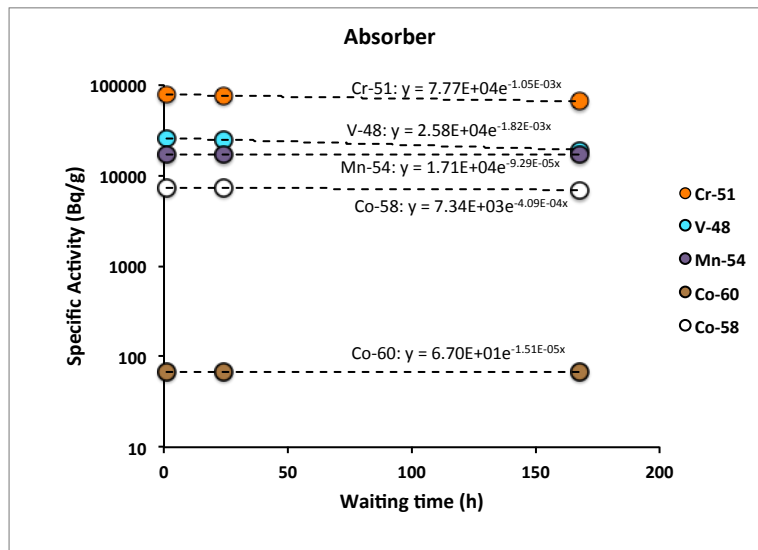


Figure 7.21: Residual nuclides in the absorber, specific activities for ¹⁸Ne operation.

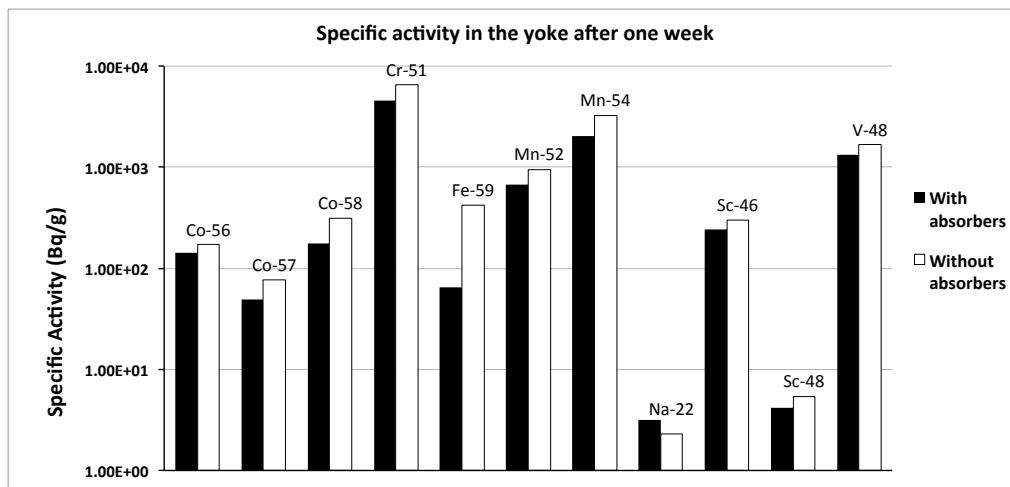


Figure 7.22: Specific activities after one week in the dipole yoke, in the layouts with and without absorbers, for ¹⁸Ne operation.

This is of course due to the presence of short-lived radionuclides in the first hours after the shutdown, which becomes negligible after a week, as it can be seen in Figure 7.23, where the residual dose-rates for the three waiting times at 1 m for the open mid-plane dipole are compared.

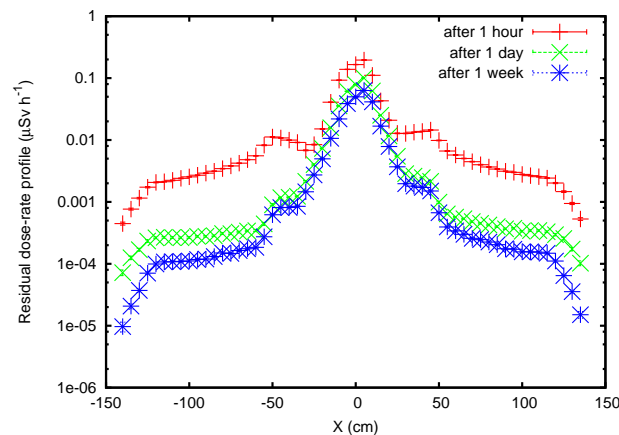


Figure 7.23: Residual dose-rate profile for ^{18}Ne operation at the dipole for several waiting times (open mid-plane layout).

7.4 Summary and conclusions

The shielding thickness for the different sections of the DR is calculated using the point-loss approximation model and a simplified geometry. A conservative approach is used: shield thicknesses are evaluated for both ion operations and the worst case is taken for the shield in each location in the machine. In order to classify the surrounding areas as supervised radiation areas, concrete layer ranging from a 5- to 7-m thickness are required. In the areas surrounding the collimation sections of the machine, the access during operation will be forbidden, due to the high intensity of the prompt radiation. Indeed, a concrete shield capable of attenuating the radiation down to allowed doses would result in an excessively thick and expensive layer. This issue can be addressed by using shielding material that can moderate the high-energy component of the neutron spectra, like for instance iron, or by using concrete which is enriched with elements that can make neutron capture, like boron.

The annual effective dose to the reference population during the operation of beta-beams with ^{18}Ne , due to the airborne activity, would reach a value of $6 \mu\text{Sv}$ and of $3.7 \mu\text{Sv}$ during the operation of ^6He . Even if these values are below the annual limit for CERN, they still represent a risk, as there would be a small margin for the other facilities. Some mitigation measures could be taken in the design phase, like the reduction of beam losses or the implementation of storage balloons where the activated air decays before release. Furthermore, ad-hoc ventilation systems could be designed, on the model of those conceived for the LHC tunnel. The inhalation dose for workers accessing the DR tunnel for intervention and their external exposure to the radionuclides produced in the air have been assessed and they do not represent an issue as they are below the reference limits. Besides, the external exposure to the airborne radioactivity represents a small fraction of the total residual dose rate due to the activation of the machine components.

The residual dose rates in the decay ring vary with the location in the machine. In particular, the collimation areas after the yearly operation of both helium neon ions will be prohibited areas also after a waiting time of one week. This does not represent a showstopper for the construction of the machine at CERN: the collimation section could be kept separated from the rest of the machine. Unavoidable interventions immediately after the shutdown could be organized in shifts optimized in time and procedure, like those used for the LHC. In the arcs, the comparison between the layout with absorbers and the layout with open mid-plane magnets show that the residual dose rates after one week are higher with the former design. This is explained with the high activation of the steel in the absorbers. The induced activation of the steel in the yokes, though, is higher in the open-mid plane layout. This is explained by the higher number of particles which are lost in the yoke when the absorbers are not present. The difference between the values can be considered negligible in determining the choice of the layout, especially when comparing specific activities of the produced radionuclides which are anyway higher than the exemption limits and will have comparable decay time lengths in terms of radioactive waste characterization. The decision on the magnet layout should be based on the results of the energy deposition studies, which show that the open mid-plane magnet represents a safer choice in terms of magnet protection. The area of the arcs, at the end of the annual operation, a week after the shutdown, can be classified as limited-stay controlled radiation area, where the maximum ambient dose equivalent rate is 2 mSv h^{-1} .

8 Conclusions

In this thesis the radiological risks for the installation of a future beta-beam facility at CERN have been analyzed.

In the first part, an overview of the beta-beam facility in its conceptual design has been given. That design is at the base of the study that started in 2004 within the EURISOL DS proposal and was concluded with the recent research on the feasibility of such a facility at CERN, especially in terms of efficiency in ion production and radiation protection aspects. The main characteristics of physics performance and technological features of beta beams have been presented, with particular stress on the description of the accelerator chain and on the different types of losses. This information provides the basis from which the entire study has been developed.

The third chapter provides the motivation for the use of the MC code FLUKA, employed in the simulation of the interactions of particles with matter. The premise of this study is the need for correctly predicting the interaction of ion primary beams with accelerator components. Several conclusions can be drawn from this part of the work. First of all, it is important to stress that the FLUKA code can effectively reproduce the secondary neutron spectra which are produced in the interaction of ions with matter. This is true even in the low-energy range, at 100 MeV per nucleon, which represents a threshold energy between two different nuclear models used in the code. The capability of reproducing neutron spectra is fundamental in radiation protection studies, even more so for the assessment of the prompt radiation generated in an ion-beam facility, the design of the shielding, and the evaluation of the induced radioactivity in the accelerator components, as well as in the air released into the environment. For this purpose, the code has been tested with experimental data available in the literature, collected in a campaign of measurements of neutron spectra generated in the interaction of ion beams with a thick target. The capability of the code to predict angular energy distribution of secondary ions has also been tested. In particular, angular spectra of secondary ^{17}F and ^{17}O produced in the reaction $^{16}\text{O}+^{12}\text{C}$ at 14.7 MeV per nucleon were collected during measurements performed at the IThemba Labs in Cape Town at the end of 2009. The comparison between predicted and experimental data shows that the

Conclusions

code can only partially reproduce the real spectra. On the one hand, it can be concluded that the neutron-proton pick-up reactions and the complete fusion mechanism, which are two important mechanisms in the low-energy range for nucleus-nucleus interactions, are successfully implemented in FLUKA. On the other hand, it is not possible to draw conclusions about reactions occurring below a total energy of 80 MeV, due to the lack of experimental data in this energy range. Also, at the moment of writing this thesis, the spectra for fragments lighter than ^{17}F and ^{17}O cannot be simulated because the mechanism of two-nucleon stripping, which also affects the spectra in the intermediate-energy range, is not yet implemented in FLUKA. The development of MC codes which are able to simulate the production of light fragments is still the object of research today. In particular, efforts are put in studying reactions that involve light ions, including the reactions of interest for medical physics applications. In terms of radiation protection of ion-beam facilities, the capability of predicting spectra of secondary hadrons is of utmost importance for an accurate estimate of the prompt and induced radiation fields generated in the accelerator. For a more precise evaluation of the radioactivity induced by the primary beam in the accelerator components, further development of the nuclear models used in MC codes is needed. The behavior of protons and ions at the energy of 100 MeV per nucleon has been analyzed in order to assess analogies and differences in the production of secondary neutrons. The analysis shows that it is not possible to scale the results for protons to those for the ions, because of the different production mechanisms of the secondary neutrons at high energies.

The fourth chapter presents an overview of the radiation protection methods used for all the calculations. Both analytical and MC methods have been used in the assessment of the radiological impact of beta beams in the CERN environment. The reference for dose rate limits and regulations on the access to radiation areas is the CERN Safety Code. The fundamental parameters to consider in a radiation protection study are the intensity and energy of the primary beam, the types of particles, the loss distribution maps and the chemical composition of all materials. A detailed and precise geometry of the system is needed for a precise evaluation of the induced radioactivity. At the same time, MC biasing techniques and simplified geometries can effectively be used to optimize the calculation time. Analytical models are typically used to describe the diffusion of the radionuclides in the air and through the ventilation outlets. In particular, special coefficients that take into account the wind characteristics and the deposition in environmental matrices are used to convert the specific activity of the airborne radionuclides into effective dose to the reference group of the population.

The second part of this work deals with the actual calculation of the above-mentioned radiation protection parameters for all the beta-beam machines in the energy range from 100 MeV per nucleon to 92 GeV per nucleon. These results include the shielding thickness required around the machines, the residual dose rates expected near the accelerator during shutdown, the specific activities of the radionuclides produced in the machine components, and the air activation, including its impact on the doses to personnel and to the population living in the surrounding of the installations. The attenuation lengths in concrete have been calculated for both ^{18}Ne and ^6He ions at several energies comprised between 100 MeV per nucleon and

92 GeV per nucleon. The conclusion of the shielding study shows that the concrete walls around the RCS should have a thickness variable between 270 cm and 580 cm, depending on the loss point considered and on the radiological classification of the surrounding areas. The maximum thickness corresponds to one specific position in the arcs, where the shielding must protect areas accessible to the public from radiation produced in a high-intensity beam loss point. A less stringent radiological classification of the area to be shielded (e.g., from public area to radiation area) would reduce the required thickness by as much as 130 cm. In the PS, to achieve classification as a public area, 360 cm of concrete are needed, while 300 cm are sufficient for a supervised radiation area. The most demanding shielding requirements are encountered in the DR, where the high-intensity and high-energy losses, especially in the collimation area, cannot be shielded with standard concrete walls. In fact, along the collimation section a thickness of almost 9 m would be necessary in order to respect the dose rate constraints of a simple-controlled radiation area. In this case, the suggested solution is to use a sandwich-like wall, made up of several different materials, such as borate concrete and iron slabs. Alternatively, access to adjacent tunnels must be forbidden during operation.

In terms of airborne radioactivity, the maximum annual effective dose given by all CERN installations to a reference population group must not exceed 10 μSv . During the beta-beam operation with ^{18}Ne , the total annual effective dose has been estimated to reach, in the worst case, a value of 7.4 μSv , where the contribution of the DR alone is of 6 μSv . This effective dose is below the limit for CERN but would represent an unacceptable level when combined with the contributions of other facilities operated in the same year, and therefore should be reduced. In order to do so, a more detailed knowledge of the dimensions of the tunnel and of its depth in the ground are required. This information would then be used to evaluate several possible airflow rates, with a method similar to the one used for the LHC at CERN. In addition, storage balloons can be used to keep the air until the decayed radionuclides have reached the allowed release limits.

The residual dose rates in the RCS, following a year of operation, stay in the order of several mSv h^{-1} even one week after the shutdown of the machine. The RCS tunnel will then be classified as limited-stay controlled area, accessible after one week. The high activation of the machine components, which is responsible for the high dose rates close to the beam line, might impose the use of a remote-handling system for the accelerator maintenance. Another mitigation measure is the reduction of beam losses in the quadrupoles in the arcs and in the electrostatic septum. By doing so, the decay losses will become dominant and the residual dose rates will drop drastically. Concerning the PS, it has been possible to compare the estimated residual dose rates after operation for the beta beams with today's dose rates, which result from the operation of the PS as a proton machine and which are documented in the survey data collected from 2009 to 2012. The measured dose rates are higher than those predicted, proving that using the PS for beta beams will not pose additional radiological risks in terms of material activation. The residual dose rates in the DR vary with position: the collimation section is the worst case as even after one week it will remain classified as a prohibited area. This does not represent a show stopper as the collimation section could be

Conclusions

kept separated from the rest of the machine and maintenance could be organized with very short, well planned intervention – following dose-optimization procedures like the ones used for the LHC. The other areas in the machine will be accessible one week after the shutdown.

In conclusion, this thesis work proves the feasibility of a future beta-beam facility at CERN from the point of view of radiation protection. In addition, it provides a framework that can be used for similar calculations where ions of comparable mass number and in the same energy range are involved. It presents the limits of the low-energy nuclear models used in modern MC codes and provides experimental data that can be used for future benchmarks. Finally, it presents a simplified method for time-efficient calculation of shielding thicknesses with minor impact on the design accuracy. After this radiation protection study, the overall feasibility of a beta-beam complex at CERN has been further investigated [89] by taking other aspects into account. The latest results show that the baseline remains the same as the one presented in this work, namely with the same ions as primary beams. At the same time, these studies have cast light on the need of optimization for the bunching in the accelerator chain and protection of the magnets from radiation. Following the results presented in this work, which have been audited by the CERN Scientific Policy Committee, radiation protection is not considered a limit for the realization of beta beams at CERN.

A Residual dose rate maps in the RCS

In this appendix, the residual dose rate maps for an irradiation time of 10^7 seconds, which corresponds to a continuous operation of three months, are given for the several locations in the RCS and for both the ions: in the septum area and in the arcs. Figure A.1 (see also Chapter 4) is presented again: it shows the layout of the RCS with the several losses and their locations in the ring.

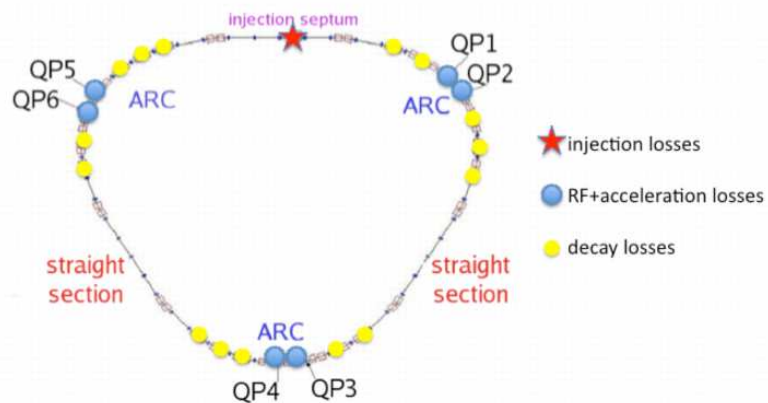


Figure A.1: Layout of the RCS with the different kinds of losses and their locations in the ring.

Appendix A. Residual dose rate maps in the RCS

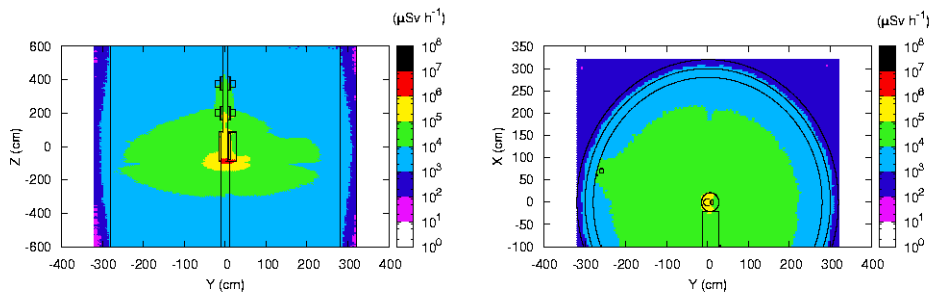


Figure A.2: Residual dose rate map after one hour for ${}^6\text{He}$, in the septum area.

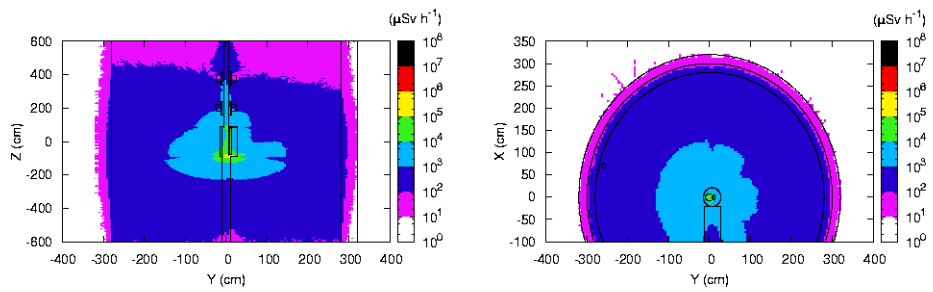


Figure A.3: Residual dose rate map after one day for ${}^6\text{He}$, in the septum area.

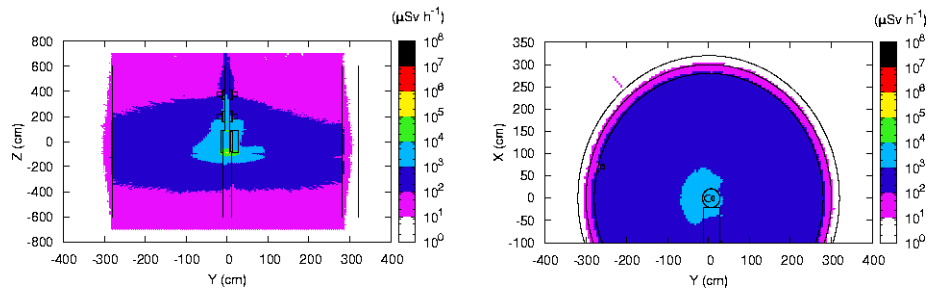


Figure A.4: Residual dose rate map after one week for ${}^6\text{He}$, in the septum area.

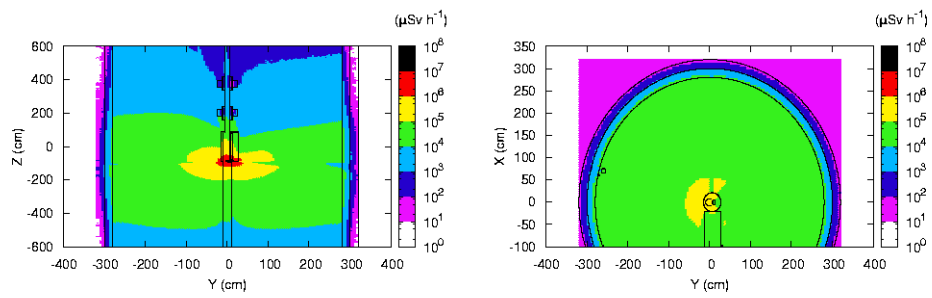


Figure A.5: Residual dose rate map after one hour for ^{18}Ne , in the septum area.

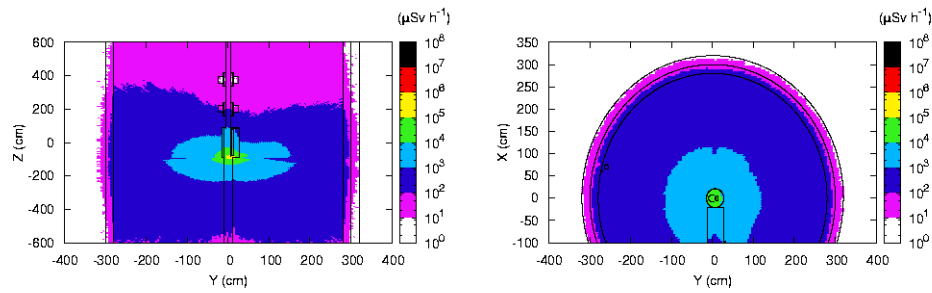


Figure A.6: Residual dose rate map after one day for ^{18}Ne , in the septum area.

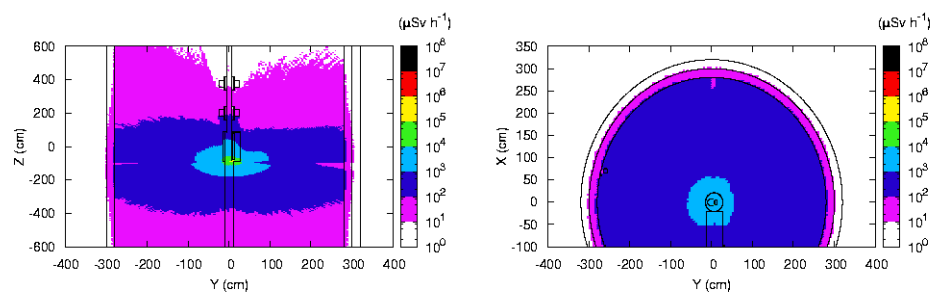


Figure A.7: Residual dose rate map after one week for ^{18}Ne , in the septum area.

Appendix A. Residual dose rate maps in the RCS

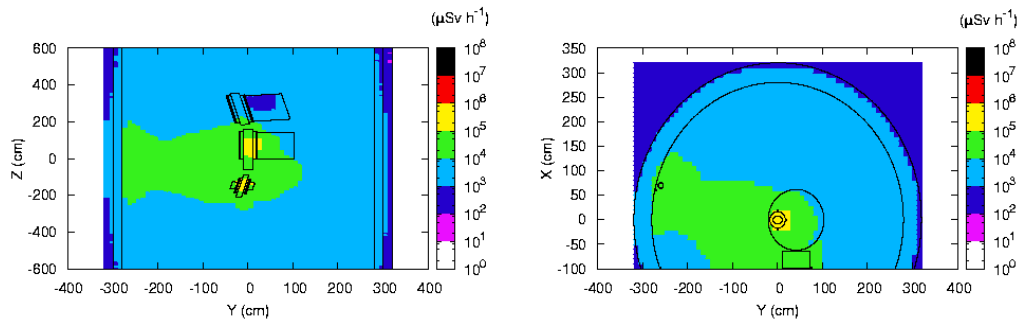


Figure A.8: Residual dose rate map after one hour for ${}^6\text{He}$, in the arcs for RfC-acceleration and decay losses.

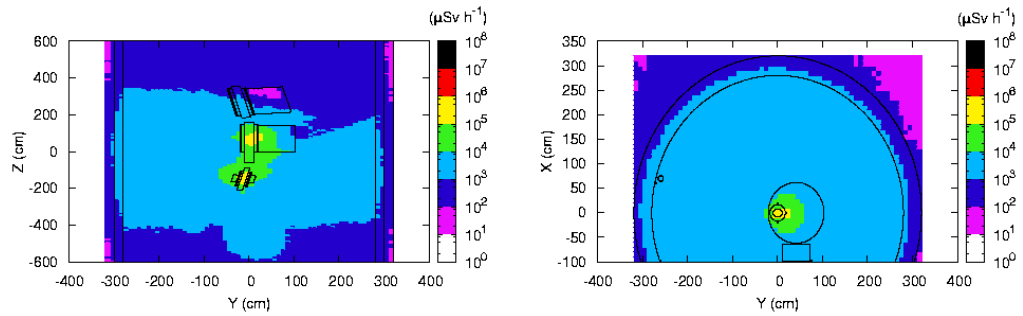


Figure A.9: Residual dose rate map after one day for ${}^6\text{He}$, in the arcs for RfC-acceleration and decay losses.

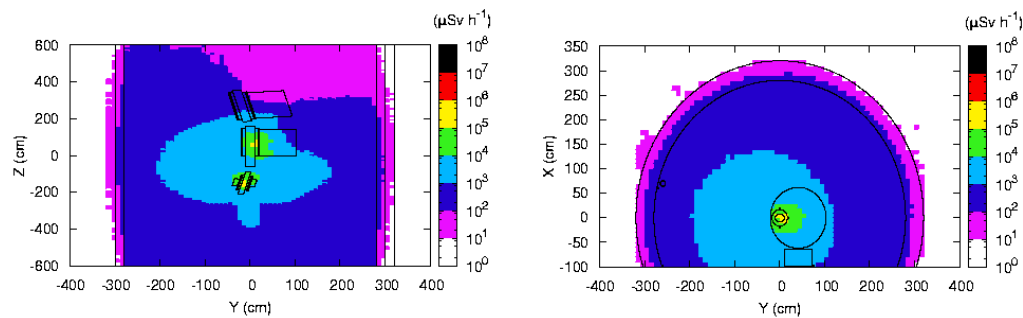


Figure A.10: Residual dose rate map after one week for ${}^6\text{He}$, in th arcs for RfC-acceleration and decay losses.

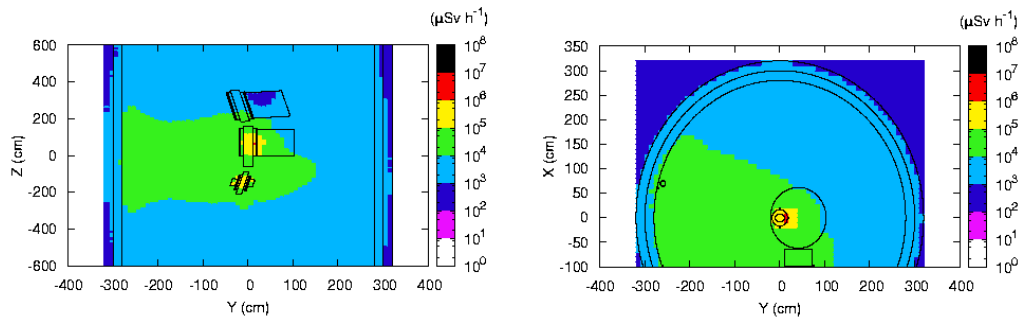


Figure A.11: Residual dose rate map after one hour for ^{18}Ne , in the arcs for RfC-acceleration and decay losses.

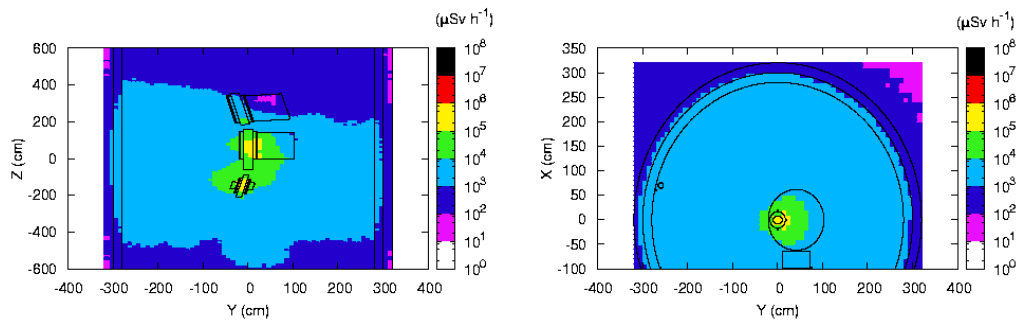


Figure A.12: Residual dose rate map after one day for ^{18}Ne , in the arcs for RfC-acceleration and decay losses.

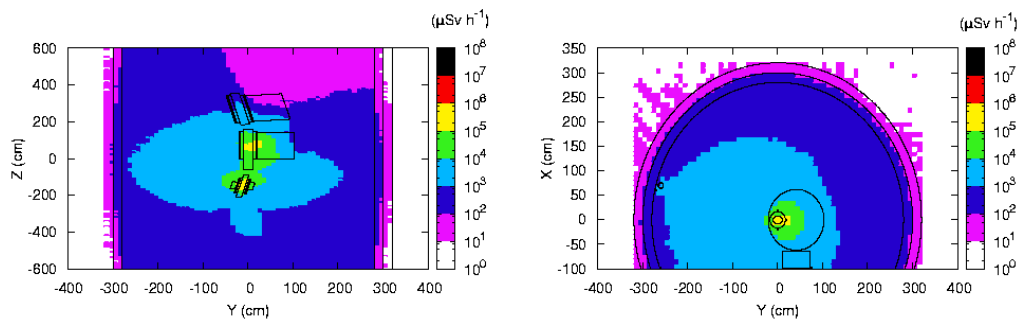


Figure A.13: Residual dose rate map after one week for ^{18}Ne , in th arcs for RfC-acceleration and decay losses.

B Residual dose rate maps in the DR

In this appendix, the residual dose rate maps for an irradiation time of 10^7 seconds, which corresponds to a continuous operation of three months, are given for the several locations in the DR and for both the ions: in the arcs, in the collimation section and in the bump area. Figure B.1 (see also Chapter 6) is presented again: it shows the layout of the DR.

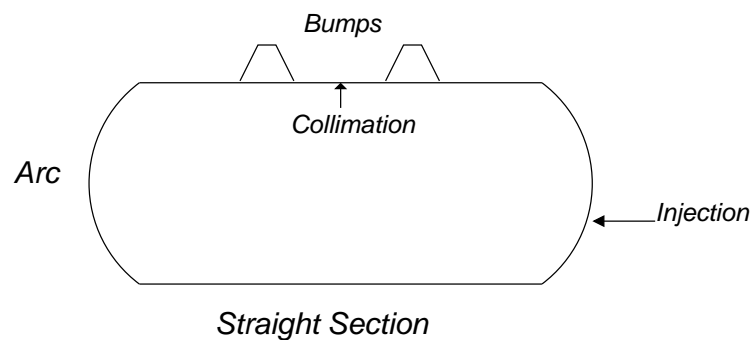


Figure B.1: The layout of the DR with the names of the main sections.

Appendix B. Residual dose rate maps in the DR

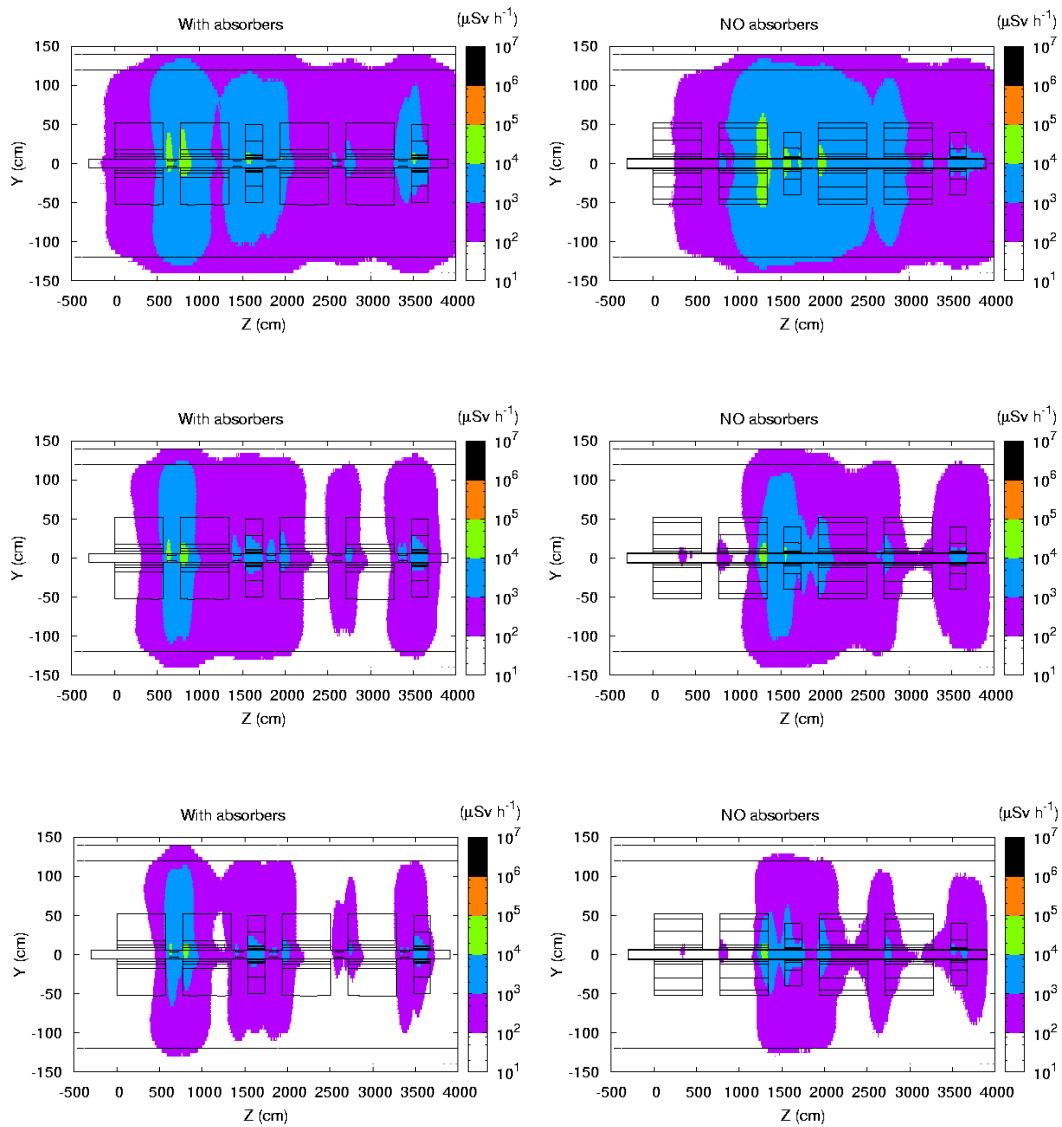


Figure B.2: Residual dose rate maps for the waiting times of 1 hour, 1 day and 1 week in one arc cell, for ^{18}Ne : layout with absorbers on left, layout with open mid-plane magnets on the right.

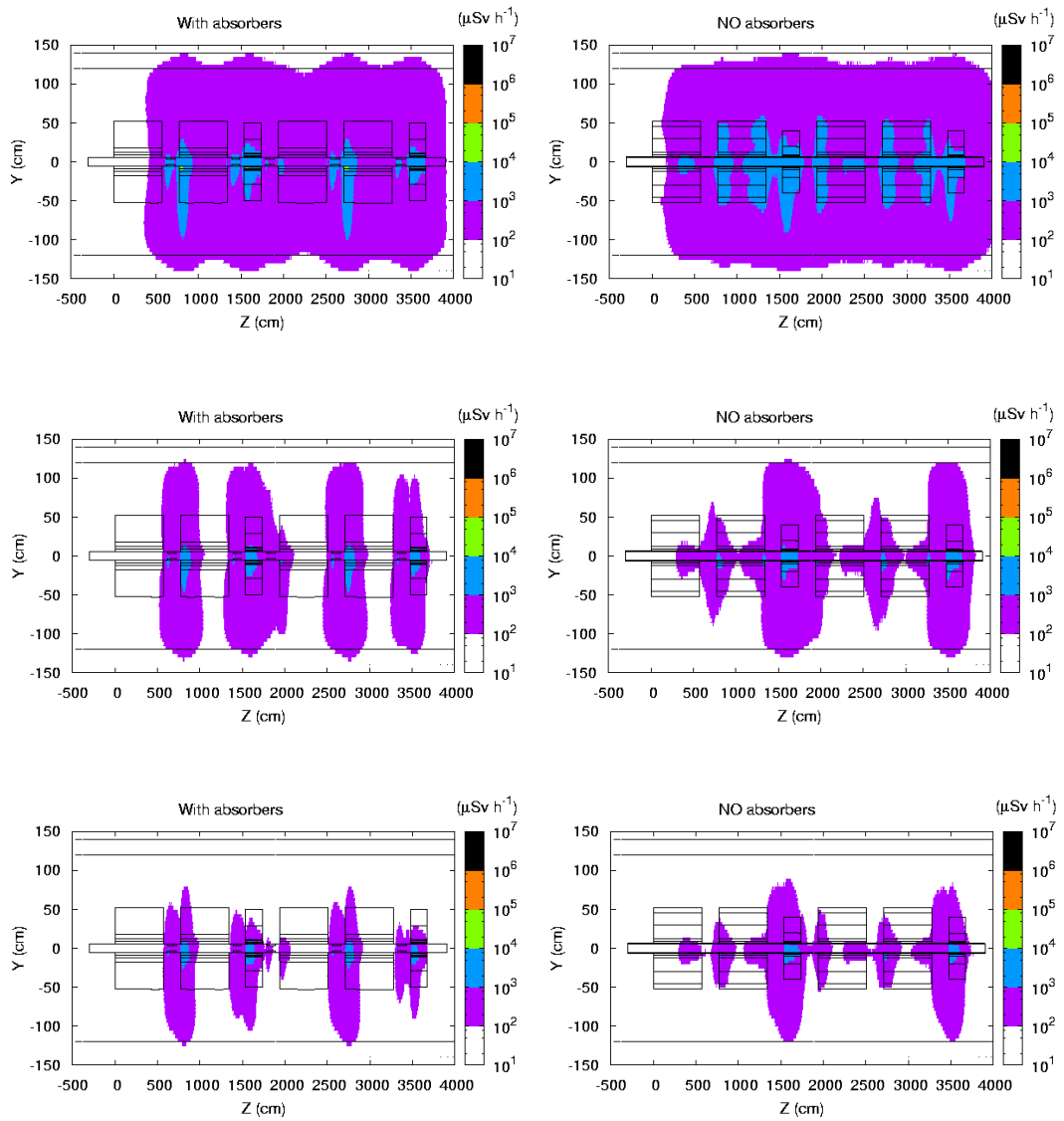


Figure B.3: Residual dose rate maps for the waiting times of 1 hour, 1 day and 1 week in one arc cell, for ${}^6\text{He}$: layout with absorbers on left, layout with open mid-plane magnets on the right.

Appendix B. Residual dose rate maps in the DR

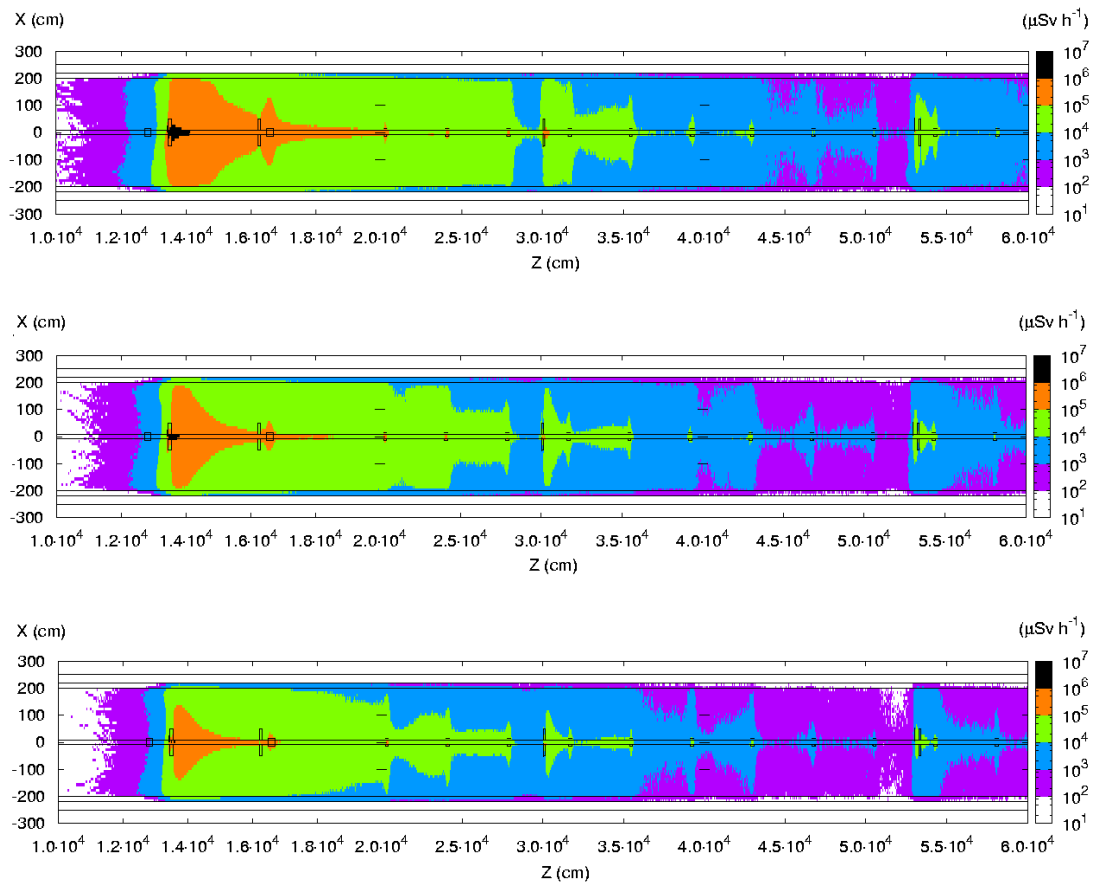


Figure B.4: Residual dose rate maps for the waiting times of 1 hour, 1 day and 1 week in the collimation section, for ^{18}Ne .

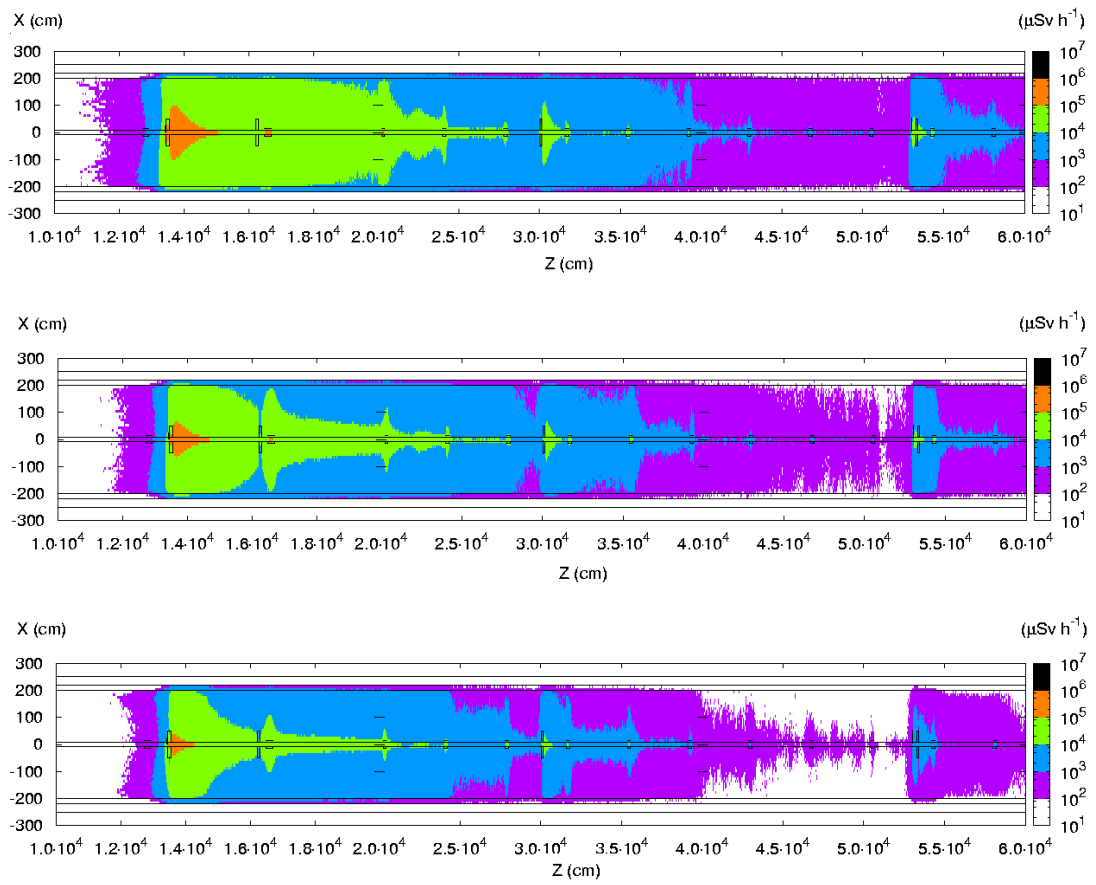


Figure B.5: Residual dose rate maps for the waiting times of 1 hour, 1 day and 1 week in the collimation section, for ${}^6\text{He}$.

Appendix B. Residual dose rate maps in the DR

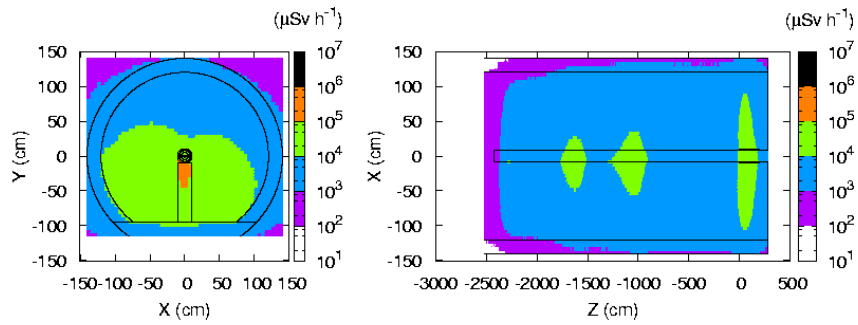


Figure B.6: Residual dose rate maps after one hour for ^{18}Ne , in the second bump, in the second quadrupole (worst case).

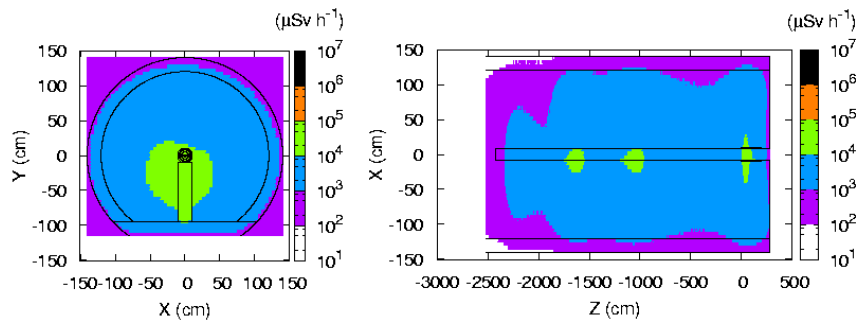


Figure B.7: Residual dose rate maps after one day for ^{18}Ne , in the second bump, in the second quadrupole (worst case).

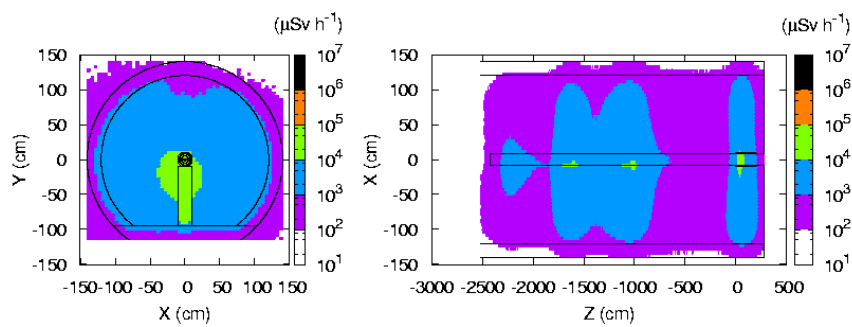


Figure B.8: Residual dose rate maps after one week for ^{18}Ne , in the second bump, in the second quadrupole (worst case).

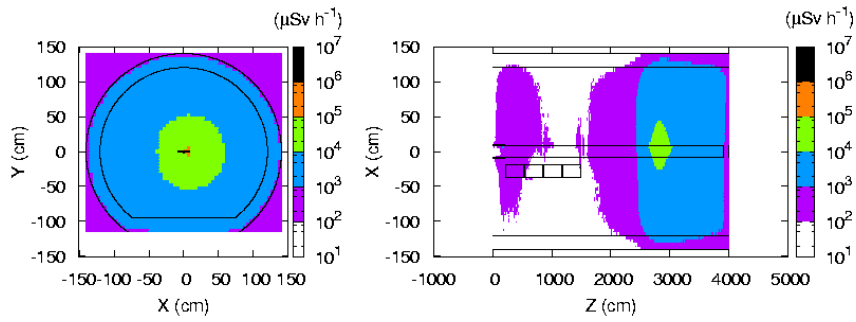


Figure B.9: Residual dose rate maps after one hour for ${}^6\text{He}$, in the second bump, in the first bending magnet (worst case).

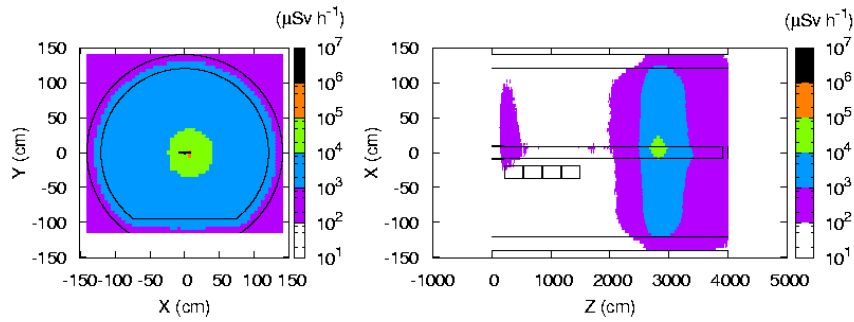


Figure B.10: Residual dose rate maps after one day for ${}^6\text{He}$, in the second bump, in the first bending magnet (worst case).

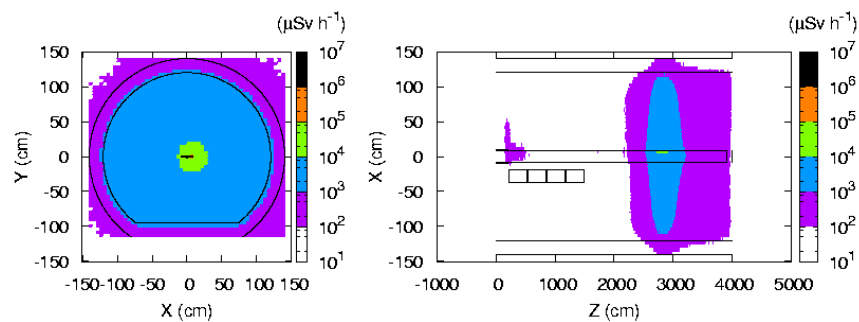


Figure B.11: Residual dose rate maps after one week for ${}^6\text{He}$, in the second bump, in the first bending magnet (worst case).

Bibliography

- [1] M. Lindroos and M. Mezzetto, *Beta Beams*, Imperial College Press, (2009).
- [2] V. Gribov and B. Pontecorvo, *Neutrino astronomy and lepton charge*, Phys. Lett., Vol. 28B, Number 7, (1969).
- [3] B. T. Cleveland et al., *Measurement of the solar electron neutrino flux with the Homestake chlorine detector*, Astrophys. J., Vol. 496, (1998).
- [4] K. S. Hirata et al. [KAMIOKANDE collaboration], *Observation of B-8 Solar Neutrinos in the Kamiokande-II Detector*, Phys. Rev. Lett., Vol. 63, (1989).
- [5] Q. R. Ahmad et al. [SNO collaboration], *Direct evidence for neutrino flavour transformation from neutral-current interactions in the Sudbury Neutrino Observatory*, Phys. Rev. Lett., Vol. 89, (2002).
- [6] K. Eguchi et al. [KamLAND collaboration], *First results from KamLAND: Evidence for reactor anti-neutrino disappearance*, Phys. Rev. Lett., Vol. 90, (2003).
- [7] E. Aliu et al. [K2K collaboration], *Evidence for muon neutrino oscillation in an accelerator-based experiment*, Phys. Rev. Lett., Vol. 94, (2005).
- [8] D. G. Michael et al. [MINOS collaboration], *Observation of muon neutrino disappearance with the MINOS detectors and the NuMI neutrino beam*, Phys. Rev. D, Vol. 97, (2006).
- [9] F. Arneodo et al. [ICARUS collaboration], Nucl. Instrum. and Meth. A, Vol. 461, (2001); P. Aprili et al., *The ICARUS experiment*, CERN-SPSC-2002-027.
- [10] OPERA collaboration, *An appearance experiment to search for $\nu_\mu \rightarrow \nu_\tau$ oscillations in the CNGS beam. Experimental proposal*, CERN-SPSC-2000-28.
- [11] G. Acquistapace et al., *The CERN neutrino beam to Gran Sasso*, CERN 98-02, INFN/AE-98/05, (1998).
- [12] K. Nishikawa, *Status of the T2K Experiment at J-Park*, Proceedings of Neutrino Telescopes 2007, 197-210, Milla Baldo Ceolin Venice, (2007).
- [13] D. S. Ayres et al. [NOvA collaboration], *NOvA proposal to build a 30-kiloton off-axis detector to study neutrino oscillations in the Fermilab NuMI beamline*, arXiv:hep-ex/0503053.

Bibliography

- [14] B. Autin et al., *Conceptual design of the SPL, a high-power superconducting H^- LINAC at CERN*, CERN-2000-012.
- [15] R. Garoby, *The SPL at CERN*, CERN-AB-2005-007.
- [16] M. V. Diwan et al., *Very long baseline neutrino oscillation experiments for precise measurements of mixing parameters and CP violating effects*, Phys. Rev. D, Vol. 68, (2003).
- [17] M. V. Diwan et al., *Proposal for an experimental program in neutrino physics and proton decay in the homestake laboratory*, arXiv:hep-ex/0608023.
- [18] P. Zucchelli, *A novel concept for a neutrino factory: the beta-beam*, Phys. Lett. B, Vol. 532, (2002).
- [19] B. Autin et al., *The acceleration and storage of radioactive ions for a neutrino factory*, CERN/PS 2002-078 (OP); Nufact Note 121, Proceedings of Nufact02, London, (2002); J. Phys. G: Nucl. Part. Phys. 29, (2003).
- [20] M. Lindroos and T. Nilsson, *The acceleration and storage of radioactive ions for a beta-beam facility*, Proceedings of RNB6, Argonne, USA, (2003); Nucl. Phys. A, Vol 746, (2004).
- [21] M. Benedikt and M. Lindroos [on behalf of the Beta-beam task], *The Beta-beam within EURISOL DS*, EURISOL DS/TASK12/TN-06-01.
- [22] M. Benedikt and S. Hancock, *A novel scheme for injection and stacking of radioactive ions at high energy*, NIM A 550 (2005) 1-5.
- [23] A. Fabich and M. Benedikt, *Decay losses along the accelerator chain of the EURISOL Beta-beam baseline design*, AB-NOTE-2006-012 ATB.
- [24] M. Benedikt et al., *Conceptual design report for a Beta-Beam facility*, Eur. Phys. J. A (2011) 47:24, DOI 10.1140/epja/i2011-11024-5.
- [25] <http://www.euronu.org/>
- [26] R. Serber, *Nuclear reactions at high energies*, Phys. Rev., 72:1114,1947.
- [27] J.R. Glauber, *Cross sections in deuterium at high energies*, Phys. Rev., 100:242, 1955.
- [28] E. Gadioli, P.E. Hodgson, *Pre-equilibrium Nuclear Reactions*, Volume 168/1982. Springer Berlin/Heidelberg, 1982.
- [29] V. Weisskopf, *Statistics and nuclear reactions*, Phys. Rev., 52(4):295-303, August 1937.
- [30] E. Fermi, *High energy nuclear events*, Progr. Theor. Phys., 5:570, 1950.
- [31] V. Vandebosh, J.R. Huizenga, *Nuclear fission*, Academic Press, New York, 1984.
- [32] W.G. Lynch, *Nuclear fragmentation in proton- and heavy-ion-induced reactions*, Ann. Rev. Nucl. and Part. Sci., 37:493-535, December 1987.

- [33] G.D. Harp, J.M. Miller and B.J. Berne, *Attainment of statistical equilibrium in excited nuclei*, Phys. Rev. Lett., Vol. 165, Issue 4, (1968).
- [34] H. Sorge, H. StÄcker, and W. Greiner, *Nuclear reactions at relativistic energies*, Nucl. Phys. A 498 (1989) 567c.
- [35] J. Ranft, *Dual Parton Model at cosmic ray energies*, Phys. Rev. D, 51(1):64-84, January 1995.
- [36] A. Fassò, A. Ferrari, J. Ranft and P. Sala, *FLUKA: a multi-particle transport code*, CERN-2005-10 (2005).
- [37] A. Fassò, A. Ferrari, S. Roesler, P. Sala et al., *The physics models of FLUKA: status and recent developments*, Proceedings Computing in High Energy and Nuclear Phys. 2003, La Jolla, (March 24-28, 2003).
- [38] N. Nakao, N.V. Mokhov, *MARS15 Code in Accelerator Applications*, Fermilab-Conf-07-416-APC (2007).
- [39] H. Iwase, K. Niita and T. Nakamura, *Development of General-Purpose Particle and Heavy Ion Transport Monte Carlo Code*, J. Nucl. Sci. Technol, Vol. 39 (2002) 1142.
- [40] E. Cuccoli, A. Ferrari and G.C. Panini, *A group library from JEF 1.1 for flux calculations in the LHC machine detectors*, JEF-DOC-340 (91) (1991).
- [41] <http://www.oecd-nea.org/dbdata/data>.
- [42] H. Sorge, H. StÄcker, and W. Greiner, *Modelling multi-hadronic interactions in a phase space approach*, Ann. Phys. (N.Y.) 192 (1989) 266.
- [43] S. Roesler, R. Engel and J. Ranft, , Proceedings of the Monte Carlo 2000 conference, Lisbon, 23-26 October 2000.
- [44] https://www.fluka.org/free_download/course/heidelberg2011/Lectures/Ions0311.pdf.
- [45] J.J Griffin, *Statistical model of intermediate structure*, Phys. Rev. Lett., Vol. 17, Issue 9,(1966).
- [46] M. Cavinato et al., *The Boltzmann Master Equation theory, nuclear thermalization and pre-equilibrium reactions*, Proceedings 10th Int. Conf. on Nuclear Reaction Mechanisms, Varenna, 9-13 June 2003.
- [47] A. Mairani, *Nucleus-nucleus interaction modelling and applications in ion therapy treatment planning*, Scientifica Acta, ISBN 978-88-95767-09-3 , October 2007.
- [48] J.P. Mira, *The role played by quasi-elastic and inelastic break-up of the ^{12}C and ^{16}O projectiles in the production of Intermediate Mass Fragments at 14-35 MeV/u*, PhD Thesis to be submitted to the University of Stellenbosch, Stellenbosch SA.

Bibliography

- [49] T. Nakamura et al., *Measurements of secondary neutrons produced from thick targets bombarded by high energy neon ions*, J. Nucl. Sci. Technol., Vol. 36, No. 1, p. 41-53 (1999).
- [50] J. Ranft, *BRAHMS and PHOBOS collaborations*, Proceedings of the Hadronic Shower Simulation workshop, CP896, Batavia, Illinois (USA), September 2006.
- [51] T. Kurosawa et al., Phys. Rev. C 62, 044615, 2000.
- [52] G. Battistoni et al., *Heavy ion interactions from Coulomb barrier to few GeV/n: Boltzmann Master Equation theory and FLUKA code performances*, SLAC-PUB-10915.
- [53] I. Strašik et al., *Experimental study of the residual activity induced by 950 MeV/u uranium ions in stainless steel and copper*, NIM B 266, 3443 (2008).
- [54] *The 2007 Recommendations of the International Commission on Radiological Protection*, Annals of the ICRP, publication 103, Vol. 37, Issue 2, Elsevier,(2007).
- [55] G.R. Stevenson and R. H. Thomas, *Radiological Safety Aspects of the Operation of Proton Accelerators*, IAEA Technical Reports Series No. 283, Vienna 1988.
- [56] *Radiation quantities and units*, Report 33, Washington DC, ICRU publications, 1980.
- [57] *The ICRP cd-rom of dose coefficients*, A.W. Phipps, T.J. Silk and T.P. Fell, Radiation Protection Dosimetry, Vol. 79, Nos 1-4, pp. 363-365 (1998).
- [58] *Safety Code*, EDMS-335729 v.2, (2006).
- [59] P. Vojtyla, *Models for Assessment of the environmental impact of Radioactive releases from CERN facilities*, CERN-TIS-2002-013-TE8P (2002).
- [60] G.R. Stevenson, *Shielding high energy accelerators*, Radiation Protection Dosimetry, Vol. 96, NO. 4, pp. 359-371 (2001).
- [61] E. Mauro and M. Silari, *Radiation protection studies for a high-power 160 MeV proton linac*, CERN-SC2009-022-RP-TN v.2.
- [62] S. Roesler and G. R. Stevenson, *deq99.f-D A FLUKA user-routine converting fluence into effective dose and ambient dose equivalent*, CERN-SC-2006-070-RP-TN (2006).
- [63] *Conversion coefficients for use in radiological protection*, Annals of the ICRP, publication 74, Vol. 26, Issues 3-4, Elsevier,(1996).
- [64] M. Pelliccioni, *Overview of fluence-to-effective dose and fluence-to-ambient dose equivalent conversion coefficients for high energy radiation calculated using the FLUKA code*, Rad. Prot. Dos. 88 (2000) 279-297.
- [65] M. Pelliccioni, *Radiation weighting factors and high energy radiation*, Rad. Prot. Dos. 80 (1998) 371-378.

- [66] J.C. Wagner, A. Haghghat, *Automated variance reduction of Monte Carlo shielding calculations using the discrete ordinates adjoint function*, Nucl. Sci. and Eng.: 128, 186-208, 1998.
- [67] A. Fassò et al., *Predicting induced radioactivity at high energy accelerators*, SLAC-PUB-8215, August 1999.
- [68] K.S. Krane, *Introductory nuclear physics*, Wiley, 1998.
- [69] L. Ulrici, M. Brugger, T. Otto and S. Roesler, *Radionuclide characterization studies of radioactive waste produced at high-energy accelerators*, NIM A 562 (2006) 596-600.
- [70] M. Huhtinen, *Determination of cross sections for assessments of air activation at LHC*, CERN/TIS-RP/TM/96-29 (1997).
- [71] *Hauptabteilung für die Sicherheit der Kernanlagen (HSK), Berechnung der Strahlenexposition in der Umgebung aufgrund von Emissionen radioaktiver Stoffe aus Kernanlagen*, HSK-R-41/d, (July 1997).
- [72] *Swiss legislation on radiological protection (Ordonnance sur la Radioprotection, OraP)*, (1994).
- [73] K.F. Eckerman and J.C. Ryman, *External exposure to radionuclides in air, water and soil*, Federal guidance report No. 12, EPA 402-R-93-081, Environmental Protection Agency, Washington DC (1993).
- [74] A. Lachaize, *Le synchrotron rapidement pulse du complexe EURISOL/Beta Beam*, <https://espace.cern.ch/betanu/Articles/General>.
- [75] J. Payet, *Code BETA*, jpayet@cea.fr.
- [76] C. Theis et al., *Interactive three dimensional visualization and creation of geometries for Monte Carlo calculations*, NIM A 562 (2006) 827-829 .
- [77] P. Vojtyla, *Dose conversion coefficients for exposure of the reference population group to radionuclides in air released from the ISOLDE facility*, CERN-SC-2008-001-IE-TN.
- [78] A. Lachaize, *New beam structure at injection into the RCS*, presentation at 8th Beta-beam task meeting, CERN (2008).
- [79] M. Kirk, P. Spiller, C. Omet, J. Stadlmann, M. Benedikt, *Radiation hardness of PS magnets during beta-beam operation*, GSI Annual Report, 2006.
- [80] M. Benedikt, A. Fabich, M. Kirk, C. Omet, P. Spiller, *Estimation Of Decay Losses And Dynamic Vacuum For The Beta-beam Accelerator Chain*, CERN-AB-2006-040.
- [81] L. Bozyk, P. Puppel, P. Spiller and U. Ratzinger, *Strahlsim, a computer code for the simulation of charge exchange beam loss and dynamic vacuum in heavy ion synchrotrons*, Proceedings of the First International Particle Accelerator Conference, Kyoto, May 2010.

Bibliography

- [82] G. Dumont, M. Widorski, *Radiation survey results 2010 PS Complex*, presentation at “Machine Studies Working Group”, EDMS 1132092.
- [83] G. Dumont, *Radiation survey results 2011-2012 PS Complex*, presentation at “Machine Studies Working Group”, EDMS 1179664.
- [84] <http://psring.web.cern.ch/psring/psring/pic.php?sector=1>.
- [85] F.W. Jones, *Development of the Accsim Tracking and Simulation Code*, Proceedings 1997 Particle Accelerator Conference, Vancouver, May 1997.
- [86] K. Artoos et al., *Design, manufacturing status, first results of the LHC main dipole final prototypes and steps towards series manufacture*, IEEE Trans. Appl. Supercond. 10 , 1 (2000) 98-102.
- [87] G.A. Vossa, T. Rabedeau, S. Raither, H. Schopper, E. Weihreter and H. Winick, *SESAME: an extended spectral range synchrotron radiation facility in the Middle East based on an upgrade to BESSY I*, NIM A, 467-468 (2001) 55-58.
- [88] H. Vincke and P. Vojtyla, *Radiological and environmental impacts of air releases from the SPS running with increased intensity*, CERN-SC-2005-019-IE-TN.
- [89] E. Wildner, *Beta Beams*, presentation at European Strategy for Neutrino Oscillation Physics II, May 2012, CERN.

Curriculum Vitae

Name: Stefania Trovati

Date of birth: 9th May 1977

Nationality: Italian

E-mail: stefania.trovati@psi.ch

Employment

Since December 2010. Applied physicist at EBG MedAustron GmbH, responsible of the design and realization of the radiation heads for the MedAustron hadron-therapy facility in Wiener Neustadt (Austria): procurement of detectors for beam characteristics read-out and control, commissioning test plan, risk management for the medical front end. Collaboration with the PSI proton-therapy group: commissioning of Gantry 2, development of Matlab tools for commissioning data analysis.

From March 2010 to October 2010. Assistant at Ecole Polytechnique Federale de Lausanne (EPFL) and Unpaid Associate at CERN. Radiological characterization of the Proton Synchrotron (PS) nuclear waste.

From March 2007 to February 2010. Marie Curie Fellow: Marie Curie Early Stage Training at CERN within the RADENV (Radiation protection and environmental impact of future accelerators) project (MC-EST # 20174), <http://cordis.europa.eu/>.

Education

December 2008-May 2013. PhD at EPFL, Lausanne. Thesis title: "Assessment of the radiological risks for a beta-beam facility at CERN". Supervisor: Prof. L. Rivkin.

Curriculum Vitae

June 2009. Degree as “Personne competente en radioprotection” at ‘Institut universitaire de radiophysique appliquée (IRA)’ in Lausanne, Switzerland.

March 2004. Master’s degree in Physics (“Laurea”) at the Department of Physics, University of Pavia. Supervisor: Dr. P. Galinetto.

Participation in conferences, workshops and meetings

- “Activation studies for a beta-beam Decay Ring (DR): residual dose rates during maintenance and airborne activity”, Shielding Aspects of Accelerators, Targets and Irradiation Facilities - SATIF 10, CERN, Geneva, Switzerland, June 2-4, 2010.
- “Radiation Protection issues for a beta-beam facility at CERN”, Scientific Policy Committee Panel (Neutrinos), CERN, Geneva, Switzerland, June 2009.
- “Radiation Protection for beta-beams in FP7”, FP7 Kick-Off Meeting, CERN, Geneva, Switzerland, March 2009.
- “General status of RP studies and investigations on the Decay Ring”. Beta-beam task meeting, CERN, Geneva, March 2009.
- “Activation studies for a beta-beam Rapid Cycling Synchrotron (RCS)”. First International Workshop on Accelerator Radiation Induced Activation (A.R.I.A.), PSI, Villigen, Switzerland, October 2008.
- “Decay Ring (DR) Radiation Protection Studies”. Beta-beam task meeting, CERN, Geneva, October 2008.
- “Radiation Protection Issues for the RCS (2)”. Beta-beam task meeting, CEA Saclay, May 2008.
- “Radiation Protection Issues for the RCS (1)”. Beta-beam task meeting, IPN Orsay, November 2007.
- “Radiation shielding of a beta-beam Rapid Cycling Synchrotron (RCS)”. 11th International Conference on Radiation Shielding, Atlanta, April 2008.
- “Beam extraction line for the experimental area at CNAO: status of the project.” CNAO collaboration meeting (2006).
- “Human exposure to space radiation: role of primary and secondary particles”. MICROS2005 Conference, Venice, November 2005, poster session.
- “GCR and SPE organ doses in deep space with different shielding: Monte Carlo simulations based on the FLUKA code coupled to anthropomorphic phantoms”. 2005 FLUKA collaboration meeting.

Courses and schools

- “Introduction to particle accelerators”, EPFL, Lausanne, February 2010.
- “Cours de Radioprotection destine aux experts dans le domaine des secteurs de travail de type B et C”, IRA Lausanne, Switzerland, June 2009.
- “International school on Radiation Damage and Protection”, Erice, Italy, May 2009.
- “CERN Accelerator School (CAS): introductory level”, Frascati, Italy, November 2008.
- “Principles of Protection Against External Radiation Sources”, Health Protection Agency (HPA), Chilton, England, October 2008.
- “Course on Radiation Protection Measurements”, Politecnico, Milano, Italy, 17-21 September 2007.
- “Python - Hands-on Introduction”, CERN technical training, June 2007.
- “Nuclear, Subnuclear and Applied Physics Software National Seminar”, Alghero (SS), Italy, June 2006.
- “National Seminar on Nuclear and Sub-Nuclear Physics”, Otranto, Italy, September 2005.

Publications

- M. Benedikt, A. Bechtold, F. Borgnolutti, E. Bouquerel, L. Bozyk, J. Bruer, A. Chancé, P. Delahaye, A. Fabich, S. Hancock, C. Hansen, E. Jensen, A. Källberg, M. Kirk, A. Lachaize, M. Lindroos, M. Loiselet, M. Magistris, S. Mitrofanov, A. C. Mueller, J. Payet, H. Podlech, P. Puppel, M. Silari, A. Simonsson, P. Spiller, J. Stadlmann, T. Stora, A. Tkatchenko, S. Trovati, V. Vlachoudis, E. Wildner. “Conceptual design report for a Beta-Beam facility”, *Eur. Phys. J. A* (2011) 47:24, DOI 10.1140/epja/i2011-11024-5.
- S. Trovati and M. Magistris. “Activation studies for a beta-beam Decay Ring (DR): residual dose rates during maintenance and airborne activity”, *Shielding Aspects of Accelerators, Targets and Irradiation Facilities - SATIF 10 - Workshop Proceedings*, OECD Publishing, January 2011.
- S. Trovati, M. Magistris, M. Silari. “Radiation shielding of a beta-beam Rapid Cycling Synchrotron”, *Nuclear Technology*, Vol. 168, November 2009.
- S. Trovati, M. Magistris, M. Silari. “Activation studies for a beta-beam Rapid Cycling Synchrotron (RCS)”, *PSI proceedings 09-01*, ISSN 1019-0643, January 2009.
- S. Trovati, M. Kirk, P. Delahaye, M. Magistris. “Radiation protection studies on a possible future beta-beam operation of the CERN PS”, *CERN-SC-2009-051-RP-TN*, 2009.

Curriculum Vitae

- S. Trovati, M. Magistris, M. Silari. “Radiation Protection Issues for the Beta-Beam Rapid Cycling Synchrotron”, CERN-SC-2008-070-RP-TN v.1, 2008.
- F. Ballarini, M.V. Garzelli, G. Givone, A. Mairani, A. Ottolenghi, D. Scannicchio, S. Trovati, A. Zanini. “Modelling the radiation action for the estimation of biological effects in humans”, International Conference on Nuclear Data for Science and Technology 2007, DOI:10.1051/ndata:07649.
- S. Trovati, F. Ballarini, G. Battistoni, F. Cerutti, A. Fassò, A. Ferrari, E. Gadioli, M.V. Garzelli, A. Mairani, A. Ottolenghi, H.G. Paretzke, V. Parini, M. Pelliccioni, L. Pinsky, P.R. Sala, D. Scannicchio, and M. Zankl. “Human exposure to space radiation: role of primary and secondary particles”, Radiation Protection Dosimetry, 10.1093/rpd/ncl438, December 2006.
- F. Ballarini, G. Battistoni, M. Campanella, M. Carboni, F. Cerutti, A. Empl, A. Fassò, A. Ferrari, E. Gadioli, M.V. Garzelli, M. Lantz, M. Liotta, A. Mairani, A. Mostacci, S. Muraro, A. Ottolenghi, M. Pelliccioni, L.S. Pinsky, J. Ranft, S. Roesler, P.R. Sala, D. Scannicchio, S. Trovati, R. Villari, T. Wilson, N. Zapp, V. Vlachoudis. “The FLUKA code: an overview”, J. of Phys. Conf. Series 41, 151.
- S. Trovati, F. Ballarini, G. Battistoni, F. Cerutti, A. Fassò, A. Ferrari, E. Gadioli, M.V. Garzelli, A. Mairani, A. Ottolenghi, H.G. Paretzke, V. Parini, M. Pelliccioni, L. Pinsky, P.R. Sala, D. Scannicchio, and M. Zankl. “Human exposure to space radiation: role of primary and secondary particles”, The 14th Symposium of Microdosimetry, Venice, November 2005, Book of abstracts.
- Co-author in a number of publications within the FLUKA collaboration.